UNIVERSITY OF Cincinnati

Document of Defense

Date: 11/8/2024

I, Mohamad Ghulam, hereby submit this original work as a part of the requirements for the degree of Doctor of Philosophy in Aerospace Engineering.

It is entitled:

Characterization of Valved-Pulsejet and Single-Element Lean Direct Injection Combustion Systems.

Student Signature: Mohamad Ghulam

This work and its defense approved by:

Chair : Ephraim Gutmark, Ph.D.

Member : Shaaban Abdallah, Ph.D.

Member : Prashant Khare, Ph.D.

Characterization of Valved-Pulsejet and Single-Element Lean Direct Injection Combustion Systems

A dissertation submitted to the

Graduate College

of the University of Cincinnati

in partial fulfillment of the

requirements for the degree of

Doctor of Philosophy

in the Gas Dynamics and Propulsion Laboratory

of the Department of Aerospace Engineering and Engineering Mechanics

by

Mohamad bin Mustfa Ghulam

M.S. in Aerospace Engineering, University of Cincinnati

August 2019

Committee Chair and Thesis Advisor: Dr. Ephraim J. Gutmark, Ph.D.

Committee Member: Dr. Shaaban Abdallah, Ph.D.

Committee Member: Dr. Prashant Khare, Ph.D.

Abstract

The pulsejet study investigates twelve configurations of the self-aspirated valved pulsejet, focusing on its operational mechanism. It begins by characterizing the engine's acoustic field with varied boundary conditions, revealing an extended effective acoustic length beyond the combustion chamber and tailpipe sections when the valve is open. Radial and lateral velocity fluctuations are hypothesized as causes for vortex structure generation. Analysis of reacting pulsejets using gasoline and ethanol fuels shows that the operating frequencies are unaffected by fuel type, with geometric arrangement as the primary frequency factor. Fluctuations in dynamic pressure, microphone readings, and thrust characterize engine stability, impacted by low-frequency modes and higher harmonics. Tailpipe length emerges as the key geometric factor for performance enhancement with the medium size being the optimal option. Pressure field analysis demonstrates shock wave generation during ignition, serving as an excitation mechanism. Notably, different configurations with varied operating frequencies can yield equivalent thrust, indicating that thrust production is not solely dependent on pressure rise during combustion, despite similar pressure rise observed across most cases.

The second study investigates the impact of the equivalence ratio, inlet air temperature, confinement ratio, and exit boundary on the flame dynamics of a single-element, low-emission nozzle used in a multipoint lean direct injection (MLDI) combustion system. High-speed OH* chemiluminescence, combined with sound pressure measurements, is used to analyze the flame structure and its correlation to sound intensity. Three distinct flame types are identified: the V-flame, M-flame, and lifted-distributed flame. The V-flame, occurring at higher equivalence ratios, is associated with axial fluctuation modes and is coupled (in-phase) with the acoustic field, leading to higher sound intensity. Notably, the matching of frequency values between the flame's coherent mode (830 Hz) and sound pressure (822.6 Hz) during the V-flame condition indicates flame-

acoustic interaction. The M-flame, observed at lower equivalence ratios, is associated with radial fluctuation modes and is decoupled (out-of-phase) from the acoustic field, resulting in lower sound intensity. The sound intensity is linearly correlated with the equivalence ratio. As the equivalence ratio approaches lean blowout (LBO), the flame loses its coherent structure and transitions into a random turbulence mode, suggesting that the noise measured outside the combustion chamber is dominated by turbulence rather than flame-acoustic coupling mechanisms. Increasing the inlet temperature and adding the exit plate both shift the flame anchoring point upstream. This occurs because a higher inlet temperature decreases air density, which increases axial velocity and reduces the size of the inner recirculation zones, leading to a V-flame anchored near the nozzle exit. Similarly, adding the exit plate raises the pressure gradient in the reverse flow region, pushing the flame anchoring point upstream. Each parameter promotes a different flame dynamic mode. The axial fluctuation mode, associated with flame vortex roll-up, is magnified with increasing inlet temperature, particularly in more confined flames, such as those with a 5.6 confinement ratio. In contrast, the newly revealed axial-radial fluctuation mode (where both vortex roll-up and flame angle fluctuations occur simultaneously) is amplified after adding the exit plate. As the confinement ratio increases, the size of the inner recirculation zone grows linearly, producing larger flames with lower OH* intensity, as the OH* species become more distributed. Larger confinement ratios, such as 6.9 and 9.6, promote the radial fluctuation mode associated with flame angle fluctuations, due to the increased inner recirculation vortices push the jet radially. Significant changes in sound pressure level (SPL), around 15 decibels (dB), are observed in microphone measurements as the flame structure and associated dynamic modes transition between the identified flame types. Finally, the LBO limit, important for reducing thermal NOx formation, is influenced by these parameters.

Acknowledgments

In the name of Allah (God), the Most Gracious, the Most Merciful, and his peace and blessings be upon the prophet Mohammad, his family, and his companions. First and foremost, I would like to express my deepest gratitude to Allah. Alhamdulillah, at the beginning and at the end, for His countless blessings and for guiding me to achieve this milestone in my academic journey. Without His grace, none of this would have been possible.

I am forever indebted to my beloved parents, whose unwavering support has been my strength throughout my life, especially during the challenging years of studying abroad. My mother deserves this Ph.D. even more than I do; her boundless dedication, sacrifices, and tireless efforts in raising me and my siblings have been my greatest inspiration. To my father, thank you for your endless encouragement and for all the years of hard work and sacrifices you made to provide for our family.

To my six wonderful sisters and their families—thank you for your constant support and encouragement, and for always being there for me, no matter how far apart we are. You have all been my cheering squad, and I am so grateful for each of you. To my extended family, my aunts, uncles, all my relatives, and friends thank you for your kind words and prayers that have uplifted me along this journey.

I would like to extend my sincere appreciation to the leadership and government of the Kingdom of Saudi Arabia, as represented by the Ministry of Education and the Saudi Arabian Cultural Mission (SACM) in the United States of America, for their generous support of the Ph.D. program.

A special and heartfelt thank you goes to my thesis advisor, Dr. Ephraim Gutmark, or "Effie" as he is fondly known. Since our first meeting in 2016, during my first semester as a master's student, Dr. Gutmark has welcomed me into the exciting world of research in the Gas Dynamics

and Propulsion Laboratory. I am deeply grateful for his guidance, support, and the wealth of knowledge he shared with me throughout my time at the University of Cincinnati. His mentorship has left an indelible impact on my life and career.

Finally, to all the students and team members of our lab, thank you for the collaboration, and support. Each of you contributed to making this journey memorable and rewarding. Thank you to everyone who helped make this achievement possible.

Table of Contents

Nomenclature

f = frequency (Hz)

p_{ref} = reference pressure (Pa)

SPL = sound pressure level (dB)

SC = short combustor (cm)

LC = long combustor (cm)

ST = short tailpipe (cm)

MT = medium tailpipe (cm)

LT = long tailpipe (cm)

FF = flare-off

FN = flare-on

FFT = fast Fourier transform

$SPOD$ = spectral proper orthogonal decomposition

CR = confinement ratio

LBO = lean blowout

I = OH* intensity

Re = Reynolds number

c = speed of sound (m/s)

θ = phase angle (degree)

ρ = density (kg/m^3)

μ = dynamic viscosity ($kg/m\,.s$)

ϕ = global equivalence ratio

Chapter 1

Operational Mechanism of Valved-Pulsejet Engines

1. Introduction

The pulsejet engine is considered to be a pressure gain combustion (PGC) technology, attracting researchers and industries in recent years due to its simple and low-cost design compared to conventional gas turbine engines. Pulsejet technology holds potential for various applications, including serving as a lift engine for vertical takeoff and landing (VTOL) aircraft [1] and small conventional fixed-wing aircraft [2]. In a conventional gas turbine engine, total pressure loss primarily stems from combustion inefficiencies and fluid dynamic losses. The combustion chamber experiences the largest total pressure, resulting in a 4-8% decrease compared to that delivered by the compressor [3,4]. This loss in total pressure leads to increased entropy and reduced thermodynamic efficiency of the working fluid, limiting the usable work extracted from the rise of stagnation pressure produced during combustion events. Several studies have demonstrated a significant improvement in thermodynamic efficiency by integrating pressure-gain combustion systems into gas turbine engines [5–9]. Pressure-gain combustion systems were proposed as early as the 1940s, with subsequent studies showing net total pressure gains ranging from 1-4% of the total pressure delivered by the compressor [10–16]. Later research, conducted by Paxson et al., was tailored to the relevant environment of modern gas turbine engines [17,18]. The generic thermodynamic cycle of the pulsejet engine, known as the Humphrey cycle, replaces the constant-pressure heat addition process (isobaric) with a constant-volume heat addition process (isochoric). The pulsejet engine operates as an acoustically driven device, relying on the coupling between pressure waves generated from combustion events and the antinode pressure of the

resonance-natural mode (thermoacoustic coupling) to create self-aspirated intermittent combustion operation [19]. In a typical passively valved pulsejet, fuel is introduced into the combustion chamber by imposing air into the carburetor section, creating a low-pressure zone that opens the valve and allows fuel admission. Initially, inlet air is supplied to start the engine. Once ignited by a spark plug, a high-pressure zone forms inside the chamber, causing the valve to close. Subsequently, combustion products travel through the tailpipe and exit the engine, generating thrust and forward motion. Afterwards, a low-pressure zone reoccurs in the chamber, acting as a vacuum. This allows fresh reactants to enter the combustion chamber through the valve from the carburetor, inducing a reverse flow upstream from the back end of the engine's exhaust due to ambient air entrainment. This repetitive process occurs at the resonance frequency, which depends on the engine's size. [20].

The Argus engine, which powered the German V-1, stands as a renowned example of a valved pulsejet engine. In recent years, researchers have introduced a novel concept utilizing an active-controlled rotary mechanical valve while constantly imposing inlet air [21]. This robust design ensured sustained pulsejet operation over hours, with the measured pressure gain ranging from 20-35% of that of the passive valve pulsejet [22]. Furthermore, studies demonstrated that the imposed airflow significantly impacts the phase lag between acoustic pressure and unsteady heat release. Zhu et al. revealed a low-frequency oscillation dominating operation over the resonance frequency mode, attributed to blowout conditions resulting from decreased fuel flow rates[23]. Conversely, Geng et al., through particle image velocimetry (PIV) and simulation studies, associated the vortex structure generated after adding the flare nozzle with low-frequency oscillation, enhancing thrust [24,25]. Paxson et al. explored the effect of ejector shape on pulsejet performance, concluding that a tapered ejector optimized thrust augmentation [26]. Additionally, valveless or aero-valve

pulsejets represent an alternative design achieved by replacing the reed valve with a short-bent pipe. Studies by Maqbool et al. investigated the acoustic behavior of single valveless pulsejet engines and interconnected pulsejets with various duct geometries, aiming to establish systems providing distributed thrust [27,28]. Another study by Gieras et al. examined the effect of fuel injection design and location on valveless pulsejet engine behavior, demonstrating the possibility of modifying pressure and thrust amplitudes and operating frequency based on fuel injection locations [29]. Notably, efficient operation was achieved when the combustion zone was near the end of the combustion chamber, contrasting with results from active valved pulsejets [23].

Several experimental research studies were conducted at the Gas Dynamic and Propulsion Laboratory at the University of Cincinnati. Vijay et al. conducted ionization measurements and found that combustion events in the pulsejet did not occur in a wavy pattern like the pressure profile. Instead, combustion events happened at arbitrary axial locations[30]. Furthermore, the combustion events were in phase with pressure peaks but with some time lag, and stable operations tended to have a higher time lag between the pressure peak and the first combustion event. Justas et al. analyzed the effects of geometry on pressure, temperature, and thrust [31]. They demonstrated that the long combustor configuration had more stable operation than the short combustor configuration. In most cases with long combustors, combustion events occurred within the combustion chamber, while in some short combustor cases, combustion events were found at the beginning of the tailpipe section. Additionally, in all configurations, the maximum temperature was located near the convergent section. Moreover, a pressure blip was noticed at the exit of the tailpipe in self-aspirated cases (without imposing inlet air), which was associated with long combustor configurations and some short combustor cases. Cases with imposing inlet air (assisted cases), particularly those with short tailpipes, had smaller pressure magnitudes than self-aspirated

cases (unassisted cases). These results may be attributed to the decoupling between acoustic pressure oscillation and unsteady heat release caused by the imposition of inlet air, as recently explained by Zhu et al. [23]. Higher thrust was observed after adding the flare; however, not all configurations experienced an increase in thrust value with the flare nozzle. An interesting study investigated the flow dynamics inside a transparent quartz pulsejet using high-speed broadband chemiluminescence and outside the engine at the tailpipe's exhaust using shadowgraph [32,33]. The results revealed two groups of vortices: the first, located at the combustion chamber, traveled upstream and impinged on the upstream wall, while the second group of vortices created at the lip of the tailpipe's exhaust were ejected downstream. In cases with the flare nozzle attached to the tailpipe, additional vortices were generated at the trailing edge of the flare nozzle and penetrated radially. Finally, sound measurements were conducted on an actual Argus 014 engine, and the highest sound pressure was recorded at an angle of 90 degrees to the engine axis. Interestingly, a loud, distinct boom sound that produced an SPL of 166 dB (4.953 m away from the engine) was captured during the ignition of the Argus engine. Finally, sound measurements were conducted on an actual Argus 014 engine, with the highest sound pressure recorded at an angle of 90 degrees to the engine axis. Interestingly, a loud, distinct boom sound that produced an SPL of 166 dB (4.953 m away from the engine) was captured during the ignition of the Argus engine. Furthermore, a strong asymmetry was noticed between peak over-pressure and under-pressure, with the former occurring faster than the latter, suggesting possible shock-related physics involved during the ignition of the Argus engine [34].

Despite numerous studies on pulsejet engines, there remains a lack of clear and comprehensive understanding of how thrust production, pressure gain due to combustion, and sound measurements correlate with systemic variations in the engine's geometric configurations.

Additionally, no study has conducted phase-average results and has relied on instantaneous and computational methods instead. Moreover, there has been no coherent explanation of how vortex structures are generated inside the engine and outside the engine after the addition of the flare nozzle. Hence, the aim of this study is to gain a comprehensive understanding of the passively valved self-aspirated pulse jet, focusing on acoustic modes, pressure behavior within the engine, fuel effects, and thrust production. A total of twelve different configurations are examined to observe variations in engine behavior, considering parameters such as combustor length, tailpipe length, and the addition of a flare nozzle. The novelty of this study lies in several new findings regarding the Curtis-Dyna pulsejet design. Firstly, the exploration of acoustic fields in terms of velocity fluctuation, based on acoustic simulation results, reveals new phenomena occurring at the convergent and flare nozzle sections, hypothesized to be the reason behind vortex structure generation both inside and outside the engine. Secondly, engine stability is characterized by comparing the dominant frequency modes among pressure fields inside the engine, external microphone measurements, and thrust produced. During stable operations, dominant frequency values are consistent across all three types of measurements, while they vary during unstable operations. Increasing the tailpipe length enhances the consistency of frequency values among these measurements, with the medium tailpipe proving to be the most efficient option. However, even during stable operation, the mode of measured pressure at the beginning of the tailpipe, post-convergent section, differs from those observed from other pressure sensors. Additionally, an interesting finding is the sudden pressure increase observed after the first sensor at the combustion chamber entrance, with maximum pressure occurring at the third sensor in the convergent section, indicating shock wave generation from fuel ignition. Furthermore, three different types of pulsejet operations are identified: resonance stable, resonance unstable, and non-resonance unstable

operations. Results indicate that interference from higher harmonic modes and low-frequency modes are the root causes of unstable pulsejet operations. Thirdly, new phase-averaged results provide important insights into the relationship between pressure waves inside and thrust production. Interestingly, thrust results across the twelve geometries show that different engine configurations with varying operating frequency values can produce the same amount of thrust, despite featuring similar pressure rise inside the engine, indicating that thrust is not solely dependent on the pressure rise due to combustion events.

2. Experimental Setup

The pulsejet utilized in the study (see Fig.1 and Fig.2) consists of a nozzle installed inside the carburetor section where the air/fuel mixture is injected. The headwall section contains circumferentially distributed holes covered by a reed-valve type. The passive reed valve controls the entry of air/fuel mixture into the combustion chamber. The combustion chamber is instrumented with a spark plug to ignite the entering air/fuel mixture. To initiate the engine, compressed inlet air is utilized only at the beginning of the operation to force the fuel to flow into the chamber by creating a low-pressure zone, causing the reed valve to open and admit the air/fuel mixture. After the mixture of reactants enters the combustion section, the spark ignites the air/fuel mixture for a few cycles until unassisted operation is achieved, at which point the spark and compressed air supply are switched off. However, one of the cases with gasoline fuel required constant imposition of compressed air, which is the SC-ST-FF configuration.

The design is adapted from the commercial *HobbyKing* Curtis-Dyna pulsejet, which is a compression-fit engine utilizing alignment plates to connect different standard pipes together. The pulsejet engine is secured by three threaded rods that compress the structure using collars around the alignment plates. The length of the combustor sections varies between 5.08 cm and 7.62 cm with a 4.5 cm convergent section, while tailpipe lengths are 27.94 cm, 43.18 cm, and 58.42 cm (see Table 1). Additionally, a 2.5 cm flare section is added or removed at the end of the tailpipe. The study comprises twelve different configurations of the pulsejet engine (see Table 2). For clarity, each configuration is abbreviated: short and long combustors are denoted as SC and LC, respectively, while short, medium, and long tailpipes are abbreviated as ST, MT, and LT. Flaring is abbreviated as FF and FN for flare-off and flare-on, respectively. In the frequency-response campaign (non-reacting cases), a loudspeaker is placed approximately 2 cm from the pulsejet exit

to excite the system, as depicted in Fig. 1. Three flush-mounted microphones measure pressure oscillations inside the pulsejet at the beginning of the combustor, convergent section, and the start of the tailpipe. In the reacting cases (without the loudspeaker), the pulsejet is instrumented with five PCB Piezotronics high-speed pressure sensors, flush-mounted with a 5% error margin, capable of detecting dynamic pressure oscillations [35]; however, they are not suitable for static pressure measurements (two at the combustor, one at the convergent section, one at the beginning of the tailpipe, and one at the end of the tailpipe). The sensor locations are provided in Table 3. Pressure measurements with microphones were collected at a sampling rate of 20 kHz and 100 kHz when using PCB sensors for reacting cases, exceeding the Nyquist criterion for pulsejets operating at sub-400 Hz. Thrust is measured using the dynamic ICP Piezotronics (208C03 type with ± 15% sensitivity) internally preloaded force sensor, functioning as a spring/mass system [36,37]. The force sensor is installed between two plates, impended beneath and connected to the movable plate holding the pulsejet (see Fig. 2). A free-field Bruel and Kjaer half-inch microphone (type 1706, with 48.4 mV/Pa sensitivity, and inherent noise of 16.5 dB) is used for sound measurement, positioned approximately 60 degrees from the engine axis starting from the engine's head side.

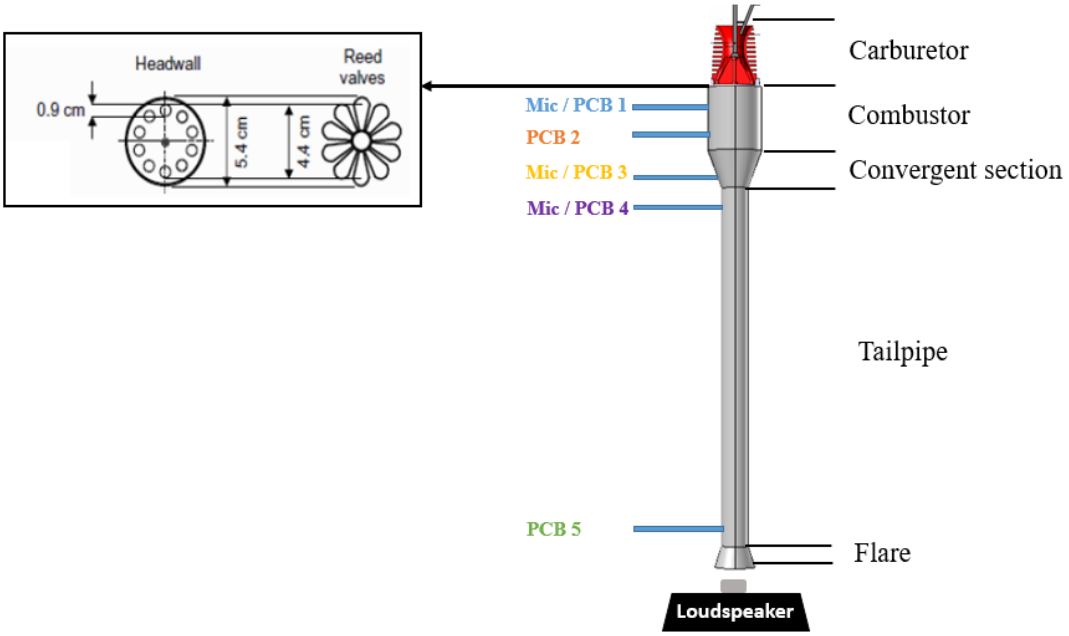

Fig. 1 Diagram of the experimental setup for the frequency-response study on the Curtis-Dyna pulsejet.

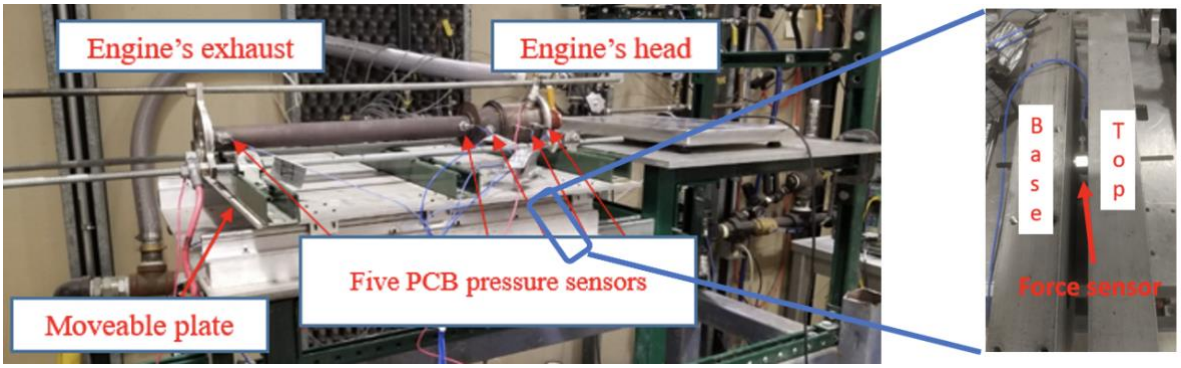

Fig. 2 Experimental setup of the reacting pulsejet that includes five PCB pressure sensors, and force sensor for thrust measurement embedded underneath the moveable plate.

Table 1. Geometrical dimensions of each section of the pulsejet.

	Length (cm)	Maximum Diameter (cm)	Volume (cm^3)
Short Combustor (SC)	5.08	6.35	160.9
Long Combustor (LC)	7.62	6.35	241.3
Convergent Section	4.5	6.35	83.5
Short Tailpipe (ST)	27.94	3.2	224.7
Medium Tailpipe (MT)	43.18	3.2	347.3
Long Tailpipe (LT)	58.42	3.2	469.8
Flare	2.5	4.75	31.4
Carburetor	5.59	3.56	44.53

Table 2. The twelve different configurations included in this study.

Case number	Configuration	Total length (cm)
1	SC-ST-FF	33.02
2	SC-ST-FN	35.52
3	LC-ST-FF	35.56
4	LC-ST-FN	38.06
5	SC-MT-FF	48.26
6	SC-MT-FN	50.76
7	LC-MT-FF	50.8
8	LC-MT-FN	53.3
9	SC-LT-FF	63.5
10	SC-LT-FN	66
11	LC-LT-FF	66.04
12	LC-LT-FN	68.54

Table 3. Microphone and PCB pressure sensors' locations from the start of a given part.

	Port 1 (cm)	Port 2 (cm)	Port 3 (cm)	Port 4 (cm)	Port 5 (cm)
Short Combustor (SC)	1.7	3.4	-	-	-
Long Combustor (LC)	2.54	5.08	-	-	-
Convergent Section	-	-	2.25	-	-
Short Tailpipe (ST)	-	-	-	2	25.94
Medium Tailpipe (MT)	-	-	-	2	41.18
Long Tailpipe (LT)	-	-	-	2	56.42

The frequency-response study proceeds as follows: (i) Uniform white noise signals are emitted from the loudspeaker, controlled by the DAQ acquisition system, within a specified frequency range (in this study, the range is set to 50 – 3000 Hz). (ii) Subsequently, a Fast Fourier Transform (FFT) is applied to the acquired pressure data to identify pressure peaks corresponding to the fundamental mode and higher harmonics of a particular pulsejet configuration. (iii) Each mode is then individually excited by emitting sinusoidal sound waves through the loudspeaker at the frequencies obtained from the FFT results.

It is worth mentioning that the study is limited to atmospheric pressure conditions and does not account for pulsejet operation at high-pressure conditions. Another limitation of the study is the absence of measurements for the flow rate of air and fuel injected into the engine; consequently, the equivalence ratio cannot be determined. Moreover, this study does not include optical diagnostic measurements of the pulsejet cycle, and it is restricted to pressure dynamics inside the engine, as well as sound and thrust measurements.

3. Mathematical Model for Acoustics Simulation

The study employs a linear treatment of acoustic waves to comprehend the inherent acoustic behavior of the pulsejet in the absence of mean flow. Acoustic simulations of the non-reacting pulsejet are conducted using the COMSOL software, a commercially available finite element method (FEM) software. The model addresses the propagation of sound waves, or pressure waves, in the frequency domain by solving the Helmholtz equation, following previous work by Ghulam et al. [38]:

$$\nabla . \left(-\frac{1}{\rho}(\nabla p_t - q_d) - \frac{k^2 p_t}{\rho}\right) = Q_m \qquad (1)$$

Here, ρ represents air density, q_d denotes the dipole domain source, Q_m indicates the monopole domain source, $k = \left(\frac{\omega}{C}\right)$ is the wave number (with the angular frequency: $\omega = 2\pi f$ and the wavelength: $\lambda = -i\omega$), and p_t denotes the total pressure, where:

$$p_t = p + p_b \qquad (2)$$

In this equation, p represents the solved pressure, and p_b is the background pressure. The ideal gas law assumption is applied for acoustic simulation, which offers a reasonably accurate approximation in pulse combustors [39]. With a specific gas constant R = 287J/kg·K and an assumed temperature inside the pulsejet engine T = 293 K for non-reacting cases, the speed of sound is C = 343.14 m/s. The finer free tetrahedral mesh option is selected to ensure adequate resolution of all wavelengths (or frequencies) of interest. Three different boundary conditions are examined: close-open, open-open (with the carburetor fully removed), and reed valve open-open. A sound hard boundary (wall) is applied for the closed boundary, where the normal component of the acceleration is zero:

$$-n.\left(-\frac{1}{\rho}(\nabla p_t - q_d)\right) = 0 \qquad (3)$$

For a zero-dipole domain source ($q_d = 0$) and constant fluid density ρ, this condition implies that the normal derivative of the pressure is zero at the boundary ($\frac{\partial p_t}{\partial n} = 0$). Conversely, for the open boundary, a sound soft boundary is applied, where the acoustic pressure vanishes ($p_t = 0$). When the carburetor is included in the reed valve open-open case, the opening areas of the ten small holes at the headwall are combined and treated as a single hole with a total opening area $A_{combined\ holes} = 6.36\ cm^2$. Figure 3 depicts the two different computational domains of the LC-MT-FN case for brevity.

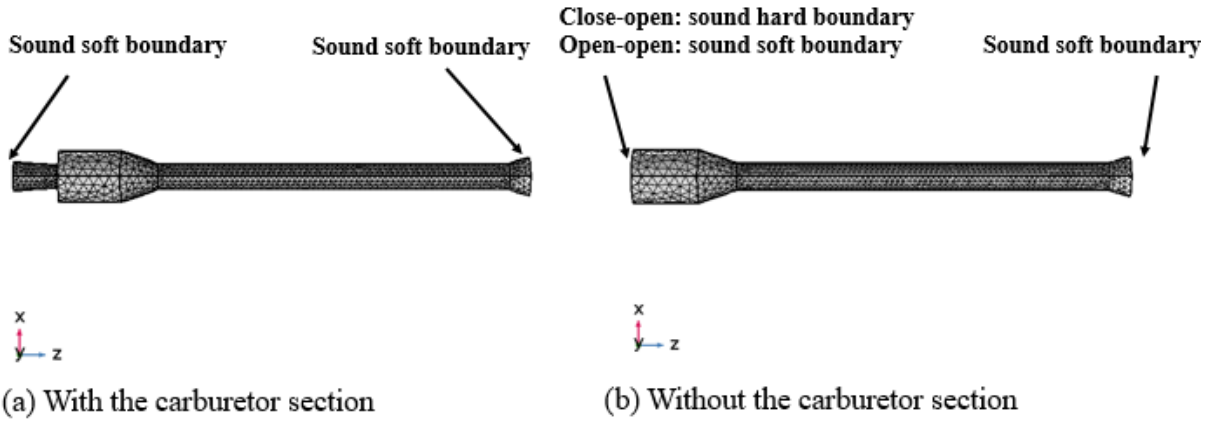

Fig. 3 The computational setup of the (a) reed valve open-open and (b) for both close-open and open-open cases of the LC-MT-FN configuration.

4. Results and Discussion

4.1. Acoustic Characteristics

4.1.1. Acoustic pressure fluctuations

The impact of different boundary conditions on the fundamental mode is a crucial aspect of the current study, as the pulsejet relies on the fundamental mode for operation following excitation. The results of both the acoustics simulation and experimental frequency study of the LC-MT-FF/FN cases are presented together in Fig. 4, with the pressure field normalized by the maximum pressure values. In the experimental data, the pressure values at the exit were assumed to be zero for an open boundary, as no microphone was placed at the engine's exit. The simulation and experimental results of the fundamental mode generally exhibit good agreement across all the different boundary conditions, particularly for the close-open boundary condition, owing to its simple geometry and fewer acoustic losses compared to the other two boundary conditions. Additionally, surface colored-contour plots of the total acoustic pressure fields for the LC-MT-FF/FN configurations are generated to visualize the mode shape with different inlet boundary conditions (see Fig. 5). It's evident that when the reed valve is fully closed (close-open case), the fundamental mode is a quarter-wave mode, with the pressure antinode situated within the combustion chamber and convergent section. Conversely, when the reed valve is open (reed valve open-open) or completely removed (open-open), the fundamental mode transforms into a half-wave mode with different antinode pressure locations. In the reed valve open-open case, the high-pressure region begins from the combustion section and peaks at the start of the tailpipe section, with the antinode pressure moving downstream to the middle of the tailpipe section in the open-open case. These findings suggest that the effective acoustic length of the pulsejet engine, which simulates when the valve is open during normal operation, extends to the upstream section

(carburetor) of the engine and is not solely determined by the combustion chamber and tailpipe sections. This discovery is significant because pulsejet researchers have traditionally focused only on the combustion chamber and tailpipe sections when calculating the operating frequency. Furthermore, these results underscore the impact of boundary conditions on altering the location of the antinode pressure, which is crucial for the excitation of the pulsejet system. As a device driven by acoustics, understanding the pressure antinode locations is essential for designing a pulsejet so that the ignition source can be correctly determined by placing it within the antinode pressure regions of the engine, thereby serving as an excitation mechanism for the system. Additionally, it's observed from the line plot that adding the flare nozzle causes a slight increase in the pressure magnitude throughout the entire pulsejet. This is attributed to the reduced acoustic losses in the system after adding the flare nozzle, which can enhance the engine's performance.

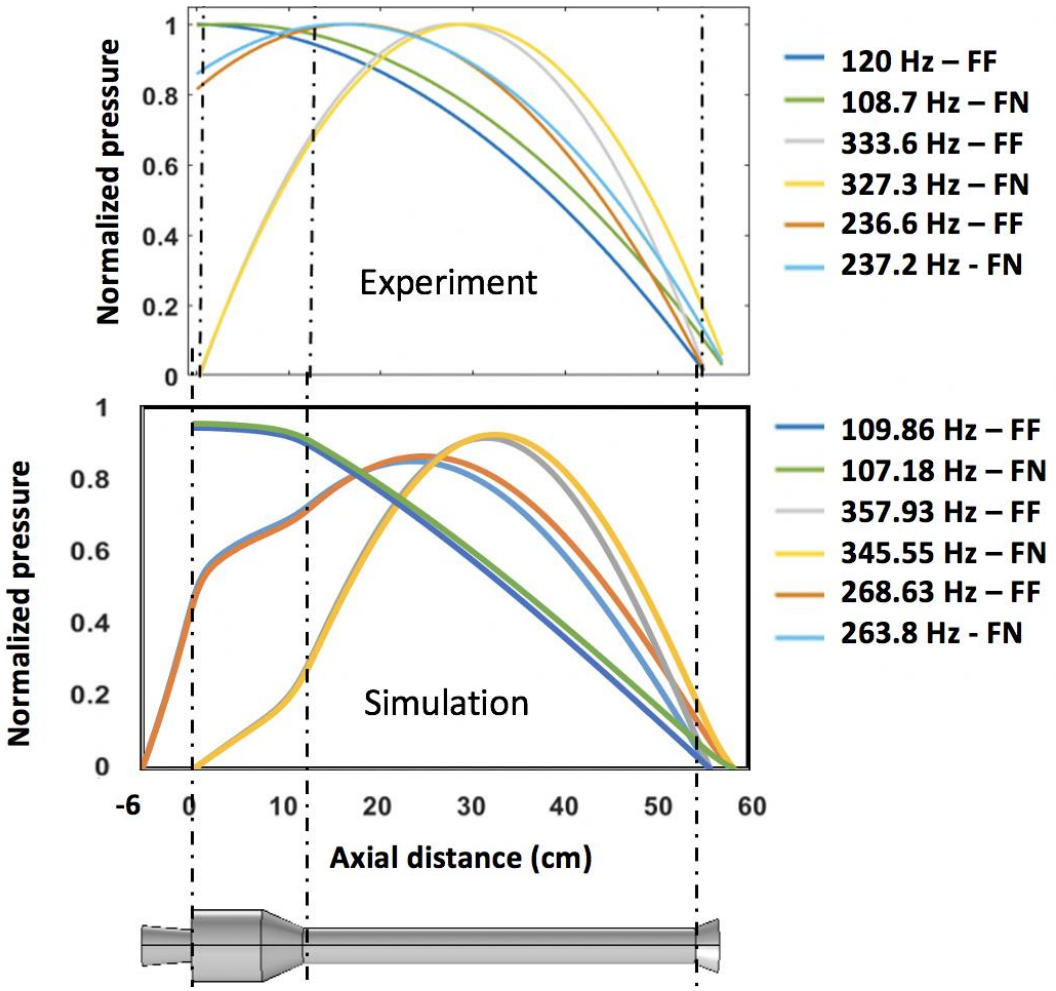

Fig. 4 The pressure field of the fundamental resonance mode from experiment (top) and simulation (bottom) with the three different inlet boundary conditions (close-open: dark blue and green, open-open: gray and yellow, reed valve open-open: orange and light blue) along the pulsejet for the LC-MT-FF/FN configurations.

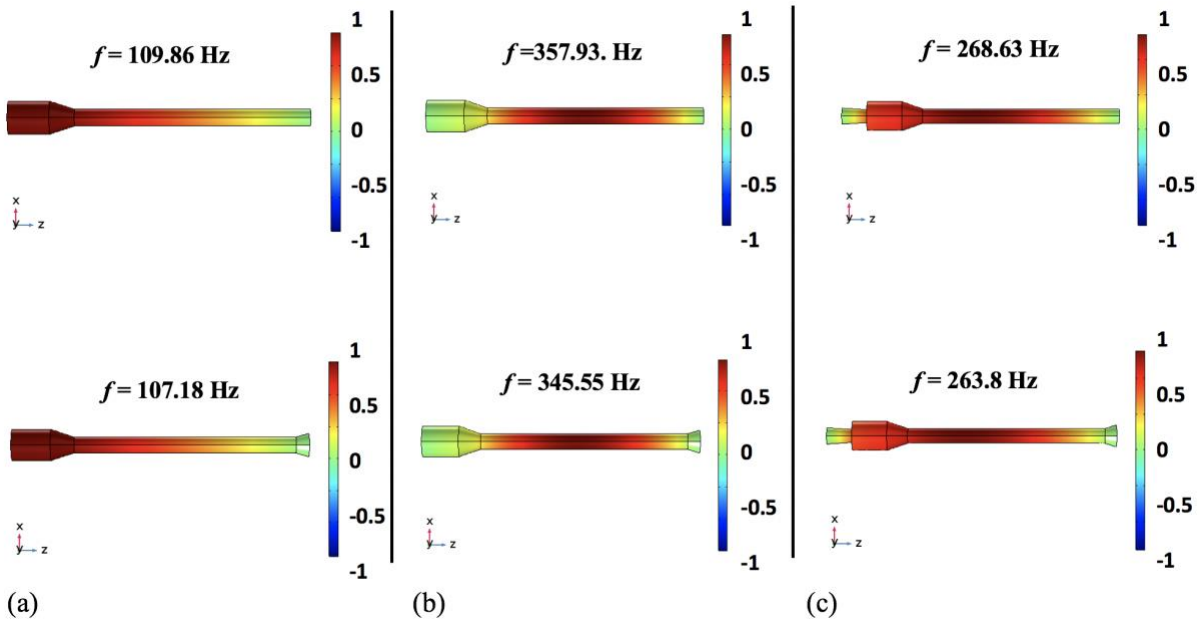

Fig. 5 Surface colored-contour of the acoustic pressure fields of the LC-MT configuration without the flare section (top) and with the flare section (bottom). (a) close-open, (b) open-open, and (c) reed valve open-open.

4.1.2. Acoustic velocity fluctuations

Since the pulsejet engine operates primarily in its resonance mode, and both simulation and experiment have shown good agreement regarding pressure fields and frequencies, it is crucial to explore another aspect of its acoustic nature: velocity fluctuations associated with the resonance mode. Several researchers have highlighted the significance of velocity fluctuations in influencing flame structure in thermoacoustic systems [40–42]. Analyzing velocity fluctuation, a vector quantity, offers the advantage of breaking down the mode into axial, radial, and lateral components. This section discusses results from the LC-MT-FF/FN configuration with close-close boundary conditions, which are more practical than the other two. Iso-surface contours in Fig. 6 of the axial component exhibit behavior opposite to the pressure field, indicating a quarter-wave mode. The axial velocity component drives hot products longitudinally. Notably, the radial and lateral components reveal a new phenomenon: vortex-like structures at the convergent and divergent sections (flare nozzle) of the engine. Therefore, it is hypothesized in this study that these

velocity disturbances can generate vortices in the combustion chamber and additional vortex structures at the flare nozzle lip, which was previously observed by Vijay et al. [32] from their chemiluminescence measurements on a transparent engine, where the upstream vortex structure appeared to be traveling upstream from the convergent section towered the combustion chamber. Additionally, studies have shown that the highest temperature point is near the convergent section, attributed to the vortex structure containing hot combustion products [2,31]. Therefore, it is hypothesized in this study that after the resonance mode is excited by shock waves from fuel ignition, these velocity fluctuations propagate through the flow field, leading to the generation of upstream and downstream vortex structures. These results, to the best of the author's knowledge, are novel and have not been demonstrated in the literature before.

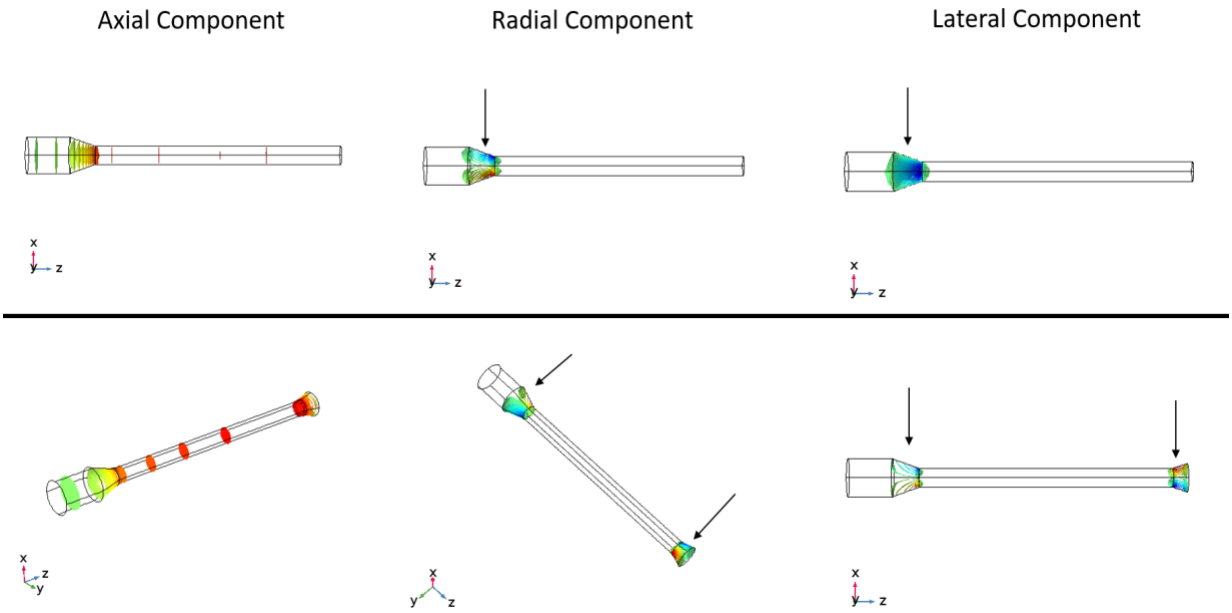

Fig. 6 visualizing the acoustic velocity fluctuations of the close-open case (see Fig.5a) in terms of three directional components (axial, radial, and lateral). Top: without the flare. Bottom: with the flare of the LC-MT case.

4.2. Reacting Pulsejet

4.2.1. Instantaneous fields

The instantaneous results are presented to demonstrate certain pulsejet phenomena and the relationship between pressure and thrust, as well as to highlight the disparities between instantaneous and phase-averaged results. For brevity, the instantaneous results of one examined case, the LC-MT-FF configuration with gasoline, which exhibited the best performance among the configurations, are showcased (see Fig. 7). Peak pressure is observed at the convergent section (sensor 3, yellow line), ranging from ± 0.3 bar, followed by a pressure drop (sensor 4, purple line) at the start of the tailpipe section, where pressure approaches zero. Such pressure behavior might lead some researchers to assume the pulsejet is a Helmholtz resonator; however, overall mode shapes derived from root mean square (RMS) pressure field results, discussed later, illustrate quarter-wave mode behavior. Moreover, a noticeable double-peak in pressure cycles, particularly evident at the convergent section in sensor 3 (yellow line), is observed, potentially related to vortex structure inside the engine causing non-uniform pressure peaks measured by sensors [34]. Pressure and thrust measurements (shown in Fig. 7b) are out of phase, with maximum thrust occurring after the pressure drop with a time lag of around 3.2 milliseconds (ms), indicating ejection of hot products from the engine. Additionally, thrust cycles exhibit several peak behaviors attributed to structural vibrations of the entire rig, given the high sensitivity of the dynamic force sensor, as per prior studies [43–45]. However, averaging (RMS calculation) thrust data still yields an accurate estimate of thrust magnitude [43]. Overall, the sound pressure level (SPL) from microphone measurements across all geometries ranges from 100 to 160 decibels (dB), indicating the presence of shock waves generated inside the engine upon fuel ignition. This study hypothesizes that these shock waves dissipate rapidly after ignition, as evidenced by the sudden pressure drop measured

by the sensor located at the beginning of the tailpipe section. Hence, it can be inferred that explosive fuel ignition excites the resonance mode of the pulsejet engine, with evidence of shock wave generation from fuel ignition detailed in subsequent subsections focusing on operating frequency and mode shape results.

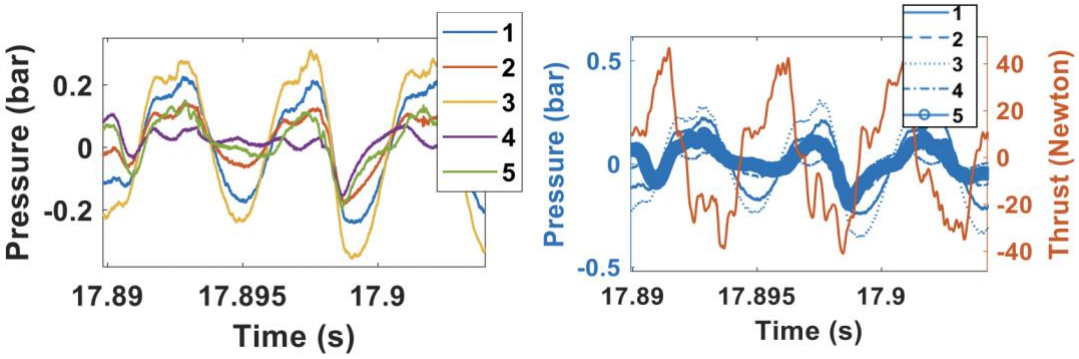

Fig. 7 Time-series of the (a) pressure inside the engine, and (b) pressure vs. thrust. These results are of the LC-MT-FF engine that has the most stable operation.

4.2.2. Operating frequency and mode shape

The reacting pulsejets were operated with gasoline and ethanol to understand the effects of the fuel type on the operating frequency. Operating the engine with ethanol posed challenges, as it only functioned for less than five seconds, a phenomenon referred to in this study as "short-burst" combustion. Additionally, ethanol required pre-heating due to its longer chemical timescale, necessitating a higher temperature environment for rapid ignition. In contrast, running the engine with gasoline proved more stable and sustained operation for longer periods, exceeding 30 seconds. Generally, there was no significant change in the operating frequency values between gasoline and ethanol cases, with differences falling within the range of 10 to 30 Hz (see Table 4). Notably, in the SC-ST-FN case, there was an approximately 86 Hz difference between the two fuels. This case, associated with a short combustor configuration known for instability and shorter sustenance periods, resulted in higher measurement uncertainties.

To determine the mode of the pulsejet engine during the combustion reaction when the reed valve is closed, the measured operating frequency data are compared to the theoretical equations for the quarter-wave mode:

$$f = \frac{c}{4L} \qquad (4)$$

and Helmholtz mode:

$$f = \frac{c}{2\pi}\sqrt{\frac{A}{VL_{eq}}} \qquad (5)$$

Where A is the cross-sectional area of the combustion chamber, is the combined volume of the combustion chamber and convergent section, and L_{eq} is the total length of the engine. Previous heat transfer studies by Blomquist et al. indicated an average uniform temperature of 940 K within the pulsejet, leading to an assumed temperature of 1000 K for calculations [47]. Thus, a trivial error may exist in the calculated frequency values. The theoretical frequencies of the fundamental modes are compared with measured values in Fig.8. It is evident that all measured operating frequencies, using both fuels, are closer to the quarter-wave mode than the Helmholtz mode. These results support the claim made in the previous section regarding acoustic characterization analysis, suggesting that the fundamental mode of the pulsejet engine is a quarter-wave mode when the reed valve is closed.

Table 4. The operating frequency values measured by the first PCB pressure sensor located at the beginning of the combustion chamber for all twelve cases using gasoline and ethanol.

Configuration	Frequency (Hz) - Gasoline	Frequency (Hz) - Ethanol
SC-ST-FF	328.2	350.4
SC-ST-FN	366.8	280.1
LC-ST-FF	251.4	266.7
LC-ST-FN	245.4	244.5
SC-MT-FF	262.0	227.3
SC-MT-FN	223.5	218.8
LC-MT-FF	210.9	200.1
LC-MT-FN	190.7	200.0
SC-LT-FF	182.5	190.9
SC-LT-FN	168.5	166.7
LC-LT-FF	162.8	181.9
LC-LT-FN	154.7	159.1

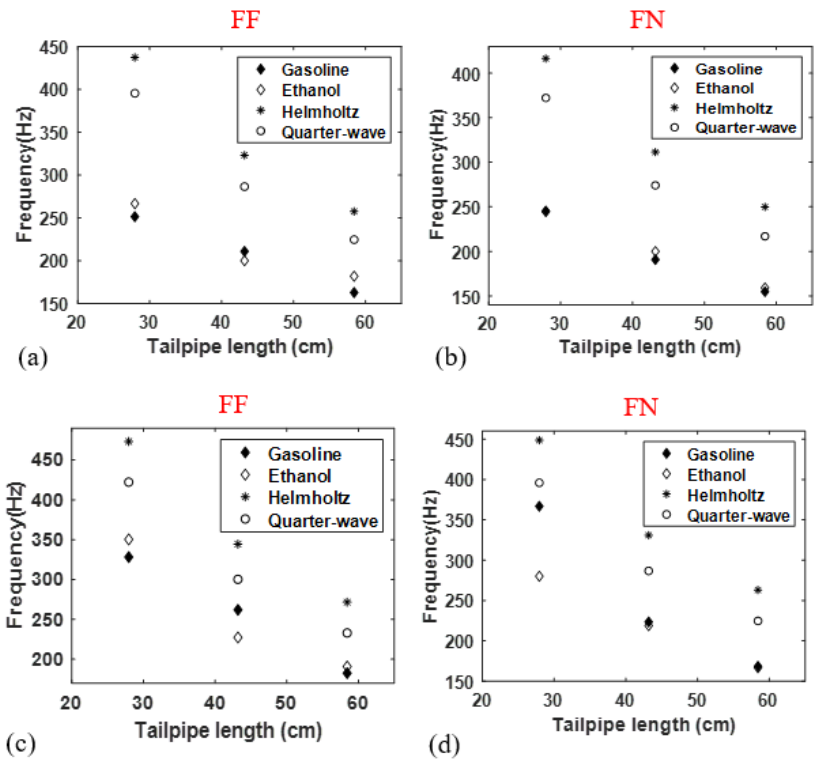

Fig. 8 The frequency values of the long combustor (a) without flare, (b) with flare, and the short combustor (c) without flare, and (d) with flare.

The mode shapes are illustrated for ethanol (Fig. 9) and gasoline (Fig. 10) based on the RMS pressure values obtained from the five PCB sensors inside the engine, normalized by the maximum pressure value among all configurations. Generally, all ethanol cases exhibit higher pressure fields compared to their gasoline counterparts, attributed to the "short-burst" combustion behavior where the engine barely sustains for less than five seconds. An intriguing observation is that all cases show a sudden increase in the pressure field after the first sensor, located at the beginning of the combustion chamber, with the maximum pressure occurring at the third sensor positioned at the convergent section. This sudden pressure surge (mostly in the range of 0.3 bar) indicates shock waves generated from fuel ignition. Furthermore, a significant pressure drop is recorded by the fourth sensor at the start of the tailpipe section in most cases. The pressure drop is caused by geometrical constraints; post-ignition, the hot products accelerate as they transition from a larger area (combustion chamber) to a smaller one (tailpipe section) due to deflagration flame behavior, which indicates the quick dissipation of the shock waves generated initially from fuel ignition. However, as the total length reduced when using the short combustor with gasoline fuel, the combustion region in the SC-MT-FF/FN and SC-LT-FF/FN cases pushed downstream to the beginning of the tailpipe section (see Fig. 10c and d), thus preventing a higher rate of acceleration of hot products and eliminating the pressure drop. Moreover, adding the flare nozzle increases pressure fields in all cases with both fuels, consistent with observations from the previously discussed acoustics study. These results underscore that the engine operates as a quarter-wave tube rather than a Helmholtz resonator, and the sudden pressure increase followed by a drop, often interpreted as indicative of Helmholtz resonator behavior, is primarily due to fuel ignition and the engine's geometrical constraints.

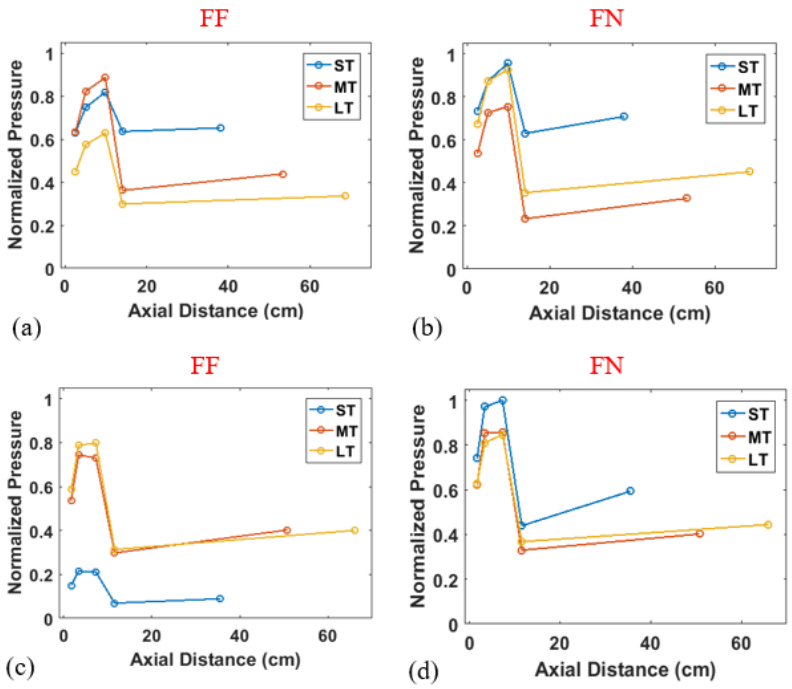

Fig. 9 Mode-shape plots based on the RMS pressure obtained from the five sensors inside the engine using ethanol. (a) LC without flare, (b) LC with flare, (c) SC without flare, and (d) SC with flare.

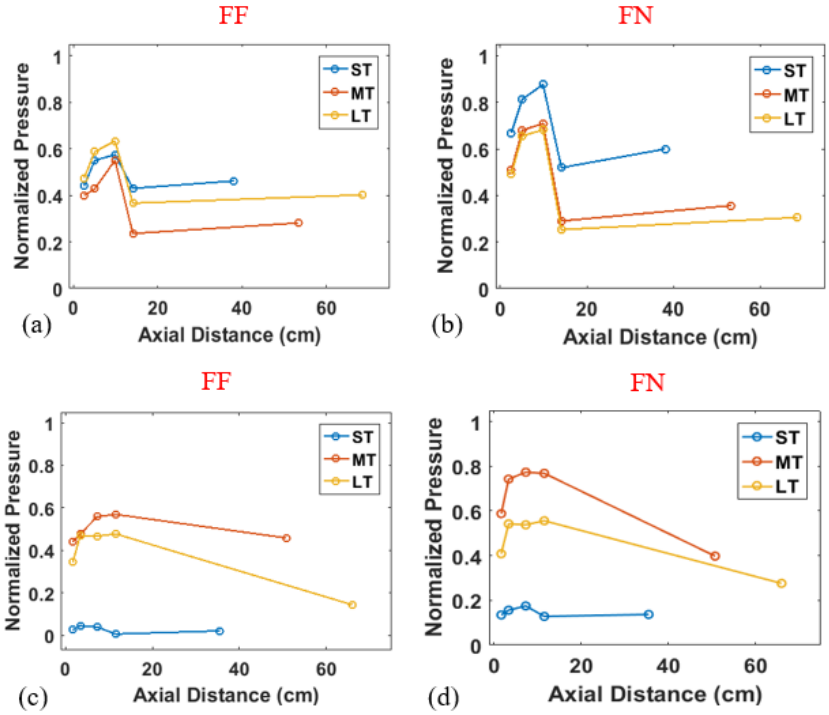

Fig. 10 Mode-shape plots based on the RMS pressure obtained from the five sensors inside the engine using gasoline. (a) LC without flare, (b) LC with flare, (c) SC without flare, (d) and SC with flare.

4.2.3. Engine stability and types of operation

The following analysis of this paper will be based on the results obtained from the gasoline campaign, considering the engine's sustainability over gasoline. Dominant frequencies are determined and compared using FFT and spectrogram methods across all five PCB sensors inside the engine, the microphone, and the dynamic force sensor measuring thrust. The FFT calculates the discrete Fourier transform (DFT) of the measured data in the frequency domain, while the spectrogram, or "Short-time Fourier Transform," is employed to analyze how the frequency content of a nonstationary signal changes over time, providing temporal information about dominant frequency behavior.

The FFT results of the pressure measurements from the first sensor located in the combustion chamber are depicted in Fig. 11, showcasing three different types of operations identified in our study. The first type of pulsejet operation, termed "resonance stable," features higher harmonic modes alongside the operating frequency mode, the latter being significantly larger in amplitude. The second type, labeled "resonance unstable" operation, shows higher harmonic modes with a relatively larger amplitude and low-frequency modes. The third type, termed "not purely" resonance operation, introduces low-frequency modes, with the absence of higher harmonics.

To further elucidate the phenomena of higher harmonic modes and low-frequency mode instability, spectrogram results are generated for the first pressure sensor at the combustion chamber, the fifth pressure sensor at the end of the tailpipe section (tailpipe 2), microphone, and thrust (see Fig. 12, 13, and 14). Only the first and fifth pressure sensors, denoted by PCB-chamber 1 and PCB-tailpipe 2, are selected to understand the frequency behavior inside the engine. In the resonance operation cases (Fig. 12 and 13), higher harmonics are observed both inside and outside the engine, as well as on the thrust data. Moreover, in resonance stable operation, the operating

frequency emerges as the dominant mode, while in unstable resonance operation, the operating frequency mode is not always dominant, leading to competition with higher harmonics and consequently, unstable pulsejet operation. Conversely, in the "not purely" resonance operation case in Fig. 14, higher harmonics do not appear inside the engine, with low-frequency modes becoming apparent instead. These low-frequency modes are theorized by some researchers to be related to auto-ignition events occurring arbitrarily [30, 32]. The discrepancy in the frequency profile between inside the engine (chamber 1 and tailpipe 2) and outside the engine (microphone) suggests that the low-frequency modes are associated with phenomena occurring solely inside the engine, thereby interfering with the operating frequency mode and introducing instability into the system. Nonetheless, even during resonance stable operation (LC-MT-FF), the dominant frequency does not remain constant throughout the entire engine. Our results demonstrate that the dominant frequency at the combustion chamber (sensor 1) differs from that measured at the beginning of the tailpipe (sensor 4), as highlighted by the red dashed box in Fig. 15. The appearance of low-frequency modes at the beginning of the tailpipe is attributed to fluctuations caused by sudden pressure drops or increases as the hot products accelerate or decelerate, transitioning from larger to smaller areas and vice versa.

The stability of pulsejet engines is characterized by frequency consistency among four types of measurements (first sensor - chamber 1, fifth sensor - tailpipe 2, microphone, and thrust) and the fluctuation of frequency values represented by error bars (see Fig. 16). Generally, as the total length increases, frequency discrepancies reduce. Short tailpipe cases for both long and short combustors (with and without flare) exhibit the most significant discrepancies in frequency values, with total engine lengths ranging from 33 to 38 cm. On the contrary, the long tailpipe region (total length from 63 to 68 cm) shows more consistent frequencies, albeit with relatively high error bars.

The medium tailpipe (total length ranging from 48 to 53 cm) is the least variable region, where dominant frequencies are consistent, and frequency fluctuations are relatively lower compared to short and long tailpipe regions. Furthermore, configurations with the best performance, characterized by the highest thrust (LC-MT-FF with a total length of 50.8 cm), exhibit the smallest error bar values of measured frequencies across all measurements, with exact same dominant frequencies. These results demonstrate a method for understanding pulsejet engine stability by analyzing the consistency of dominant frequencies inside and outside the engine and the variability of dominant frequency values. To validate this characterization method, one can observe similarities in these factors among cases with similar thrust magnitudes, as indicated in Fig. 16.

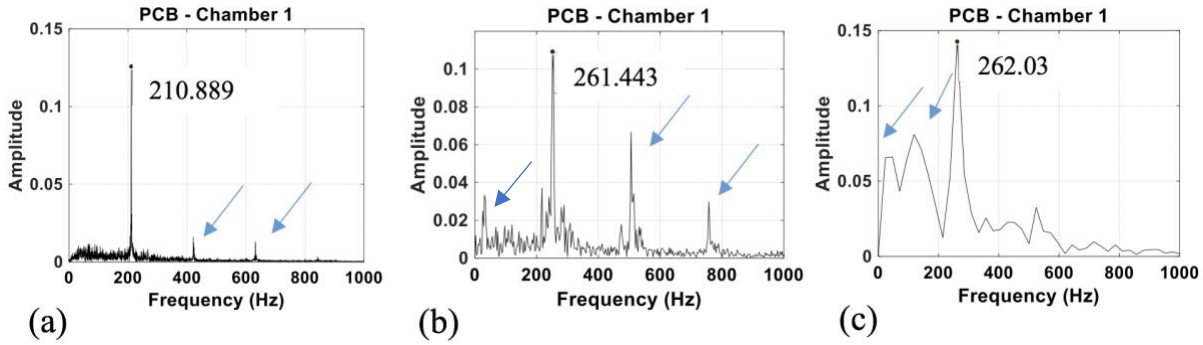

Fig. 11 FFT results of the pressure measurements located at the combustion chamber (sensor 1) for the (a) resonance stable operation – LC-MT-FF, (b) resonance unstable – LC-ST-FF, and (c) not purely resonance unstable operation – SC-MT-FF. Blue arrows are used to indicate the higher harmonics and low-frequency instability modes.

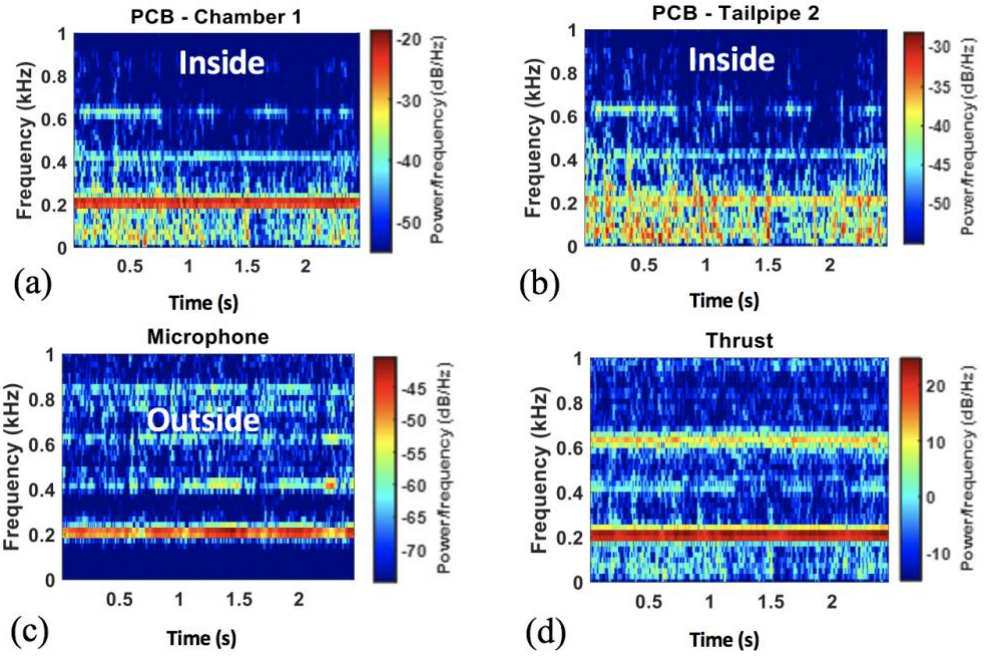

Fig. 12 Spectrogram results of the resonance stable operation - LC-MT-FF case of the (a) first pressure sensor, (b) fifth pressure sensor, (c) microphone, and (d) thrust.

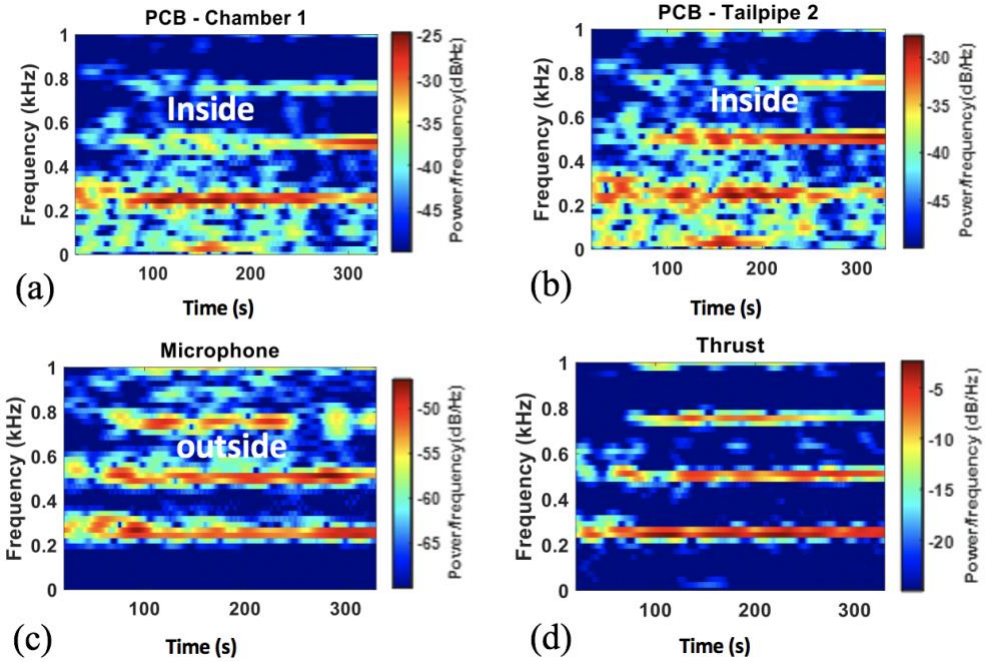

Fig. 13 Spectrogram results of the resonance unstable operation - LC-ST-FF case of the (a) first pressure sensor, (b) fifth pressure sensor, (c) microphone, and (d) thrust.

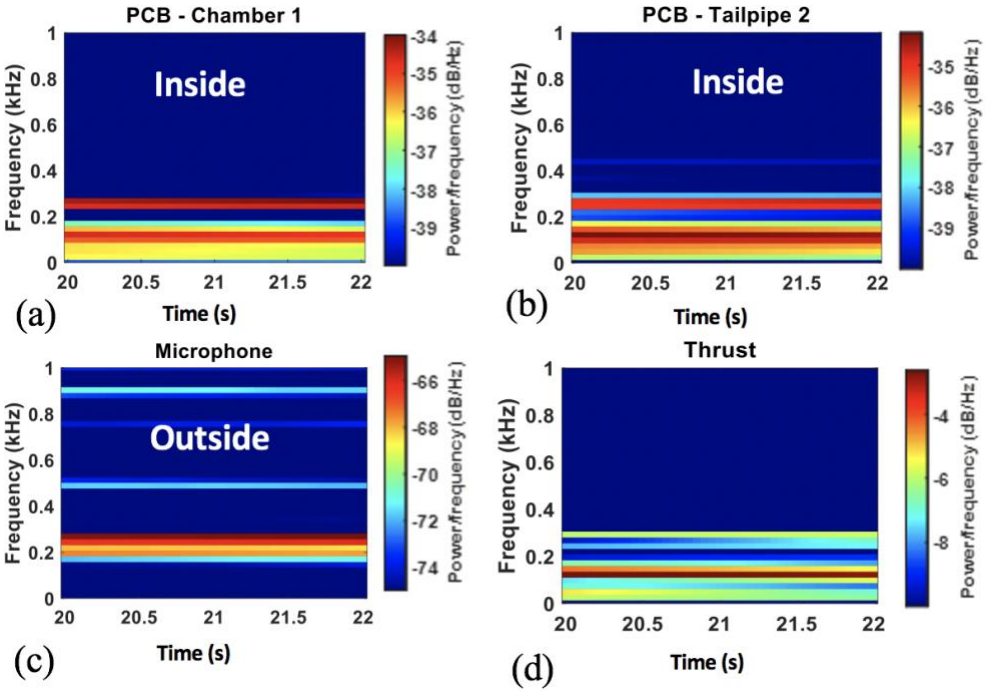

Fig. 14 Spectrogram results of the "not purely" resonance unstable operation - SC-MT-FF case of the (a) first pressure sensor, (b) fifth pressure sensor, (c) microphone, and (d) thrust.

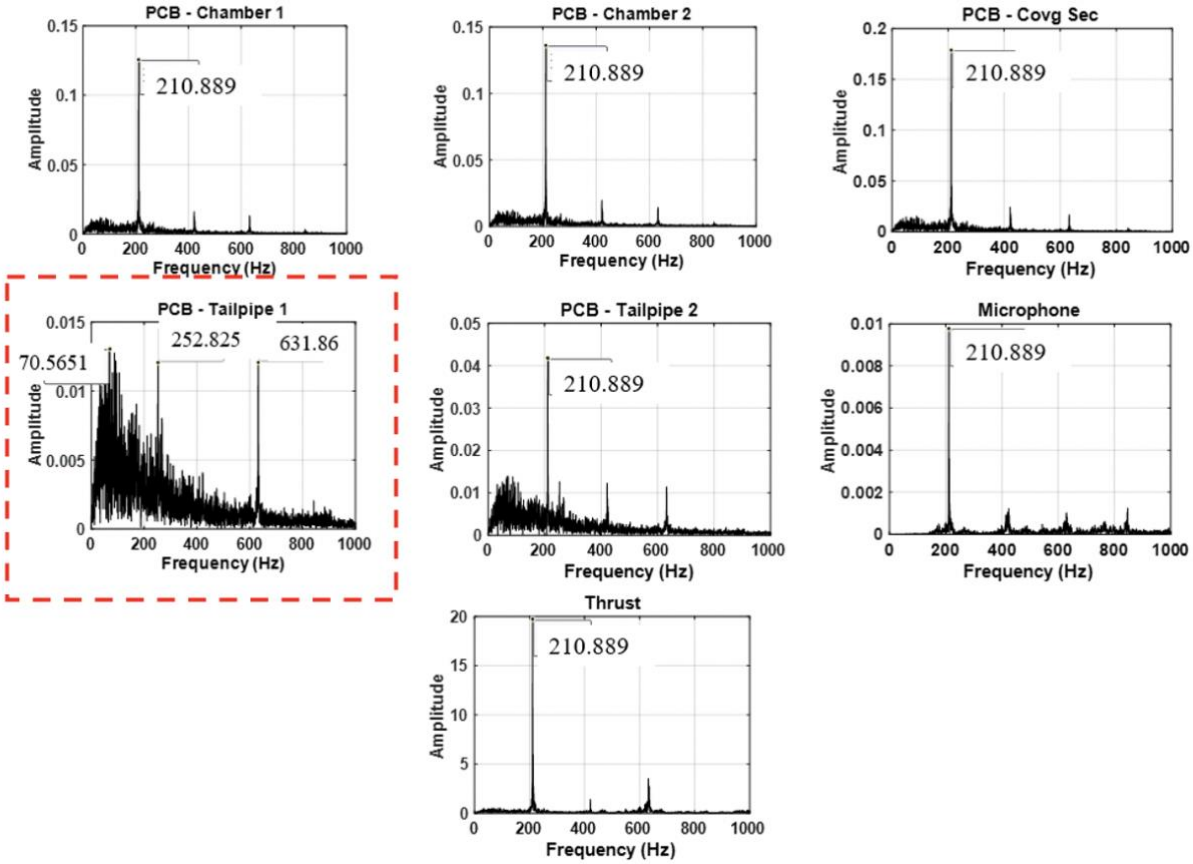

Fig. 15 FFT results of the five pressure sensors, microphone, and thrust for the resonance stable operation of the LC-MT-FF case.

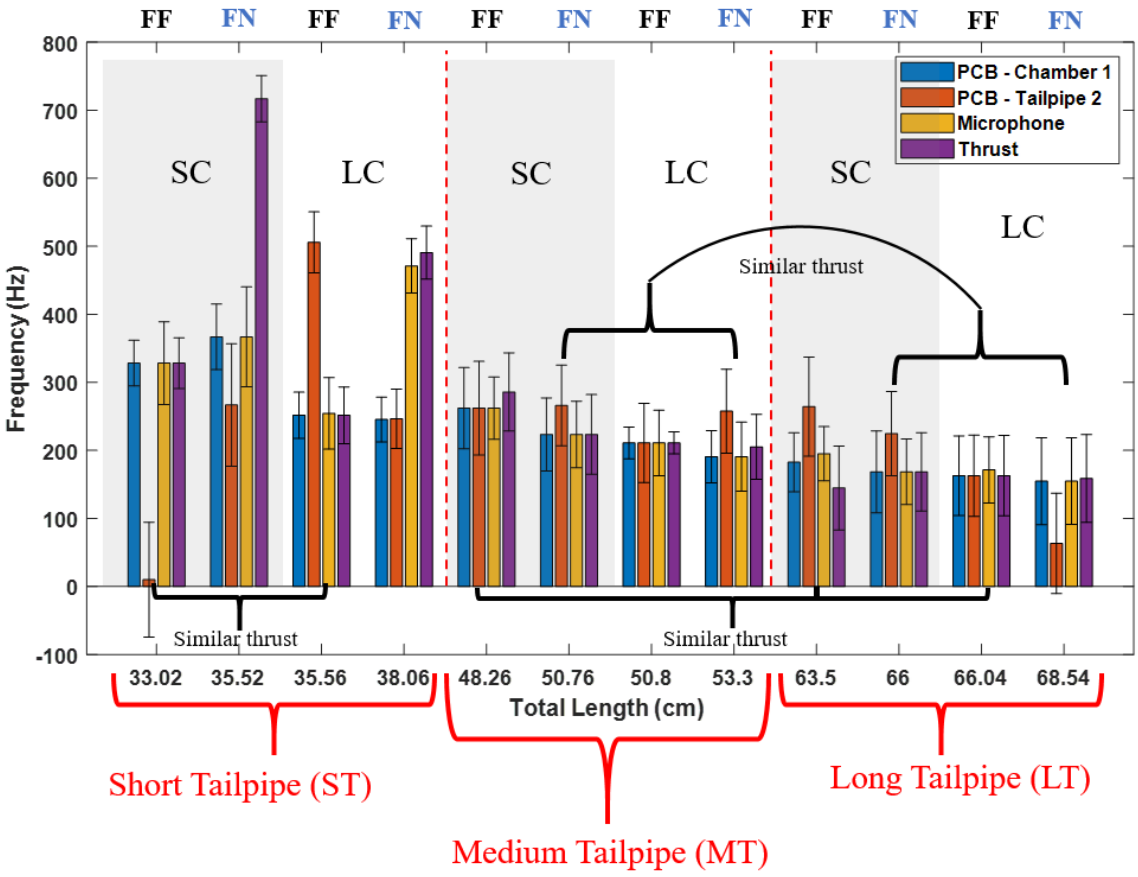

Fig. 16 The measured dominant frequencies of the first pressure sensor (PCB – Chamber 1), fifth pressure sensor (PCB – Tailpipe 2), microphone, and thrust for all the twelve cases with gasoline fuel.

4.2.4. Phase-averaged analysis

The phase-averaged method is adopted from the framework of Luzan et al. [48]. We begin by phase-referencing every pressure data point, first identifying the minimum and maximum data points within each instantaneous cycle (see Fig.17). Subsequently, the dataset is segmented into individual cycles, and a moving mean is applied that is illustrated in Fig.18. Following this, phase angles are computed using the mathematical expression:

$$\theta_i = \frac{t_i - t_{0^o}}{t_{360^o} - t_{0^o}} \, x \, 360^o \qquad (6)$$

Here t_i corresponds to the time of a selected phase θ_i, t_{0^o} refers to the zero-degree phase at the cycle's outset, and t_{360^o} denotes to the 360-degree phase at the cycle's end. This calculation is

independently applied to each of the five pressure sensors and the thrust data as illustrated in Fig.19. The data from the first pressure sensor serve as the reference for the entire phase-averaged analysis.

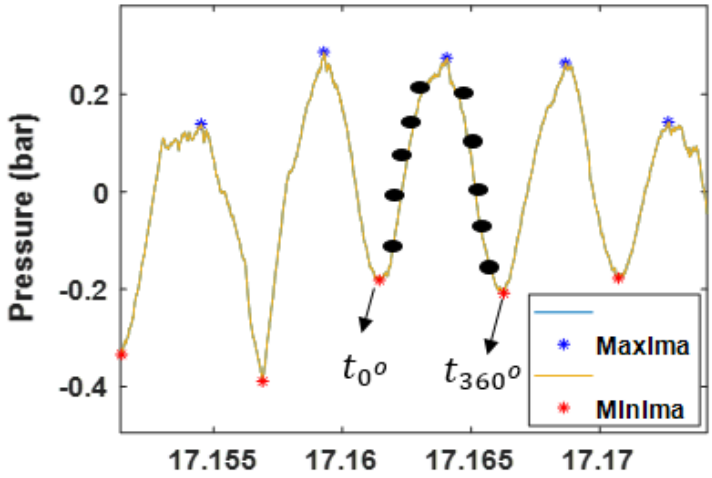

Fig. 17 The minimum and maximum data points are identified on the raw data for each instantaneous cycle. The beginning of the cycle at zero degree (t_{0^o}), and the end of the cycle at 360 degree (t_{360^o}).

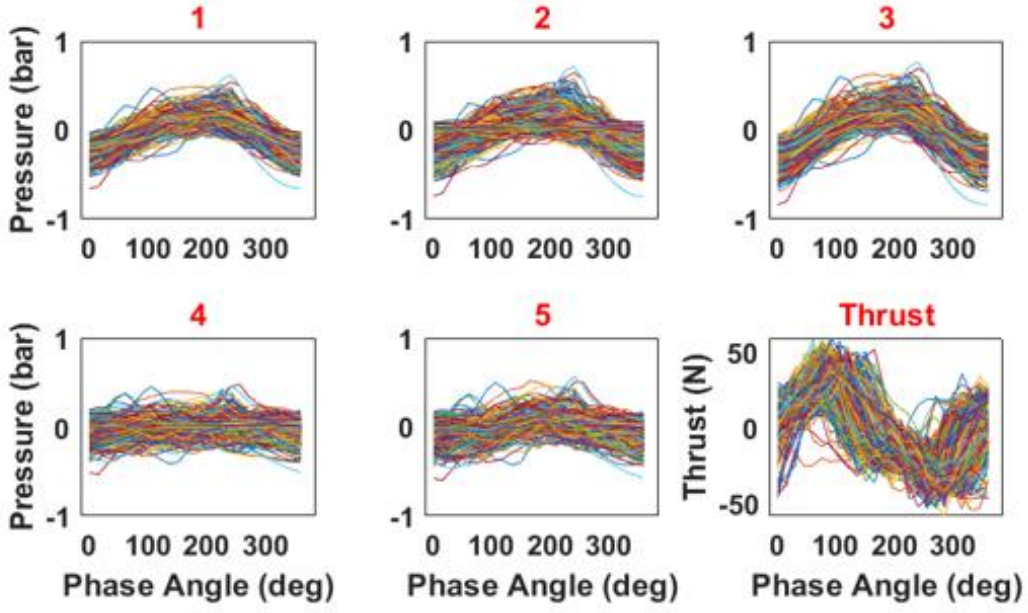

Fig. 18 Illustration of the broken cycles of the five pressure sensors (1 through 5) and thrust raw data of the LC-MT-FF case that composes of 523 cycles.

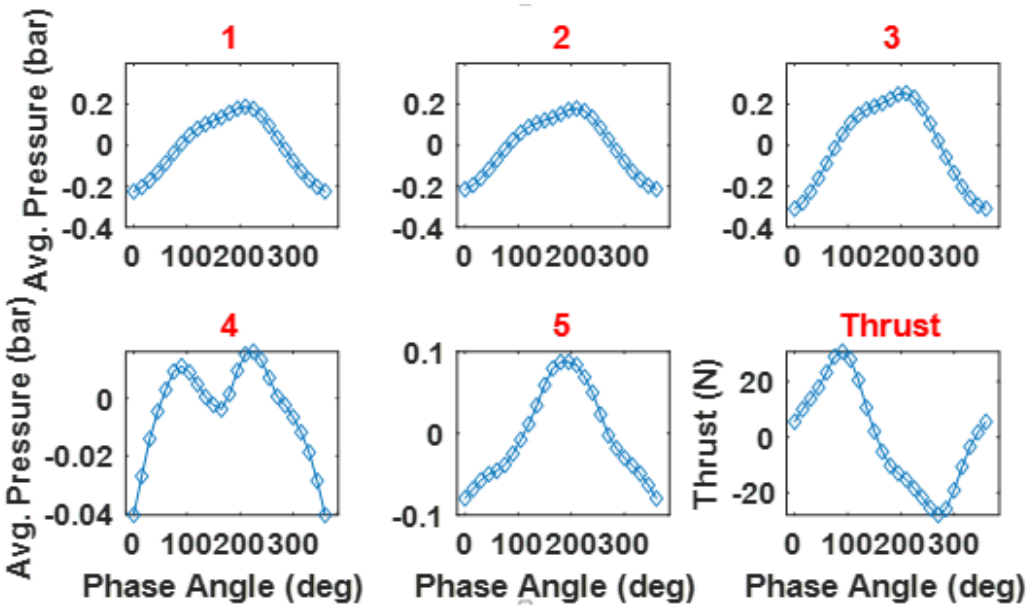

Fig. 19 Illustration of the phase-averaged obtained by using Eq.6 of the five pressure sensors (1 through 5) and thrust data of the LC-MT-FF case.

The phase-averaged results of pressure versus thrust for the three types of operations are presented in Fig. 20. In resonance operations (stable/unstable), the thrust exhibits an out-of-phase relationship with the pressure waves. However, in the stable case, the thrust profile appears smoother and yields higher thrust values, while the unstable case demonstrates significantly lower thrust magnitudes and more chaotic behavior. Conversely, in the "not purely" resonance case, the thrust aligns with the pressure wave and displays a chaotic profile with lower thrust production. Moreover, one can observe the point of maximum thrust indicated by the dashed black line. In the resonance stable case, thrust reaches its maximum value when the pressure field is close to zero across the entire engine, whereas it peaks during the under-pressure phase for unstable resonance operation and during the over-pressure phase for the not purely resonance operation. The time lag between peak pressure and peak thrust depends on the overall length of the engine, as will be discussed later. Interestingly, these new phase results reveal that thrust produced by the pulsejet engine is not solely dependent on the pressure rise due to combustion. This is evident in Fig. 17,

where the peak pressure magnitude (around 0.3 bar) remains similar among both stable and unstable operations, yet the thrust produced varies significantly.

The plot in Fig. 21 provides detailed insight into the evolution of the pressure field for seven phase degrees of the LC-MT-FF case, with associated thrust values presented at each phase degree. We observe that the maximum thrust (30 Newton) occurs at 90 degrees, coinciding with a pressure field throughout the engine that is nearly zero as the hot products are completely ejected, inducing forward motion of the pulsejet engine, thereby applying a compression force on the force sensor. The negative sign indicates the force released by the force sensor, which essentially functions as a spring/mass system. Upon the removal of the compression force from the forward motion of the engine, the signal turns negative, equaling the applied load, as the sensor seeks equilibrium. For this particular configuration, there is a 240-degree phase lag (or 3.2 ms time lag) between the maximum pressure (at 210 degrees) and maximum thrust (at 90 degrees). These results are crucial in revealing that an optimally self-aspirated valved-pulsejet engine produces maximum thrust after the fuel re-filling process of the subsequent cycle, when pressure is balanced with a zero value across the entire engine and the backflow induced by the expansion wave (reflective wave) from the open-end exhaust reaches the combustion chamber, rather than immediately after the pressure drop following the combustion event. In fact, the negative sign of the thrust values during the pressure rise, when combustion occurs (from 180 degrees to 330 degrees), indicates no compression force is applied on the force sensor, and forward motion of the engine begins at 360 degrees when pressure inside the combustion chamber is below atmospheric pressure.

The time lag between the pressure peak and thrust peak is presented in Fig. 22. The general trend indicates that as the total length increases, the time lag also increases, inversely correlated with the operating frequencies. However, there is no obvious correlation between the time lag and

thrust value. In Fig. 23, the maximum thrust values from the phase-averaged calculation and RMS of the thrust are shown. Thrust is enhanced as the total length of the engine increases through the enlargement of the combustor size, lengthening of the tailpipe, and addition of the flare. Among these three geometrical factors, the length of the tailpipe has a significant impact on the thrust magnitude. Moreover, the plot illustrates the RMS calculation of the thrust, commonly used in literature as a method to represent thrust data, generally over-predicting thrust magnitudes (except for the LC-MT-FF case). Remarkably, different engine configurations with varying operating frequencies produce the same amount of thrust (indicated by the dotted red line), which typically exhibits a similar behavior as mentioned previously in the frequency profile in Fig. 16. Thus, this new finding suggests that engineers can design smaller, lighter, and cost-efficient pulsejet engines that achieve the same thrust produced by larger engines.

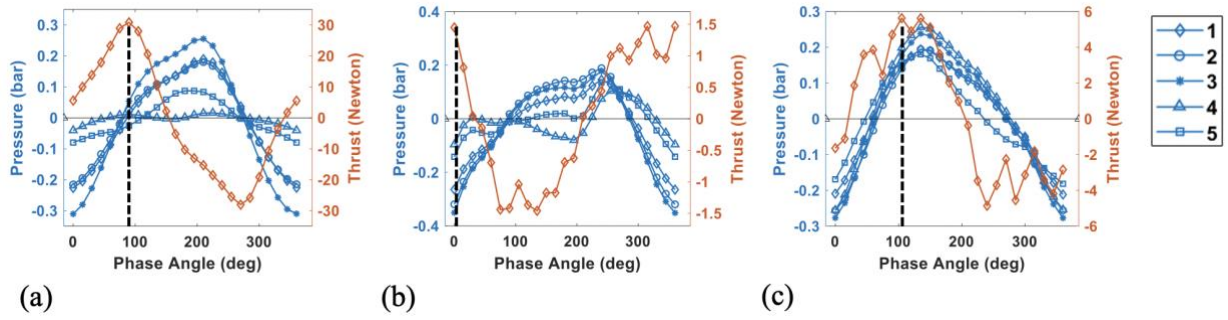

Fig. 20 Phase-averaged results of the (a) resonance stable operation -LC-MT-FF, (b) resonance unstable operation – LC-ST-FF, and (c) not purely resonance unstable operation – SC-MT-FF.

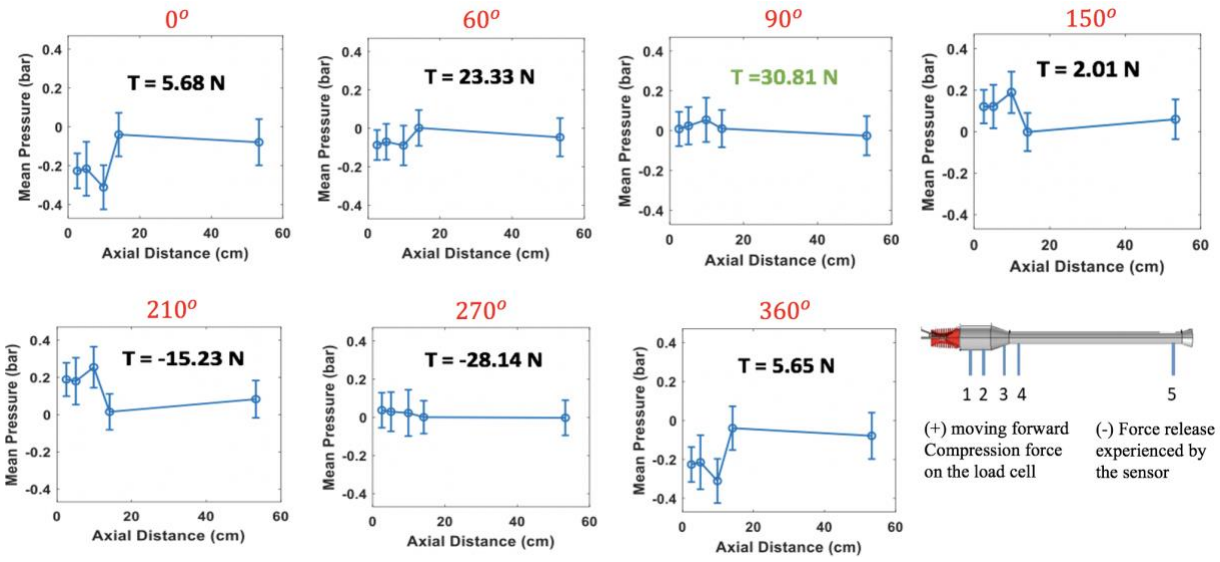

Fig. 21 The pressure field evolution with the thrust values for a complete pulsejet cycle of the LC-MT-FF configuration.

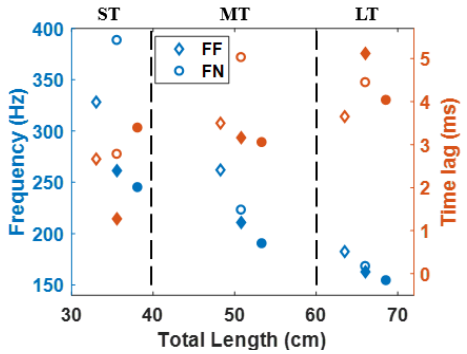

Fig. 22 The operating frequencies vs. the time lag between the pressure and thrust peaks. The Empty symbols for the long combustor and filled symbols for the short combustor.

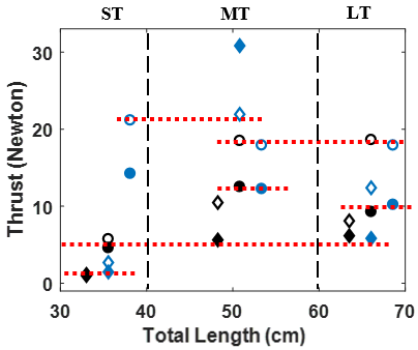

Fig. 23 The maximum thrust values (filled symbols) obtained from the phase-averaged and thrust RMS (empty symbols) values. The black color indicates the short combustor, and blue color indicates the long combustor cases. Diamonds – FF, and Circles – FN. The red line highlights the cases having similar thrust.

5. Conclusion

The study delves into the Curtis-Dyna self-aspirated valved-pulsejet across twelve configurations, analyzing both non-reacting and reacting modes. In the initial phase, acoustic analysis examines resonance modes under various inlet conditions. It uncovers that the close-open configuration exhibits a quarter-wave mode, simulating scenarios during combustion. Conversely, an open reed-valve case shifts to a half-wave mode, extending the engine's effective acoustic length upstream. Further investigation into velocity fluctuations reveals vortex-like patterns at key sections (convergent and flare nozzle sections), potentially influencing flow dynamics.

The subsequent segment scrutinizes reacting pulsejets, focusing on pressure dynamics, sound measurements, and thrust amplitude. Notably, fuel type – gasoline or ethanol – shows minimal impact on operating frequency but significantly alters engine stability. Ethanol usage results in shorter operational periods due to its longer chemical time scale. Moreover, ethanol-fueled engines exhibit higher pressure fields, attributed to short-burst behavior. Despite these variations, both fuels drive the engine as a quarter-wave tube, with operating frequencies aligning closer to theoretical quarter-wave values. A noteworthy observation is that in all cases, there is a sudden surge in the pressure field after passing the first sensor, situated at the entrance of the combustion chamber, with the maximum pressure occurring at the third sensor located at the convergent section. The sudden increase in the pressure field, usually around 0.3 bar, signifies the generation of shock waves triggered by the ignition of the fuel, acting as an excitation mechanism for the resonance mode of the system. These shock waves dissipate rapidly, as demonstrated by the abrupt pressure drop measured at the beginning of the tailpipe section.

Engine stability is evaluated concerning tailpipe length and combustor configurations, with longer lengths and flare nozzle aiding stability. Short tailpipes consistently exhibit coherence

between operating frequencies and thrust, emphasizing the tailpipe's critical role in engine performance. Lengthening the engine enhances stability, with the medium tailpipe region identified as optimal. Notably, long combustor cases outperform short ones, with stable cases demonstrating thrust outputs up to 30 Newtons. Low-frequency instability modes, observed exclusively inside the engine, potentially disrupt acoustics and introduce losses, particularly in short combustor configurations. Resonance operation introduces higher harmonics, impacting thrust production. Stable resonance operation, such as the LC-MT-FF case, demonstrates dominance of the operating frequency over higher harmonics. However, instability arises when higher harmonics compete with the operating frequency.

The phase-averaged analysis reveals a time lag between peak pressure and maximum thrust, positively correlated with engine length. These results demonstrated that an optimally self-aspirated valved-pulsejet engine achieves maximum thrust after the refueling process of the subsequent cycle, when pressure is balanced to zero across the entire engine and the backflow from the exhaust reaches the combustion chamber, rather than immediately after the combustion event. The new phase-averaged results also reveal that the thrust generated by the pulsejet engine does not solely depend on the pressure increase resulting from combustion. Despite similar peak pressure magnitudes (around 0.3 bar) observed in both stable and unstable operations, there is significant variation in the produced thrust. In summary, the study provides valuable insights into the acoustic and dynamic behavior of pulsejet engines under various conditions, offering opportunities for optimization in design and performance. Different engine configurations with varying operating frequencies could produce similar thrust amplitudes, enabling size and cost-efficient designs.

6. Contributions

The significant contributions of this study can be summarized as follows:

1. The acoustic modes of the engine are determined under different inlet boundary conditions.
2. The study hypothesizes the mechanisms behind the vortex structures generated inside and outside the pulsejet engine.
3. The stability of the pulsejet engine is characterized by analyzing the measured frequency of the internal pressure, the sound measured outside, and the thrust produced.
4. The interference of the low-frequency and higher harmonic modes and their impact on engine performance are explained.
5. The study examines how the pressure rise from the combustion event translates into thrust by analyzing phase-averaged results.
6. The study demonstrates how engines with different operating frequencies can produce similar amounts of thrust despite having comparable pressure rise magnitudes, which can inform the design of more cost-effective pulsejet engines.

References

[1] J. Skorupa, Military airlift catching the next wave, in: AIAA\ICAS International Air and Space Symposium and Exposition: The Next 100 Years, American Institute of Aeronautics and Astronautics Inc., 2003. https://doi.org/10.2514/6.2003-2747.

[2] T. Geng, M.A. Schoen, A. V. Kuznetsov, W.L. Roberts, Combined numerical and experimental investigation of a 15-cm valveless pulsejet, Flow Turbul Combust 78 (2007) 17–33. https://doi.org/10.1007/s10494-006-9032-8.

[3] W.R. Hawthorne, R. Tom Sawyer Award lecture. Reflections on United Kingdom aircraft gas turbine history, Transactions - ASME: Journal of Engineering for Gas Turbines & Power 116 (1994). https://doi.org/10.1115/1.2906848.

[4] A.H. Lefebvre, D.R. Ballal, Gas Turbine Combustion : Alternative Fuels and Emissions, Third Edition, CRC Press, 2010. https://doi.org/10.1201/9781420086058.

[5] D.E. Paxson, T. Kaemming, The Influence of Unsteadiness on the Analysis of Pressure Gain Combustion Devices, J Propuls Power 30 (2013) 377–383. https://doi.org/10.2514/1.B34913.

[6] C.M. Ward, R.J. Miller, Performance Analysis of an Ejector Enhanced Pressure Gain Combustion Gas Turbine, (2012). https://doi.org/10.2514/6.2012-772.

[7] S.M. Jones, D.E. Paxson, Potential Benefits to Commercial Propulsion Systems from Pressure Gain Combustion, (n.d.). https://doi.org/10.2514/6.2013-3623.

[8] D.E. Paxson, T.A. Kaemming, Foundational Performance Analyses of Pressure Gain Combustion Thermodynamic Benefits for Gas Turbines, (2023). https://doi.org/10.2514/6.2012-770.

[9] Y. Matsutomi, S. Heister, Entropy Considerations on Integration of Pressure Gain Combustors, in: 2010. https://doi.org/10.2514/6.2010-6707.

[10] C.D. Porter, Valveless-gas-turbine combustors with pressure gain, in: Proceedings of the ASME Turbo Expo, 1958. https://doi.org/10.1115/58-GTP-11.

[11] J.A.C. Kentfield, L.C.V. Fernandes, Improvements to the performance of a prototype pulse, pressure-gain, gas turbine combustor, J Eng Gas Turbine Power 112 (1990). https://doi.org/10.1115/1.2906479.

[12] J.A.C. Kentfield, A. Rehman, J. Cronje, Performance of pressure-gain combustors without moving parts, Journal of Energy 4 (1980). https://doi.org/10.2514/3.62460.

[13] J.A.C. Kentfield, M.J. O'Blenes, Small gas turbine using a second-generation pulse combustor, J Propuls Power 6 (1990). https://doi.org/10.2514/3.23247.

[14] J.A.C. Kentfield, B.C. Speirs, A multiple-inlet core for gas turbine, pulse, pressure-gain combustors, in: Proceedings of the ASME Turbo Expo, 1991. https://doi.org/10.1115/91GT304.

[15] J.A.C. Kentfield, The Shrouding of Highly Loaded, Aerovaived Pulse, Pressure-Gain Combustors, Combustion Science and Technology 94 (1993). https://doi.org/10.1080/00102209308935302.

[16] J.A.C. Kentfield, M. O'Blenes, Methods for achieving a combustion-driven pressure gain in gas turbines, J Eng Gas Turbine Power 110 (1988). https://doi.org/10.1115/1.3240195.

[17] D. Paxson, K. Dougherty, Ejector Enhanced Pulsejet Based Pressure Gain Combustors: An Old Idea With a New Twist, in: 2005. https://doi.org/10.2514/6.2005-4216.

[18] D.E. Paxson, K. Dougherty, Operability of an ejector enhanced pulse combustor in a gas turbine environment, in: 46th AIAA Aerospace Sciences Meeting and Exhibit, 2008. https://doi.org/10.2514/6.2008-119.

[19] E.J. Manganiello, M.F. Valerli10, R.H. Essig, Sea-level Performance Tests of a 22-inch-diameter Pulse-jet Engine at Various Simulated Ram Pressures, (1945).
[20] A.A. Putnam, F.E. Belles, J.A.C. Kentfield, Pulse combustion, Prog Energy Combust Sci 12 (1986) 43–79. https://doi.org/10.1016/0360-1285(86)90013-4.
[21] J.C. Lisanti, X. Zhu, W.L. Roberts, Improving the performance of an active valve resonant pulse combustor, in: AIAA Propulsion and Energy Forum and Exposition, 2019, 2019. https://doi.org/10.2514/6.2019-3871.
[22] J.C. Lisanti, X. Zhu, T.F. Guiberti, W.L. Roberts, Active Valve Resonant Pulse Combustor for Pressure Gain Combustion Applications, J Propuls Power 38 (2022) 171–180. https://doi.org/10.2514/1.B38226.
[23] X. Zhu, J.C. Lisanti, T.F. Guiberti, W.L. Roberts, Stability Characteristics of an Actively Valved Resonant Pulse Combustor, J Eng Gas Turbine Power 145 (2023). https://doi.org/10.1115/1.4056456.
[24] T. Geng, F. Zheng, A. V. Kuznetsov, W.L. Roberts, D.E. Paxson, Comparison between numerically simulated and experimentally measured flowfield quantities behind a pulsejet, Flow Turbul Combust 84 (2010) 653–667. https://doi.org/10.1007/s10494-010-9247-6.
[25] T. Geng, F. Zheng, A. V. Kuznetsov, W.L. Roberts, Numerical simulation on the effect of starting vortex ring on pulsejet thrust, in: Collection of Technical Papers - 43rd AIAA/ASME/SAE/ASEE Joint Propulsion Conference, 2007. https://doi.org/10.2514/6.2007-5051.
[26] D.E. Paxson, P.J. Litke, F.R. Schauer, R.P. Bradley, J.L. Hoke, Performance assessment of a large scale pulsejet-driven ejector system, in: Collection of Technical Papers - 44th AIAA Aerospace Sciences Meeting, 2006. https://doi.org/10.2514/6.2006-1021.
[27] D. Maqbool, C.P. Cadou, Acoustic analysis of valveless pulsejet engines, J Propuls Power 33 (2017). https://doi.org/10.2514/1.B36078.
[28] D. Maqbool, C.P. Cadou, Interaction Behavior of Pulsejet Engines, J Propuls Power (2023). https://doi.org/10.2514/1.b38855.
[29] M. Gieras, A. Trzeciak, A new approach to the phenomenon of pulsed combustion, Exp Therm Fluid Sci 144 (2023). https://doi.org/10.1016/j.expthermflusci.2023.110845.
[30] V. Anand, J. Jodele, E. Knight, E. Prisell, O. Lyrsell, E. Gutmark, Dependence of Pressure, Combustion and Frequency Characteristics on Valved Pulsejet Combustor Geometries, Flow Turbul Combust 100 (2018) 829–848. https://doi.org/10.1007/s10494-017-9875-1.
[31] J.B. Jodele, A.R. Zahn, V. Anand, E. Gutmark, Effects of geometrical variation on pressure, ionization, and thrust in a valved pulsejet, 2018 Joint Propulsion Conference (2018). https://doi.org/10.2514/6.2018-4574.
[32] V. Anand, J. Jodele, E. Prisell, O. Lyrsell, E. Gutmark, Dynamic features of internal and external flowfields of pulsejet engines, AIAA Journal 58 (2020) 4204–4211. https://doi.org/10.2514/1.J059685/ASSET/IMAGES/LARGE/FIGURE8.JPEG.
[33] V. Anand, J. Jodele, V. Shaw, A. Russell, E. Prisell, E. Gutmark, Visualization of Valved Pulsejet Combustors and Evidence of Compression Ignition, Flow Turbul Combust (2020) 1–22.
[34] V. Anand, J. Jodele, A. Zahn, A. Geller, E. Prisell, O. Lyrsell, E. Gutmark, Revisiting the Argus pulsejet engine of V-1 buzz bombs: An experimental investigation of the first mass-produced pressure gain combustion device, Exp Therm Fluid Sci 109 (2019) 109910. https://doi.org/10.1016/j.expthermflusci.2019.109910.

[35] P.L. Walter, Written By Guidance for the Filtering of Dynamic Force, Pressure, Acceleration (and Other) Signals Guidance for the Filtering of Dynamic Force, Pressure, Acceleration (and Other) Signals.
[36] Guide to Dynamic Force Sensors, www.pcb.com.
[37] A.E. Powell, Il doppio eterico : ealtri fenomeni, Macropost, 1996.
[38] M.M. Ghulam, E.J. Gutmark, Computational aeroacoustics for analyzing thermo-acoustic instabilities in afterburner ducts, in: 2018 Joint Propulsion Conference, American Institute of Aeronautics and Astronautics Inc, AIAA, 2018. https://doi.org/10.2514/6.2018-4607.
[39] R.L. May, A.K. Easton, Computational Techniques and Applications: CTAC 95, WORLD SCIENTIFIC, 1996. https://doi.org/doi:10.1142/3247.
[40] D.E. ROGERS, F.E. MARBLE, A Mechanism for High-Frequency Oscillation in Ramjet Combustors and Afterburners, Journal of Jet Propulsion 26 (1956). https://doi.org/10.2514/8.7049.
[41] P. Palies, D. Durox, T. Schuller, S. Candel, The combined dynamics of swirler and turbulent premixed swirling flames, Combust Flame 157 (2010). https://doi.org/10.1016/j.combustflame.2010.02.011.
[42] S. Candel, D. Durox, T. Schuller, J.F. Bourgouin, J.P. Moeck, Dynamics of swirling flames, Annu Rev Fluid Mech 46 (2014) 147–173. https://doi.org/10.1146/annurev-fluid-010313-141300.
[43] J. Lu, L. Zheng, Z. Wang, C. Peng, X. Chen, Thrust measurement method verification and analytical studies on a liquid-fueled pulse detonation engine, Chinese Journal of Aeronautics 27 (2014). https://doi.org/10.1016/j.cja.2014.04.001.
[44] E. Hopping, M. Murdy, N. Stepp, Design of a cost effective thrust stand for introducing thrust and impulse, 53rd AIAA Aerospace Sciences Meeting (2015). https://doi.org/10.2514/6.2015-0382.
[45] F.K. Lu, M. Awasthi, D.D. Joshi, Influence of unsteadiness on thrust measurements of pulse detonation engines, in: 48th AIAA Aerospace Sciences Meeting Including the New Horizons Forum and Aerospace Exposition, 2010. https://doi.org/10.2514/6.2010-1214.
[46] T. Geng, F. Zheng, A. V. Kuznetsov, W.L. Roberts, D.E. Paxson, Comparison between numerically simulated and experimentally measured flowfield quantities behind a pulsejet, Flow Turbul Combust 84 (2010) 653–667. https://doi.org/10.1007/s10494-010-9247-6.
[47] C.A. Blomquist, Experimental gas-fired pulse-combustion studies, 1982.
[48] C. Farbos de Luzan, L. Oren, A. Maddox, E. Gutmark, S.M. Khosla, Volume velocity in a canine larynx model using time-resolved tomographic particle image velocimetry, Exp Fluids 61 (2020). https://doi.org/10.1007/s00348-020-2896-x.

Chapter 2

Flame Dynamics in a Low-Emission Nozzle of the Multipoint Lean Direct Injection Combustion System

1. Introduction

The need to reduce pollutant emissions, particularly nitrogen oxides (NOx), from aircraft engines is critical due to environmental concerns and increasingly stringent government regulations. Several combustion technologies have been implemented to address this issue, such as Lean Premix Pre-Vaporize (LPP) and Rich-Burn, Quick-Mix, Lean-Burn (RQL) systems (see Fig.1) [1]. The objective of the LPP design is to attain complete evaporation and thorough mixing of the fuel and air with before entering the combustion chamber [2]. By operating the reaction zone at a lean fuel/air ration, the NO_x emissions are drastically reduced due to the low flame temperature and the elimination of the "hot spots" from the combustion zone. The LPP concept had been implemented in several aircraft engines such as the twin annular premixing swirler (TAPS) combustor used in the CFM LEAP, GEnx, and GE9x engines. The main drawbacks to the LPP system are the long time needed to fully vaporize and mix the fuel at low power conditions resulting in the occurrence of auto-ignition or flashback, and the susceptibility to combustion instability due to the lean burn condition. These challenges of the LPP system make it less practical for future modern engines requiring a strictly low emission. The RQL combustion is another type of technology that is being utilized currently in modern engines [3]. First, the "rich-burn" condition achieved with injecting excess of fuel beyond stoichiometry (ϕ = 1.8) in the primary zone, which enhances the stability of the combustion reaction by sustaining a high concentration of energetic hydrogen and hydrocarbon species. Due to the relative low temperature and oxygen

depletion (low population of oxygen containing intermediate species), the rich-burn condition reduces the NO_x production in the primary zone (see Fig.1b). Downstream of the primary zone, a jet air is injected to the flow stream to complete the combustion process and reduce the gas temperature in a manner that ensures a uniform and rapid mixing with the remaining hot products coming from the primary-zone. This is called the "quick-mix" process that must take place quickly, otherwise pockets of hot gas may survive long enough to produce appreciable amount of NO_x and damage the turbine blade. Historically, the research on the RQL combustor has mainly focused on optimizing the quick-mix section to establish the most rapid mixing mechanism. Finally, a dilution jet air (lean-burn process) is injected near the exit of the combustor to further reduce the exhaust temperature and therefore reduce the global equivalence ratio to the lean condition. Another major challenge of the RQL technology is the selection of the combustor liner material. For instance, the use of cooling air for the linear wall in the primary zone is precluded in order to avoid the near-stoichiometric condition and the associated production of NO_x. The RQL technology has been deployed commercially by Pratt & Whitney under the "Technology for Advanced Low NO_x" TALON combustors in PW4100, and PW6000 geared turbofan engines.

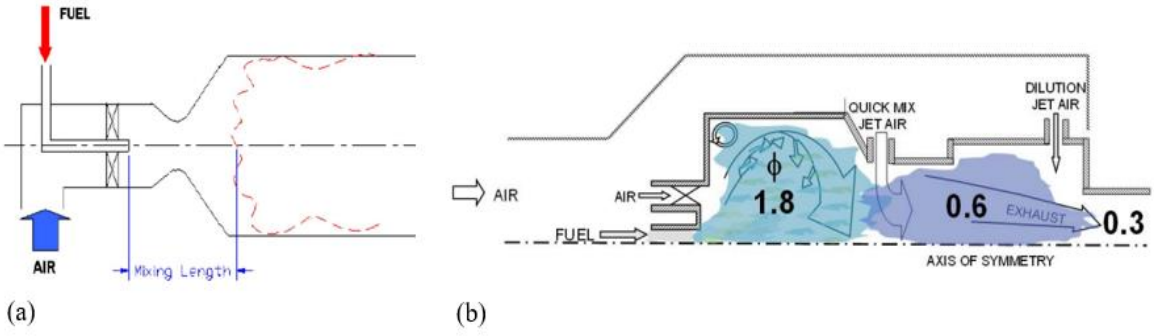

Figure 16. schamatic digrams of the (a) LPP [2]**, and (b) RQL combustion conceptes commonly utilized in the modren gas turbine engines** [3]**.**

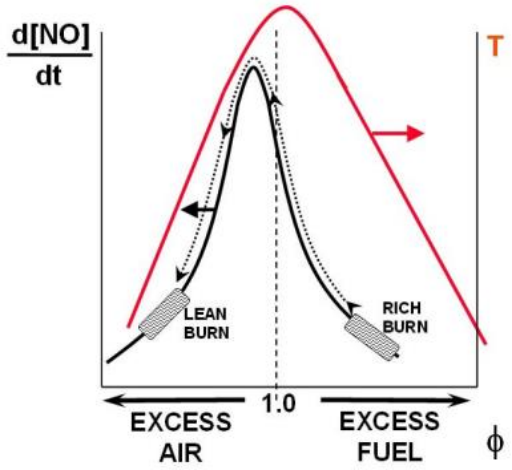

Figure 17. conceptual graph of the thermal NOx formation [3]**.**

A relatively new technology, known as the Multipoint Lean Direct Injection (MLDI) combustion system, developed by NASA, has demonstrated a significant reduction in NOx emission indices, achieving reductions of 50–70% compared to the traditional burners mentioned above [4,5]. Key strategies for mitigating thermal NOx formation include avoiding high-temperature combustion (or hot spots) by operating at either lean or rich equivalence ratios (see Fig.2), as well as minimizing the residence time of combustion reactions through rapid fuel/air mixing via higher injection velocities and reduced combustion chamber size. The MLDI system operates with lean fuel/air ratios and employs an array of multiple small-sized swirl nozzles instead of the larger single nozzles commonly used in conventional gas turbine engines as demonstrated in Fig.3. Reducing nozzle diameter has a linear relationship with the NOx emission index (EINOx) and decreases the volume of the recirculation zone, which is believed to be the primary mechanism controlling thermal NOx formation in typical combustors [6]. Figure 4 shows the effect of increasing the number of nozzle array while reducing its size on the NOx emission. The 9-point case had a nozzle diameter of approximate 25.4 mm, while the 25-point and 36-point configurations had a nozzle diameter of about 60% and 35% of the 9-point case, respectively. There is a linear relationship between the emission index of NO_x (EINO_x) and the nozzle size. The

EINO_x at the fuel to air ratio (FAR) of 0.035 decreased significantly, where the 25-point array produced 60% - 65% EINO_x and the 36-array produced 35% - 37% EINO_x of the 9-point array (note: the 49-array point did not follow the trend because it had a few blockages inside the fuel lines causing non-uniform fuel/air mixing). Another advantage of the MLDI design is its ability to reduce combustor length by generating a compact flame zone. Additionally, the MLDI system helps eliminate temperature streaks that arise when fewer injectors are used, due to the direct injection of fuel and air into the combustion chamber. This leads to short residence times, rapid and uniform mixing, and a reduction in hot spot intensity while maintaining relatively low average flame temperatures. Furthermore, direct fuel injection into the flame zone lowers the risk of flashback. However, since the MLDI system operates with lean fuel/air ratios (in the range of 0.9 to 0.5 equivalence ratio), it is prone to combustion instability (thermoacoustic phenomena). Despite these challenges, the MLDI concept remains NASA's most promising candidate for ultra-high-pressure, low-emission engine cycles. Additional studies and analyses are needed to further understand the operational mechanisms of the MLDI combustion system [7].

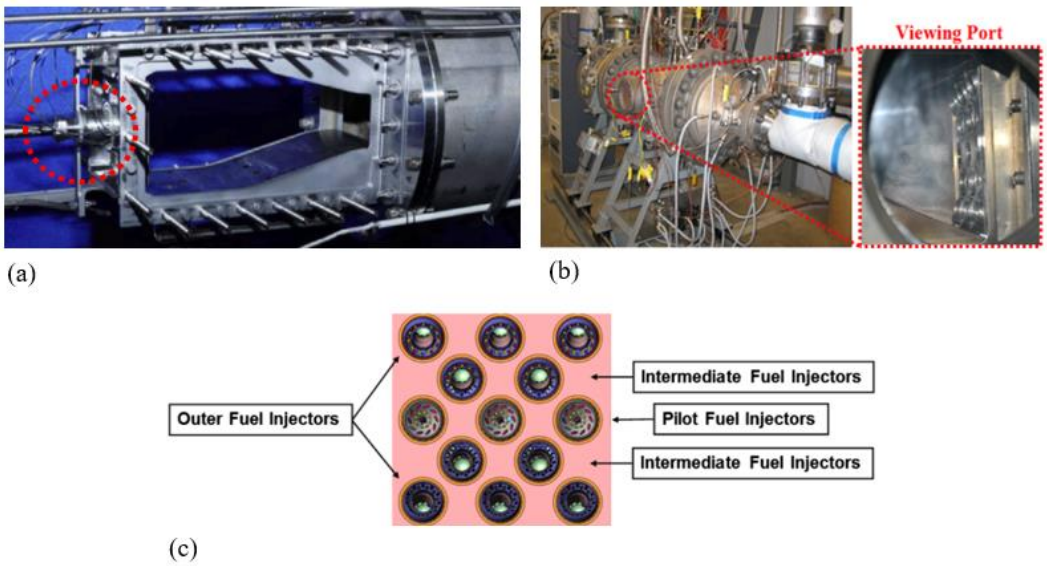

Figure 18. (a) A single cup RQL combustion [8]**, (b) MLDI combution inside a high pressure rig, and (c) top viw of the MLDI matrix consisting of multipoint injection swirling nozzles** [9]**.**

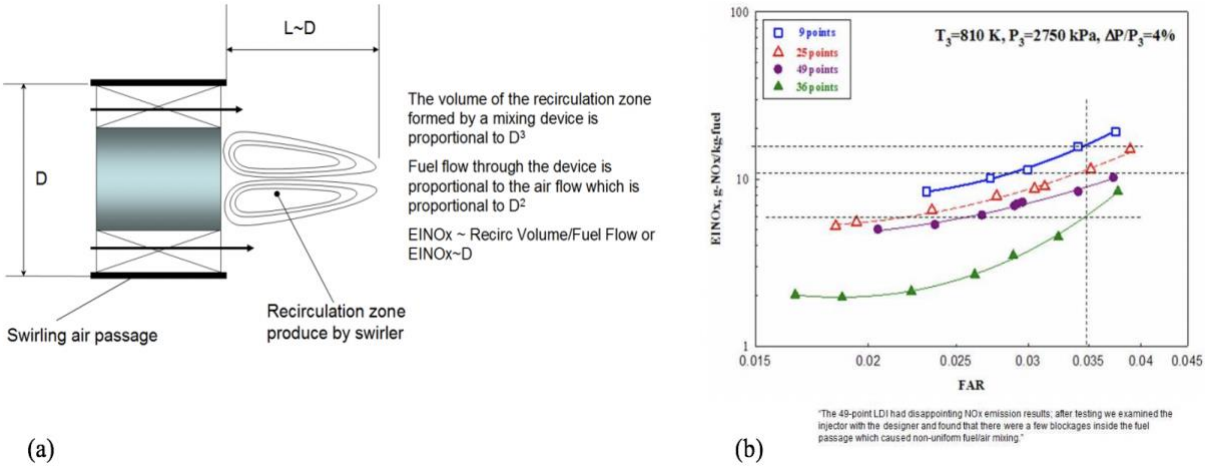

Figure 19. (a) Injector size parameters, and (b) NOx emission reduces linearly with the nozzle diameter [4]**.**

The MLDI system consists of two primary fuel injector designs: low-emission nozzles and pilot nozzles. Both designs produce swirl-stabilized flames, which are believed to offer superior flame stabilization and combustion efficiency compared to other techniques [10]. The pilot nozzle, a pressure atomizer, has a high swirl number, providing a thick recirculation zone for robust flame stabilization and a compact reaction zone. In contrast, the low-emission nozzle, an airblast atomizer, has a relatively lower swirl number and a thinner recirculation zone. The intensity of the swirling flow is characterized by the swirl number (SN) that is defined as the ratio between the tangential momentum flux and axial momentum flux as follows:

$$SN = \frac{\int_0^R u_z\, u_m r^2\, dr}{R \int_0^R {u_z}^2\, r\, dr} \qquad (1)$$

Where R is the radius of the injector, u_z is the axial velocity component, and u_m is the azimuthal velocity component. Most of the practical swirling injectors operate under the conditions of high swirl number that is around 0.6 or higher. A typical swirling flow features a vortex breakdown (VB) bubble that is manifested as a stagnation point followed by a reverse flow. The VB bubble comprises of two inner recirculation zones (IRZ), which are formed due to the adverse pressure

gradient caused by the sudden expansion of incoming swirling flow [11]. Therefore, the formation of the IRZ depends on the decay of swirl axial velocity. Moreover, the IRZ contains of the hot combustion products and aids the process of air/fuel mixing by entraining cold fresh gases located within inner jet shear layer (ISL). Additional recirculation regions are formed in the confined environment and are called the outer recirculation zones (ORZ) as illustrated in Fig. 5a. Umeh et al. explained that the shape and size of recirculation zones in swirling flow has significant effects on the flame structure since the flame is anchored by along the ISL [12]. Furthermore, the size of the combustor can be a source of fluctuations by altering swirling jet magnitude and IRZ dynamic features [13]. In a highly swirling flow, another aerodynamic phenomenon appears that is called the precessing vortex core (PVC), which rotates around the IRZ in a non-symmetric pattern and moving along the ISL and outer shear layer (OSL) as can be seen in Fig. 5b [14,15]. The PVC increases the thickness of jet shear layers and therefore changes the shape of the IRZ leading to flame surface perturbations leading to combustion instability. However, another group of researchers showed that when the shear layer thickness increased by PVC the flame sensitivity to acoustic perturbations decreased [16–19].They proposed a method of suppressing thermoacoustics oscillation by utilizing PVC in the flow field by increasing the swirl number, as the velocity-coupled flame interaction would be suppressed if there was weak shear layer response to acoustic excitation. The PVC is generally characterized using proper orthogonal decomposition (POD) analysis as a pair of asymmetric modes (single-helix), or symmetric modes (double-helix) [20]. Some studies showed that both single-helical and double-helical modes can coexist in swirling jets and identified the latter structure to be a harmonic mode of the first one [21,22]. However, it has been shown in a recent work that the single-helical and double-helical structures are independent global modes, and they can simultaneously occur in swirling jets [23].

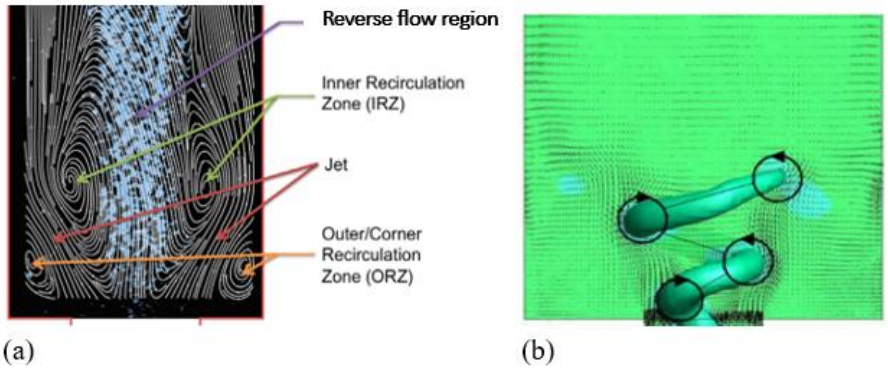

Figure 20. (a) A typical swilring flow dyanmics [24]**, (b) Illustration of the PVC in a swilring flow** [25].

According to Hicks et al., decreasing the swirl number reduces NOx emissions but also increases flame length and reduces combustion stability in the MLDI system [26]. Most previous studies related to this combustor design have focused on NOx emissions, taking into account factors such as nozzle spacing, arrangement, and operating conditions. For instance, Dolan et al. examined the effects of spacing between two adjacent LDI nozzles on flow patterns under both non-reacting and reacting conditions, and its impact on NOx emissions [27–30]. Villalva et al. analyzed reaction zone characteristics with varying fuel distribution among 13 adjacent MLDI nozzles under elevated pressure conditions [9]. Other studies on a single-element pilot nozzle of the MLDI system explored vortex breakdown dynamics in both confined and unconfined non-reacting flow conditions [31,32].

The equivalence ratio significantly influences the structure and stability of swirl-stabilized flames. Varying the equivalence ratio alters the macrostructure of the flame and its stability [33,34]. For example, reducing the equivalence ratio increases the size of the inner recirculation zone, which affects flame stabilization, flame height, heat release, and temperature distribution in the combustion chamber, ultimately impacting NOx emissions. Additionally, different equivalence ratios produce various flame structures, such as double conical, corner-stabilized, and swirl-stabilized flames, each with specific combustion characteristics [35]. Varying the equivalence ratio

also changes the size of the inner recirculation zone, causing transitions between "V" and "M" flame configurations [36]. Hao et al. found that as the equivalence ratio increases, the average OH* concentration and flame surface density rise, increasing the flame brush thickness [37].

There is currently limited published research on the flame dynamics of a single-element low-emission nozzle used in the MLDI combustion system. Therefore, the present study aims to analyze the flame behavior of the single-element low-emission nozzle design under various equivalence ratios, from near stoichiometry to the lean blowout limit. A thorough understanding of flame behavior in this design will aid in refining current systems, ultimately enhancing the efficiency of aircraft gas turbine engines. This study investigates the effects of equivalence ratio on a single-element low-emission nozzle to gain fundamental insights into flame dynamics. High-speed OH* chemiluminescence measurements, along with a microphone to monitor sound emissions outside the combustion chamber, are used under different equivalence ratio conditions. Furthermore, mode decomposition analysis is conducted to examine different flame shapes associated with varying equivalence ratios, helping to identify the flame's coherent modes. Phase-averaged results between microphone data and OH* flame intensity provide valuable insights into the coupling mechanisms that occur as flame structure changes with equivalence ratio.

2. Experimental Setup

The swirled-stabilized combustion rig consists of a steel air inlet plenum with a diameter of 174.6 mm, equipped with flow straightening screens (see Fig. 6). This section is followed by a mid-section of the same diameter, featuring a mounting flange perpendicular to the rig's axial axis. The test section is positioned at the exit of a rectangular plenum (203.2 × 134.62 × 101.6 mm^3), where a pressure transducer and low emission swirler nozzle are installed. The low-emission nozzle, which is an air-blast fuel injector, has a swirl number between 0.5 and 0.7. It is designed to produce lower swirling intensity compared to the pressure-atomizer pilot nozzle. A Master-Touch (series 8000 MP/NH) thermal mass flow meter is used to measure the mass flow rate. The meter's accuracy, including linearity, is ±1% of reading plus 0.5% of the full scale, with a repeatability of ±0.2% of the full scale. Propane (C_3H_8) is used as the fuel for combustion, while air is preheated up to 500 K using a 36-kW electric heater. The combustor is a rectangular test section made of fused silica quartz glass, allowing for optical measurements of the flame within the combustion chamber. The system is designed to accommodate different combustion confinements. The air flow rate is adjusted according to various operating conditions to maintain a 2% pressure drop across the swirler nozzle. For the equivalence ratio study, where the inlet air temperature is preheated to 500K, the air flow rate is maintained at 4.3 g/s to achieve the required 2% pressure drop. The corresponding Reynolds number (*Re*) is calculated as follows:

$$Re = \frac{\rho * v * D}{\mu} \qquad (2)$$

where the air density (ρ) is 0.706 kg/m^3, and the dynamic viscosity (μ) is $3.178 \times 10^{-5} kg/m.s$ at 500K. The combined diameter of the nozzle opening area is approximately D = 0.009624 m. Hence, the corresponding air velocity ($v = \frac{air\ flow\ rate}{\rho *\ A_{cross\ section}}$) is v = 83723.749 m/s. Therefore, the

approximate Reynolds number (*Re*) of the incoming air flow through the low-emission nozzle is *Re* = 21306237. The operating test conditions for all cases included on the equivalence ratio effects campaign are demonstrated in Table 1. Three inlet temperatures are included to investigate the effects of the temperature on the flame structure, namely 300K, 400K, and 500K. Furthermore, three different confinement ratios are analyzed which are: 5.6, 6.9, and 9.6 (see Table 2). The confinement ratio (CR) is defined as the ratio of the cross-sectional area of the test section to the cross-sectional area of the nozzle, as shown below:

$$CR = \frac{A_{test\ section}}{A_{nozzle}} \qquad (3)$$

In order to examine the exit boundary effects a rectangular plate with a one-inch diameter hole is placed on top of the combustion chamber as illustrated in Fig.7. Only the 5.6 and 6.9 confinement ratios are studied with the exit plate boundary, as igniting the flame from the exit hole using the flame torch at the 9.6 confinement ratio was not achievable. A free-field Bruel & Kjaer 1/4" microphone (type 4939), with a sensitivity of 4.25 mV/Pa and an uncertainty of ±0.2 dB at a 95% confidence level, is used to measure sound levels. The microphone is placed 20 cm from the combustor test section. To investigate flame dynamics, including flame structure and reaction zone intensity, an OH* chemiluminescence imaging technique is employed. During combustion, the high flame temperatures excite certain molecular species, causing them to emit photons at specific wavelengths as they return to their ground state.

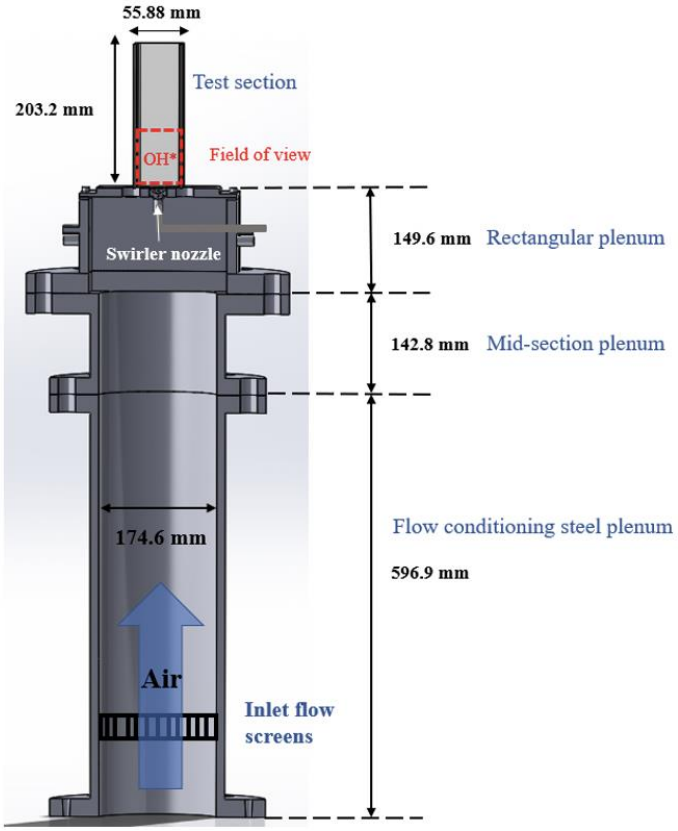

Figure 21. Cross-sectional view of the atmospheric combustion facility.

Table 5. Experimental test conditions for studying the equivalence ratio effects.

Air Temperature (K)	Confinement Ratio	Air Flow rate (g/s)	Fuel Flow rate (g/s)	Global Equivalence Ratio (ϕ)
500	5.6	4.3	0.26	0.947
		4.3	0.24	0.875
		4.3	0.22	0.802
		4.3	0.20	0.729
		4.3	0.19	0.692

Table 6. The different parameters included in the study.

Air Temperature (K)	Confinement Ratio	Exit Boundary
300	5.6	Without exit plate
400	6.9	With exit plate
500	9.6	-------

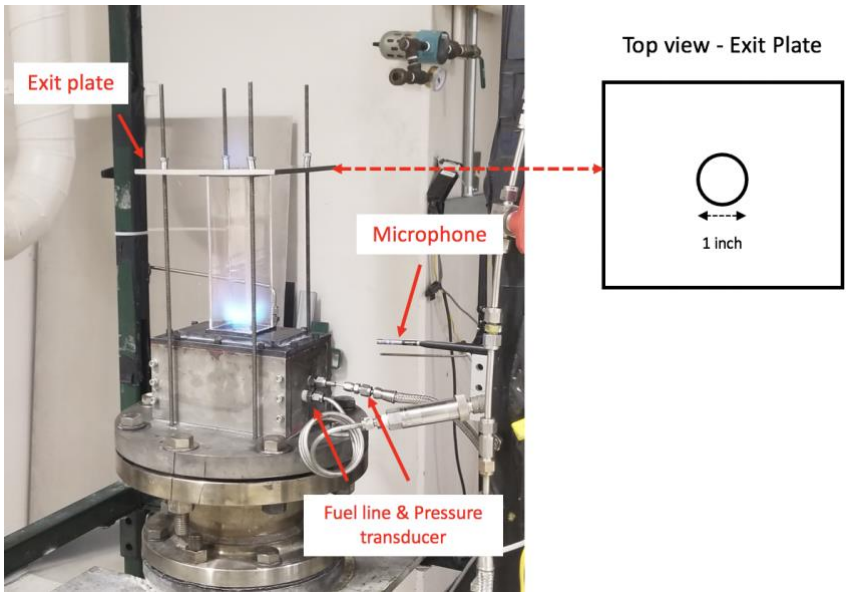

Figure 22. The exit plate with 1 inch (the same size of the nozzle diameter) circular shape hole is installed at the top of the test section.

By equipping the camera with an optical filter at a wavelength of 310 nm, OH* radicals from the flame can be optically measured. However, careful interpretation is required when presenting the OH* imaging results. For instance, the OH* intensity:

$$I = C * HR \qquad (4)$$

where I is the local chemiluminescence intensity, HR is the local heat release rate, and C is a constant coefficient, cannot be directly correlated with the heat release rate because the temperature-dependent component of the constant coefficient (C) is unknown. However, higher OH* intensity means higher flame temperature, with the temperature value is absent. A high-speed Phantom v16 camera is used to record 10,000 images during combustion operation. The camera is connected to a LaVision HS IRO X intensifier, equipped with a 310 nm wavelength filter lens and a focusing lens with a 100 mm focal length (see Fig. 8). Due to the weak signals from the OH* radicals, the intensifier is employed to amplify and increase the sensitivity of the signals captured in the recorded images. Both the OH* imaging and microphone sound measurements are captured at a 25 kHz acquisition rate using LabView software, which allows for

the direct visualization of temporal flame behavior, such as combustion dynamics occurring at frequencies of several hundred hertz.

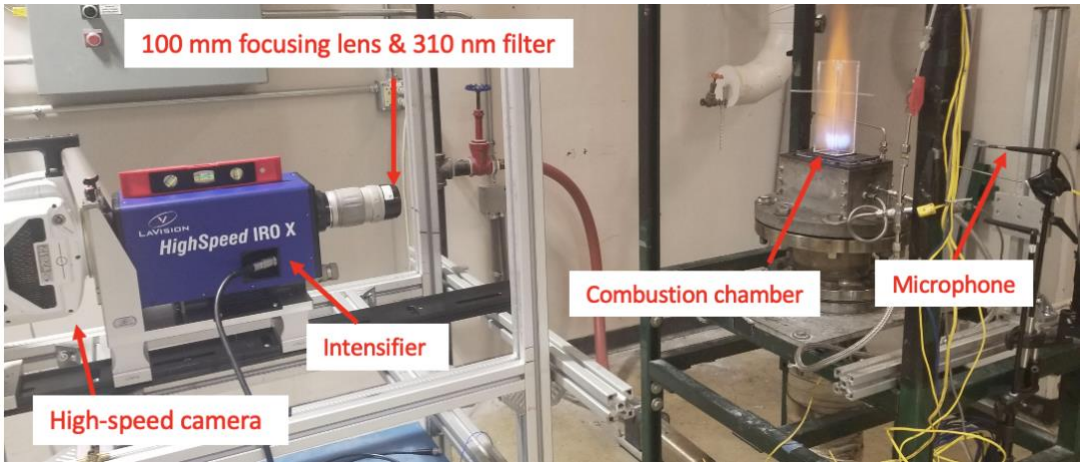

Figure 23. The OH* chemiluminescence and microphone experimental set up.

3. Results and Discussion

3.1. Equivalence Ratio Effects

3.1.1. Identified flame structures

The instantaneous flame images provide an initial observation of overall flame evolution as the equivalence ratio changes (see the top row in Fig. 9). A noticeable shift in the flame's anchoring position and structure is evident as the fuel is reduced (from left to right). At higher equivalence ratios, the flame is anchored near the nozzle exit, while at lower equivalence ratios, the anchoring point moves downstream, eventually forming a distributed flame at the lean blowout (LBO) limit (the anchoring points are indicated by the white dashed line). However, the raw flame images are line-of-sight images, meaning the measured light intensities are integrated across the entire field, including signal contributions from both in front of and behind the focal plane of the ICCD lens. Therefore, the raw OH* images do not provide precise information about the flame macrostructure in the middle section of the combustor, where the camera is focused. To address this, image deconvolution is required to obtain spatially resolved information [38–40]. The 3-point Abel deconvolution method is applied to the OH* images to reconstruct the flame's structure [41–43]. To eliminate the noise signal, a Gaussian filter with sigma = 6 is adopted [44]. As seen in the bottom row of Fig. 9, the flame transitions from a V-shaped configuration, anchored at the nozzle exit at higher equivalence ratios, to M-shaped and distributed-lifted flames as the equivalence ratio decreases, approaching the LBO limit. The advantages of using the Abel deconvolution method are particularly evident in the transient M-V flame (case C, $\phi = 0.802$) and the M-flame (case D, $\phi = 0.729$), where the reconstructed flame images clearly reveal the flame's macrostructure. In contrast, the line-of-sight images appear to show a rectangular flame. As described in the introduction, the flame transitions from a V-shaped to M-shaped and lifted-distributed

configurations are attributed to changes in the inner recirculation zone, which increases in size and alters its shape and location as the equivalence ratio decreases. The change in the swirling flow field with decreasing equivalence ratio occurs because, as the fuel is reduced, the temperature decreases, leading to lower air density and reduced axial velocity. Consequently, the inner recirculation zones resulting from vortex breakdown become larger, altering the flame's anchoring position and structure. The changes in recirculation zone structure and temperature distribution relative to the equivalence ratio are shown in Fig. 10 from the work of Medhat et al.[33]. The OH* flame intensity along the centerline, shown in Fig. 11, is linearly correlated with the equivalence ratio. As the equivalence ratio decreases, less fuel is burned, resulting in fewer OH* radicals emitted from the flame. Additionally, the flame's OH* peak location, marked by the black dashed line, shifts slightly downstream at lower equivalence ratios, indicating a lift-off behavior. Figure 11 further illustrates the effect of the equivalence ratio on flame size (see the red dashed line). As the equivalence ratio decreases, the size of the inner recirculation zone increases, resulting in a larger flame. These results indicate that, at higher equivalence ratios, the OH* peak intensity in the V-flame is concentrated in the center of the reaction zone, while in the M-flame ($\phi = 0.729$) and lifted-distributed flames ($\phi = 0.692$), the OH* intensity becomes more evenly distributed along the sides of the combustion chamber and streamwise at lower equivalence ratios. The V-flame, with its concentrated reaction zone (hot spot), is disadvantageous for thermal NOx formation, while the M-flame and lifted-distributed flames can produce lower thermal NOx due to their distributed nature of reaction zones. Thus, analyzing the flame structure provides valuable insight into the thermal distribution, which ultimately affects NOx emissions for different flame types occurring at varying equivalence ratios.

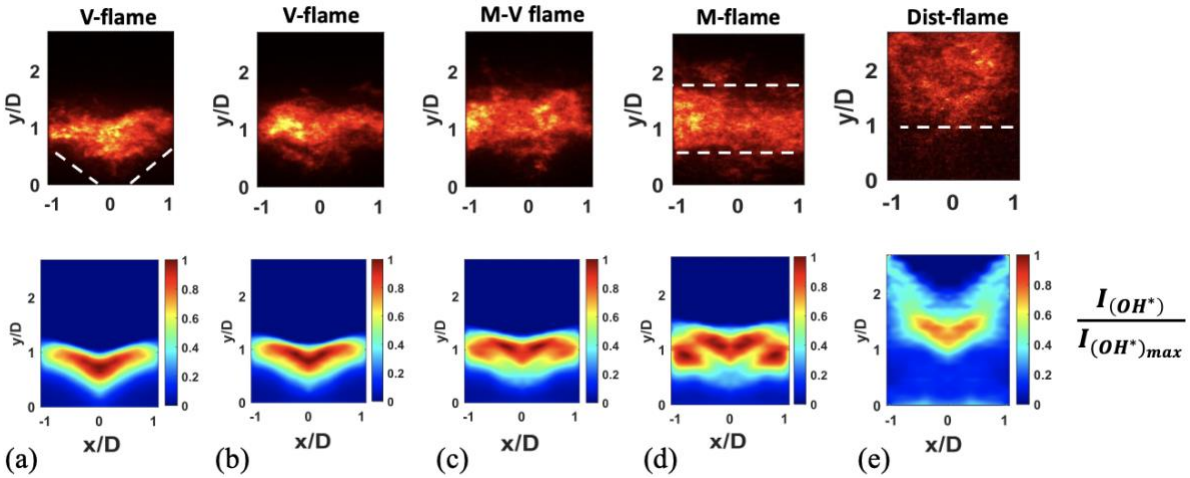

Figure 24. Top row: instantaneous flame images. Bottom row: Averaged Abel-deconvoluted flame images normalized by the maximum OH*intensity values of (a) ϕ = 0.947, (b) ϕ = 0.875, (c) ϕ = 0.802, (d) ϕ = 0.729, (e) ϕ = 0.692. The equivalence ratio decreases from left to right.

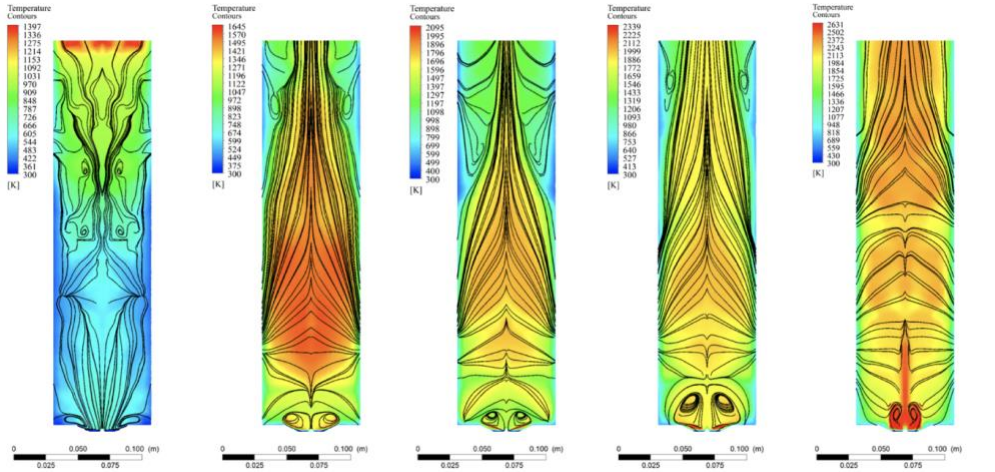

Figure 25. the change in the flow field and temperature distribution with respect to the equivalence ratio of a swirled-stabilized flame, the equivalence ratio increases from left to right [33]**.**

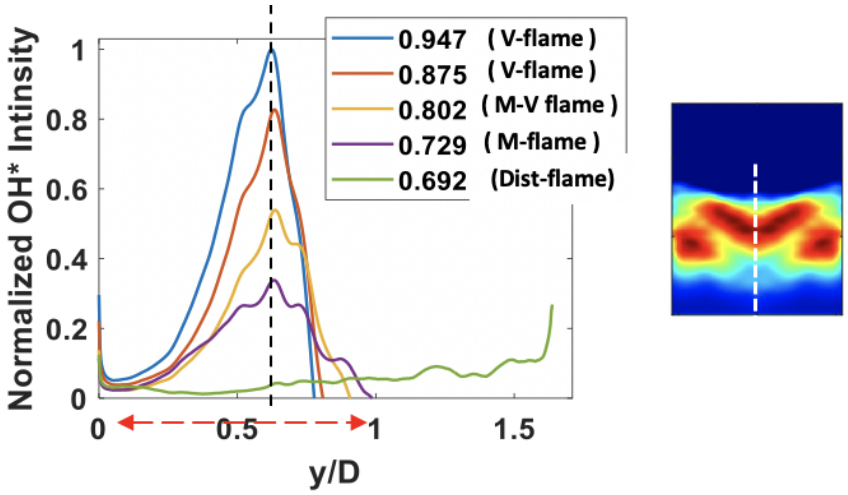

Figure 26. The OH* flame intensity along the center line. The figure on the left shows the location of the center line, and the legends indicates the equivalence ratio cases.

3.1.2. Coherent structure in the flames

The spectral proper orthogonal decomposition (SPOD) method is employed to further elucidate the dynamic coherent structures of the flame at different equivalence ratios [45–50]. Figure 12 presents the energy spectra of the first three modes in the top row, along with the corresponding spatial structures of the dominant modes and their frequencies in the bottom row for the identified flame types at varying equivalence ratios. From the energy mode spectrum, it can be observed that the dominant mode of the V-shaped flame occurs around 800 Hz, whereas for the M-shaped flame, it occurs close to 400 Hz. This frequency difference is directly related to the temperature: higher equivalence ratios correspond to higher mean temperatures, and consequently, higher oscillation frequencies, while lower equivalence ratios lead to lower mean temperatures and lower oscillation frequencies. Notably, the dominant mode in the V-shaped flame is characterized by axial fluctuations, while in the transition flame (M-V flame) and the M-shaped flame, the dominant modes are associated with radial fluctuations. The lifted-distributed flame, observed near the lean blowout (LBO) limit, does not exhibit a coherent dominant mode. However, for illustrative purposes, the 30 Hz mode, which has the highest energy content, is displayed to demonstrate the

non-coherent turbulence mode of the flame at the LBO. Furthermore, the mode energy spectrum reveals that as the equivalence ratio decreases, the peak mode dissipates, indicating that the flame loses its large-scale coherent structure and transitions into more random turbulence. This shift occurs as the flame transitions from a V-shaped structure to a lifted-distributed flame near the LBO. These results demonstrate that the V-shaped flame, at higher equivalence ratios, possesses higher energetic content with axial oscillations. In contrast, the M-shaped flame, oscillating radially at lower equivalence ratios, exhibits less energetic content. Examining the SPOD spectrum of the V-flame cases at the first two equivalence ratios, $\phi = 0.947$ and $\phi = 0.875$, shown in Fig. 13, one can observe a radial fluctuation mode around 400 Hz coexisting with an axial fluctuation mode, with the latter being dominant. These results suggest a competition between axial and radial fluctuation modes influenced by changes in flame structure as the equivalence ratio varies. Palies et al. explained that the axial fluctuation mode is associated with vortex roll-up of the flame, while the radial fluctuations are linked to fluctuations in the flame angle [51]. The following subsection will provide a more detailed discussion on the correlation between the flame's dynamic structure and acoustic measurements.

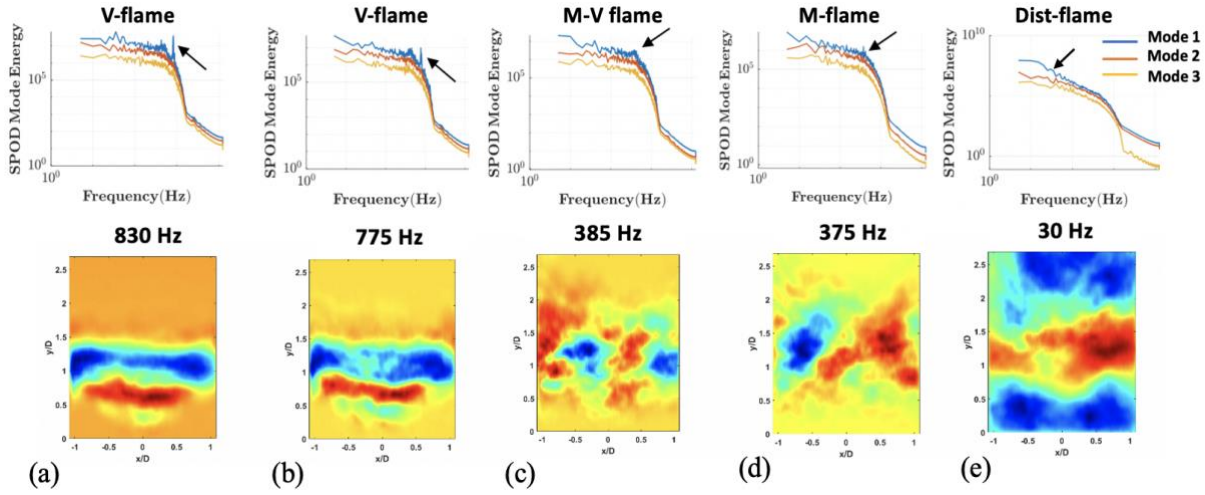

Figure 12. SPOD modes with their frequency maps of (a) $\phi = 0.947$, (b) $\phi = 0.875$, (c) $\phi = 0.802$, (d) $\phi = 0.729$, (e) $\phi = 0.692$.

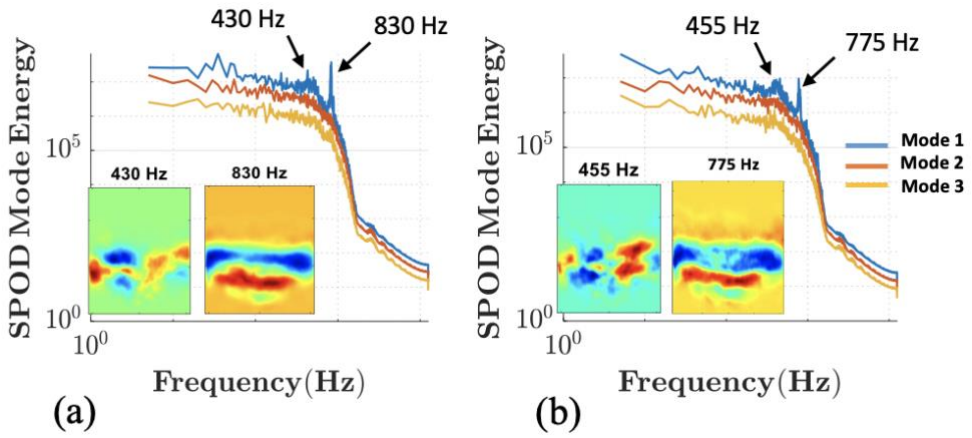

Figure 13. The co-existence of the axial and radial fluctuation modes during the V-flame conditions in (a) ϕ = 0.947, and (b) ϕ = 0.875.

3.1.3. Interaction between flame and acoustics

The Fast Fourier Transform (FFT) was applied to the acoustic data measured by the microphone positioned outside the combustion chamber, and the resulting frequencies are shown in Fig. 14. Notably, the dominant frequency values (f = 822.65 Hz, and f = 790.158 Hz) from the microphone data, recorded during the V-flame conditions occurring at higher equivalence ratios (ϕ = 0.947, and ϕ = 0.875), closely matches the dominant frequency values of 830 Hz and 775 Hz identified through the SPOD mode analysis. This indicates a coupling mechanism between the flame and the acoustic field. As the equivalence ratio decreases, however, a significant deviation between the SPOD and microphone dominant mode frequency values emerges. Additionally, lower-frequency modes appear in the microphone measurements at lower equivalence ratios. This suggests that, as the flame loses its coherent structure—transitioning into M-flames and lifted-distributed flames near the LBO limit—the acoustic noise measured outside the combustion chamber becomes dominated by turbulence noise. In contrast, under V-flame conditions at higher equivalence ratios, the coupling between the flame and the acoustic field is the primary source of combustion noise. To further elaborate on the relationship between flame dynamics and acoustic noise, the sound pressure level (SPL) obtained from the microphone measurements for each flame structure is

displayed in Fig. 15. The data clearly demonstrate a linear correlation between combustion noise and the equivalence ratio. As the equivalence ratio increases, the SPL also increases. This is due to the faster propagation speed of sound in higher temperature environments associated with higher equivalence ratios, which affects the sound intensity measured by the microphone. Specifically, the V-flame produces the highest sound intensity, approximately 170 dB, whereas the M-flame and lifted-distributed flames generate significantly lower sound intensities, in the range of 157–145 dB. To understand the coupling between flame dynamics and acoustic pressure, phase-averaged results of the flame OH* intensity and microphone pressure are presented in Fig. 16. The phase-averaging method employed follows the framework established by our group in previous research [52]. During the V-flame phase, the flame OH* intensity and microphone pressure are almost in-phase, highlighting a strong correlation between the flame structure and acoustic pressure. As the flame transitions into the M-flame structure, the OH* intensity and microphone pressure become out-of-phase, indicating decoupling of the flame and acoustic field. Interestingly, during the lifted-distributed flame phase near the LBO condition, the OH* intensity and pressure become in-phase once again, although the overall sound intensity remains lower due to the flame's lack of coherent structure. These findings reveal that the V-flame, which occurs at higher equivalence ratios and is characterized by axial fluctuations, exhibits strong flame-acoustic coupling, resulting in high sound intensity. Conversely, during the M-flame phase at lower equivalence ratios, which is dominated by radial fluctuations, the flame and acoustic fields are decoupled, leading to reduced sound intensity. At the LBO condition, the flame and acoustic fields are back in-phase; however, due to the incoherent flame structure and increased turbulence, the sound intensity remains relatively low.

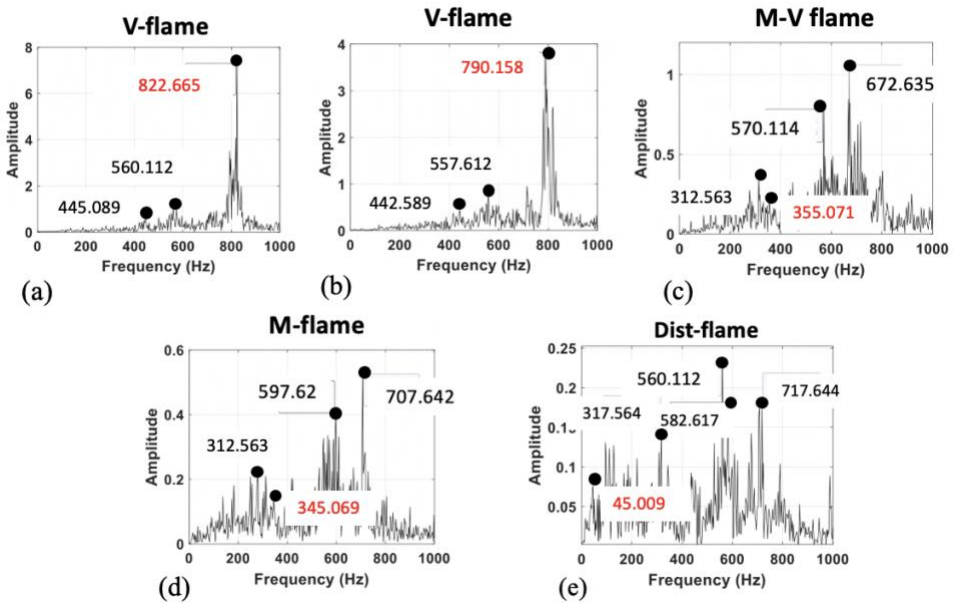

Figure 14. FFT results of the acoustic measurements of (a) ϕ = 0.947, (b) ϕ = 0.875, (c) ϕ = 0.802, (d) ϕ = 0.729, (e) ϕ = 0.692.

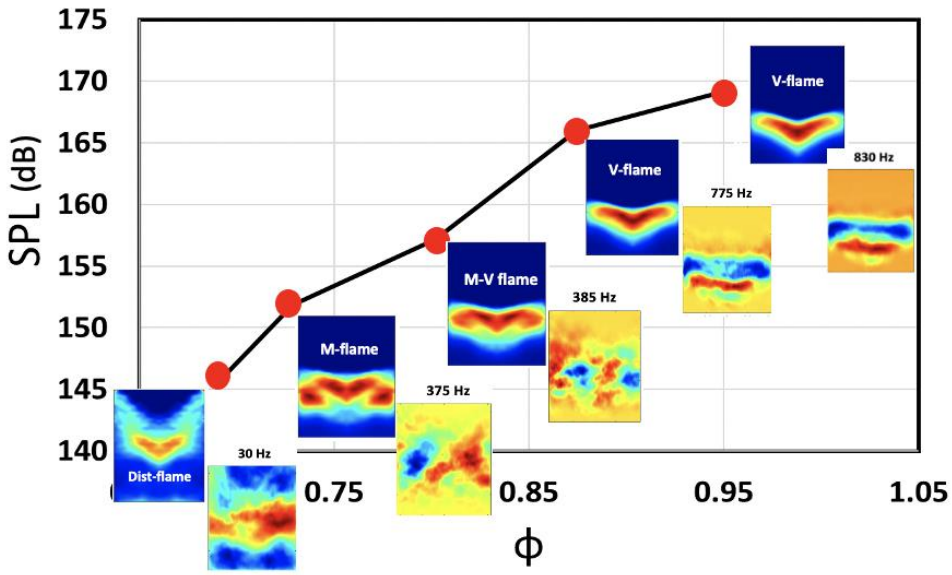

Figure 15. Sound pressure level (SPL) of the microphone measurements for the different flame shapes and modes associated with each equivalence ratio.

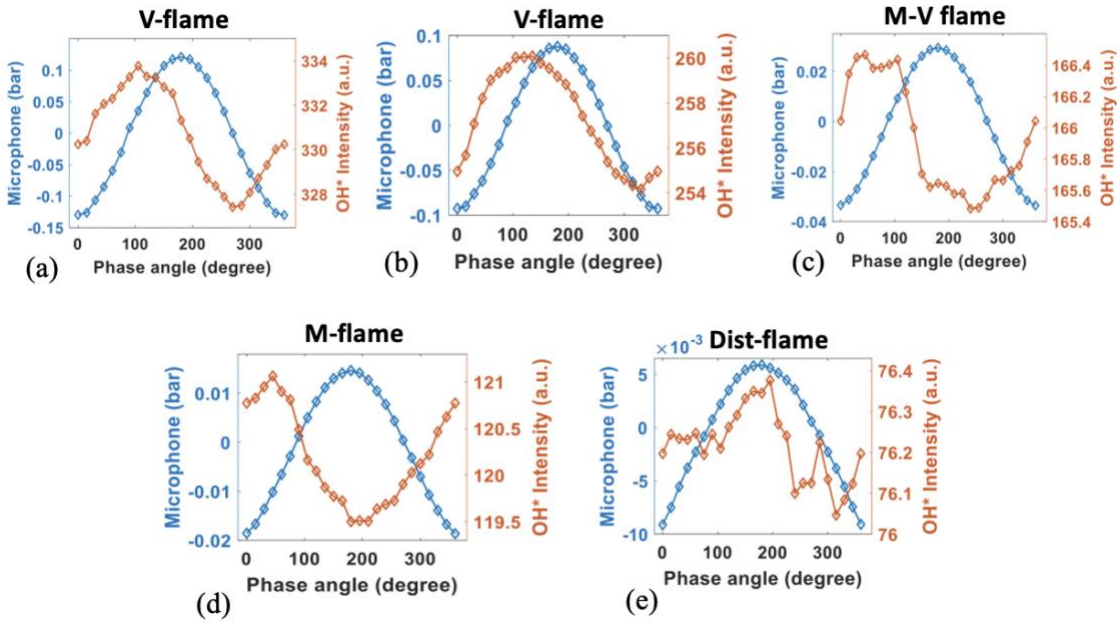

Figure 16. The phase-averaged results of the OH* flame intensity and microphone pressure of (a) ϕ = 0.947, (b) ϕ = 0.875, (c) ϕ = 0.802, (d) ϕ = 0.729, (e) ϕ = 0.692.

3.2. Inlet Temperature and Confinement Ratio Effects

Several studies have shown that increasing the preheated air temperature leads to a higher peak temperature. Preheating increases the maximum temperature in swirl-stabilized flames by 40 to 60 K for every 100 K increase in inlet air temperature. Additionally, increasing the inlet air temperature results in a shorter flame length, which promotes flame stabilization near the burner rim, as observed in Fig. 17 [53]. This occurs because higher preheat levels cause flames to become shorter and thinner, with increased turbulence kinetic energy, potentially leading to thermal instabilities and flashback risks. Moreover, raising the inlet air temperature expands the lean flammability limit, allowing operation closer to the LBO limit as demonstrated in Fig.18 [54]. However, higher preheated air temperatures are associated with increased emission indices of NOx, CO2, and O2. Three different inlet temperature cases—300 K, 400 K, and 500 K—are included to provide a comprehensive understanding of the inlet temperature's effect on the MLDI low-emission nozzle flame dynamics.

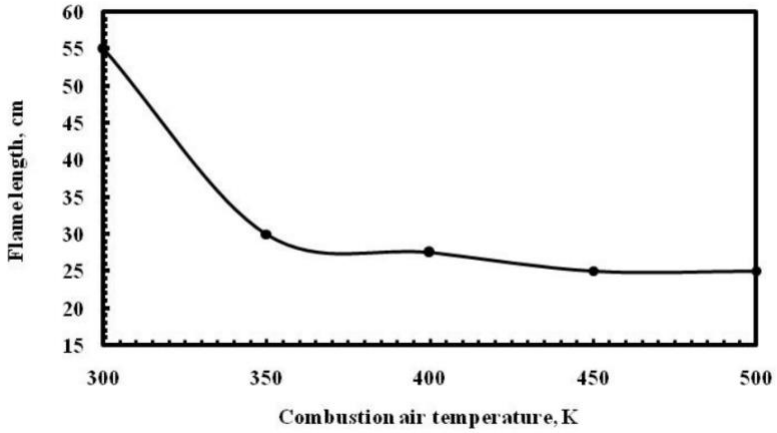

Figure 17. The flame length decreases as the inlet temperature increases [53]**.**

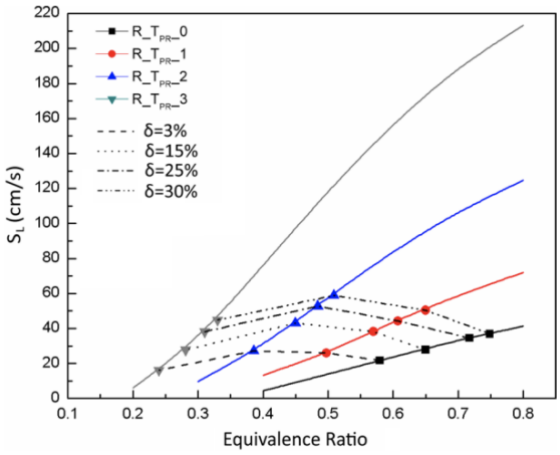

Figure 18. Effect of the inlet temperature on the flammability limit represented by the laminar flame speed [54].

The size of the combustor significantly impacts the dynamics of swirling flows. Some researchers have observed that velocity fluctuations and turbulence kinetic energy (TKE) increase substantially—by approximately 50%—in confined flows [55]. In non-reacting swirling flows, as shown in Fig. 19, the strength of the axial velocity of the swirling jet decreases as the combustor size increases, leading to greater radial jet dispersion due to the enlargement of the reverse flow region and recirculation vortices [32]. Under reacting conditions, confinement homogenizes temperature due to increased radial spreading and turbulence, resulting in a more uniform flame structure [13]. The current study examines the same confinement ratio (CR) cases depicted in Fig.19, specifically 9.6, 6.9, and 5.6 ratios. This approach ensures a thorough investigation of the effects of combustor size by including large, medium, and small combustor sizes.

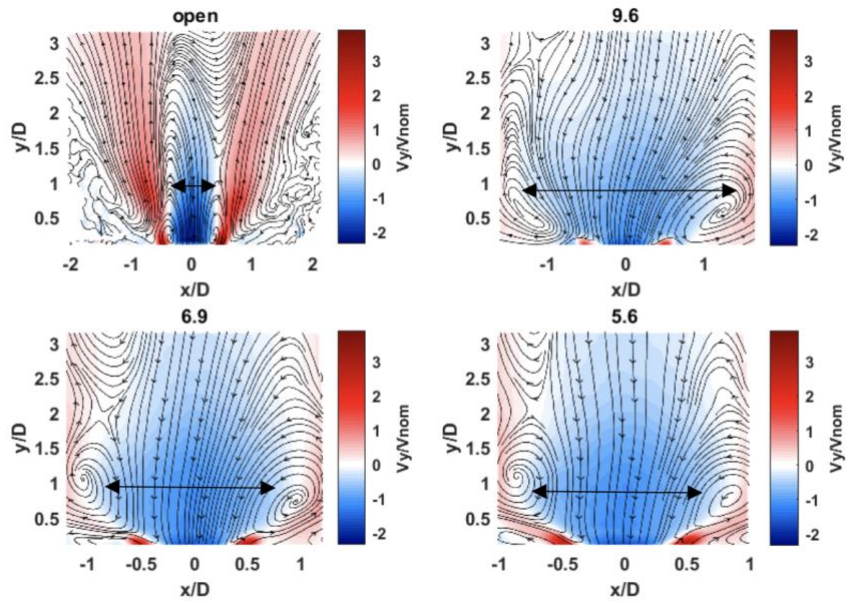

Figure 19. The axial velocity profile superimposed with streamlines showing the effects of confinement size on the swirling flow dynamics [32]**.**

To study the impacts of inlet temperature and confinement ratio, the averaged Abel-deconvoluted OH* flame results for a single, near-stoichiometric equivalence ratio are presented in Fig. 20. The flame structure and anchoring point change significantly with variations in inlet temperature and confinement ratios. For example, with a confinement ratio of 5.6, the flame transitions from an M-flame at 300K to a V-flame at 500K. Additionally, the flame base location (anchoring point) gradually shifts downstream from 0.5D at 300K to near 0D at 500K. As with the previously discussed equivalence ratio effect, increasing the inlet temperature reduces air density, leading to an increase in swirling axial velocity, which causes the inner recirculation zones to shrink and move downstream. Consequently, the flame structure, which depends on the size and location of the inner recirculation zones, changes according to factors affecting the swirling flow dynamics. Similar temperature effects are observed for higher confinement ratios, namely 6.9 and 9.6. In contrast, increasing the confinement ratio causes the flame base to lift off and move further downstream from the nozzle exit, as indicated by the white dots and red dashed line in Fig. 20. This effect is due to the larger inner recirculation zone vortices, as shown in Fig. 19, where it is

evident that increasing the confinement ratio enlarges the inner recirculation zones and the reverse flow region. Fig. 21 quantitatively illustrates the effects of both inlet temperature and confinement ratio. OH* flame intensity correlates linearly with inlet temperature, as higher flame temperatures lead to more OH* radical emissions. Interestingly, with higher confinement ratios, OH* intensity becomes less sensitive to changes in inlet temperature, as the OH* intensity is more distributed in combustors with larger flames, which are associated with larger confinement ratios. However, as the confinement ratio decreases, OH* intensity increases, meaning that when the flame is more confined (e.g., the 5.6 confinement ratio), OH* emissions are concentrated in a smaller region of the combustor, resulting in higher OH* intensity than in larger flames generated with higher confinement ratios.

The SPOD spectrum in Fig. 22 demonstrates the effects of inlet temperature and confinement ratio on flame coherence. As temperature increases, the peaks of dominant modes gain amplitude across all confinement ratios, indicating that higher inlet temperatures lead to more coherent flame structures due to the increased velocity, which intensifies the swirling flow and thus enhances flame coherence. Interestingly, at the largest confinement ratio (9.6), the frequency of the dominant modes remains nearly constant across all inlet temperature cases, indicating reduced sensitivity to changes in inlet air temperature as the confinement ratio increases. This finding is consistent with the results discussed in Fig. 21. However, the structure of the dynamic mode becomes more coherent as the inlet temperature increases. Additionally, dominant mode frequencies are linearly correlated with temperature. Thus, as confinement ratio increases and OH* intensity decreases, the dominant mode frequency also decreases. Furthermore, the dominant mode shape transitions from radial to axial fluctuation mode at a 5.6 confinement ratio as inlet temperature increases from 300K to 500K, with the flame transitioning from an M-flame to a V-

flame. However, for the 6.9 and 9.6 confinement ratios, radial fluctuation mode remains dominant regardless of temperature. At higher temperatures, additional modes, such as the 400 Hz mode for the 5.6 case and the 800 Hz mode for the 6.9 case, become noticeable (as indicated by black arrows). For the 6.9 confinement ratio at 500K, Fig. 23 illustrates three distinct modes, with radial fluctuation as the dominant structure. The FFT results from microphone data in Fig. 24 show that as inlet temperature increases, low-frequency noise modes diminish, especially in the more confined 5.6 ratio flame. This suggests that more coherent flame structures, such as the V-flame, increase acoustic noise and reduce turbulence noise. In contrast, at higher confinement ratios—such as the 9.6 case—microphone data becomes noisier regardless of inlet temperature, as the flame becomes less coherent and more turbulence is introduced into the system. The microphone FFT results also reveal a competition between the three modes shown in Fig. 23, with the flame structure determining the dominant mode.

The acoustic-flame interaction for these cases is demonstrated in the phase-averaged results in Fig. 25. The hypothesis is that the combustion chamber can be acoustically treated as a closed-open tube, with the fundamental mode being a longitudinal (axial) quarter-wave mode, as there is no exit plate installed. Thus, depending on the swirling jet penetration angle (axial or radial) and the corresponding flame dynamic mode—which are controlled by the size and location of the inner recirculation zone vortices and influenced by the velocity field associated with varying inlet air temperatures and confinement ratios, the flame can either couple or decouple with the longitudinal acoustic mode of the combustion chamber. In some cases, the flame can also couple with a sub-harmonic mode of the combustion chamber. These coupling mechanisms impact the overall sound intensity (or combustion noise) measured by the microphone outside the combustion chamber. For example, in the M-flame case at 300K with a 5.6 confinement ratio, relatively larger inner

recirculation zone vortices (compared to the V-flame at 500K) cause the swirling jets to penetrate radially. Therefore, the flame's dynamic mode, as shown in the SPOD results in Fig. 22, is a radial fluctuation mode, resulting in decoupling from the longitudinal (axial) mode of the combustion chamber. Conversely, when axial swirling jet penetration is enhanced by a reduced inner recirculation zone size at higher inlet temperatures (and thus higher velocity fields), as in the V-flame case at 500K with a 5.6 confinement ratio, the axial fluctuation mode becomes the dominant dynamic mode of the flame. In this case, the flame couples with the longitudinal acoustic mode of the combustion chamber. However, in certain cases, the flame can couple with sub-harmonic acoustic modes (see the microphone FFT results in Fig. 24). For instance, in the M-flame case at 400K with the 5.6 confinement ratio, the dominant dynamic mode of the flame is radial fluctuation, which does not align with the fundamental longitudinal quarter-wave mode of the combustion chamber. Yet, the flame still couples with the acoustic field, though the combustion noise intensity is approximately 10 dB lower than when the flame couples with the longitudinal fundamental mode, as in the V-flame at 500K with the 5.6 confinement ratio. This can be observed in Fig. 26, where the solid black (500K) and yellow (400K) lines of the 5.6 confinement ratio are near stoichiometry. When the confinement ratio increases (e.g., to 9.6), the flame generally tends to decouple from the acoustic mode of the combustion chamber. This is due to the radial dispersion of swirling jets, which is promoted by larger inner recirculation zones, causing the radial fluctuation dynamic mode to dominate and thus decoupling the flame from the fundamental longitudinal acoustic mode of the combustion chamber. However, flames associated with radial fluctuations at higher confinement ratios (e.g., 6.9 and 9.6 at 300K) may still couple with the sub-harmonic acoustic field of the combustion chamber rather than the fundamental longitudinal mode. This coupling leads to relatively lower SPL levels compared to flames coupled with the

longitudinal mode, a behavior also observed in the 5.6 confinement ratio case at 400K (see Fig. 26). Additionally, at larger confinement ratios, such as 9.6, increasing the inlet air temperature enhances flame-acoustic coupling. This occurs due to the formation of a more coherent flame structure and reduced turbulence associated with the increased swirling flow intensity that accompanies higher inlet air temperatures. A shift between pressure and OH* flame intensity peaks at 400K and 500K can be observed in the phase-averaged results, where the flame transitions from being completely out-of-phase at 400K to coupling with the sub-harmonic mode at 500K (see the red values in the microphone FFT results in Fig. 24), resulting in a higher SPL magnitude, as shown in Fig. 26.

For a deeper understanding of the effects of inlet temperature and confinement ratio on combustion noise, the averaged SPL results from microphone measurements are shown in Fig. 26. SPL correlates linearly with temperature across all confinement ratios and inversely with confinement ratio. For example, for a specific confinement ratio at the highest equivalence ratio, SPL increases by approximately 15 dB as temperature rises from 300K to 500K, due the increased speed of sound, which affects the measured sound intensity. Conversely, increasing confinement ratio decreases SPL, with a 15 dB reduction observed between 5.6 and 9.6 confinement ratios, as the flame becomes less coherent with higher confinement ratios. These results underscore the significant impact of flame structure and coherent dynamic modes on combustion noise. As the flame adopts a more coherent structure, such as the axial fluctuation mode associated with vortex roll-up (common in V-flames), combustion noise increases, making the flame the main noise source. In contrast, when the dynamic mode is radial (associated with flame angle fluctuations) in either V-flame or M-flame configurations—achieved by lowering inlet temperature or increasing

confinement ratio—combustion noise is significantly reduced, with turbulence contributing more to noise production.

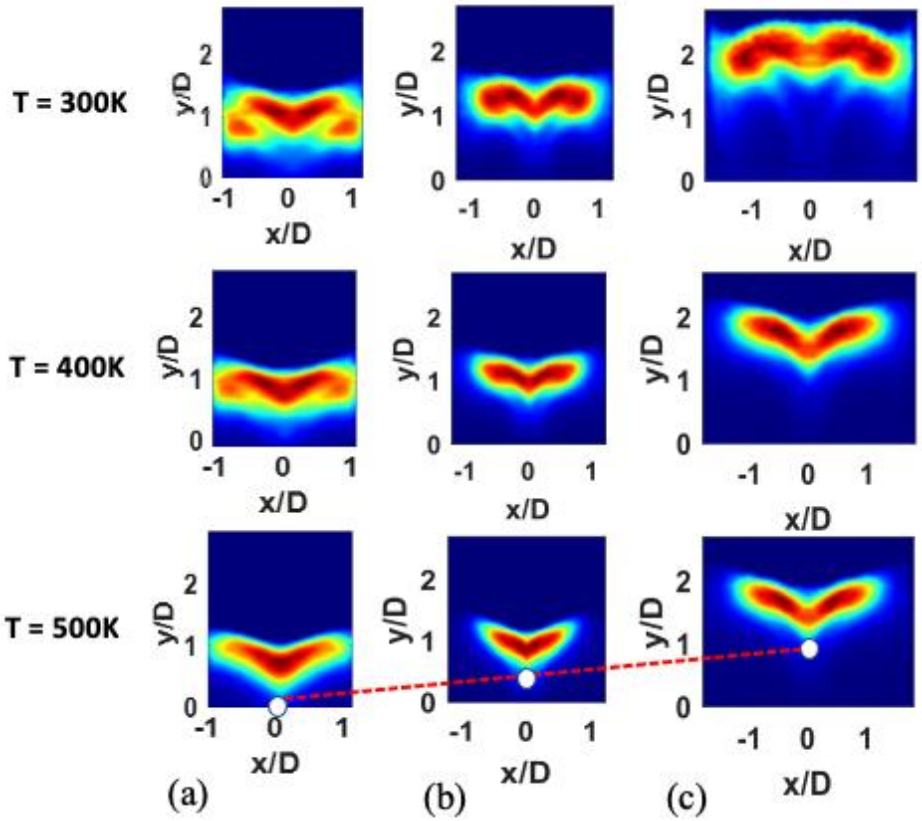

Figure 20. Averaged Abel-deconvoluted OH* flame images of (a) 5.6 (b) 6.9, and (c) 9.6 confinement ratios at near stichometry. The inlet temperature increases from top to bottom of the figure.

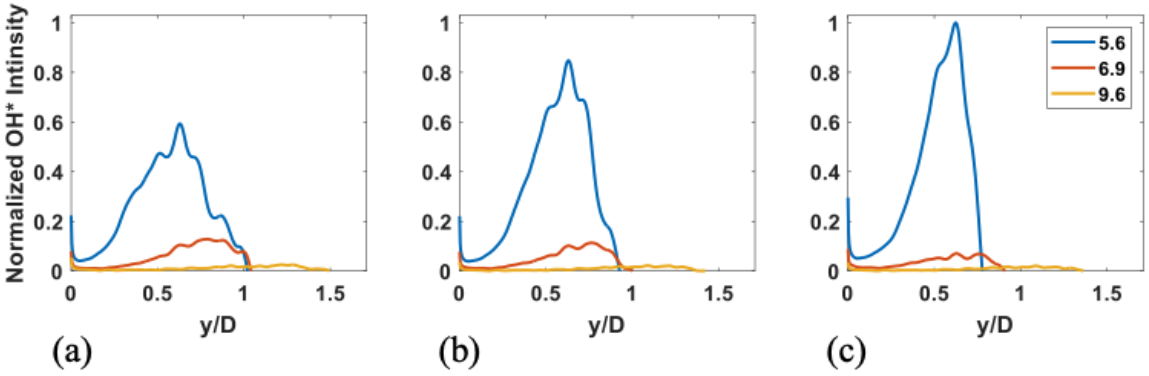

Figure 21. OH* intensity along the central line of the three confinement ratios with (a) 300 K (b) 400 K, and (c) 500 K inlet temperatures at near stichometry.

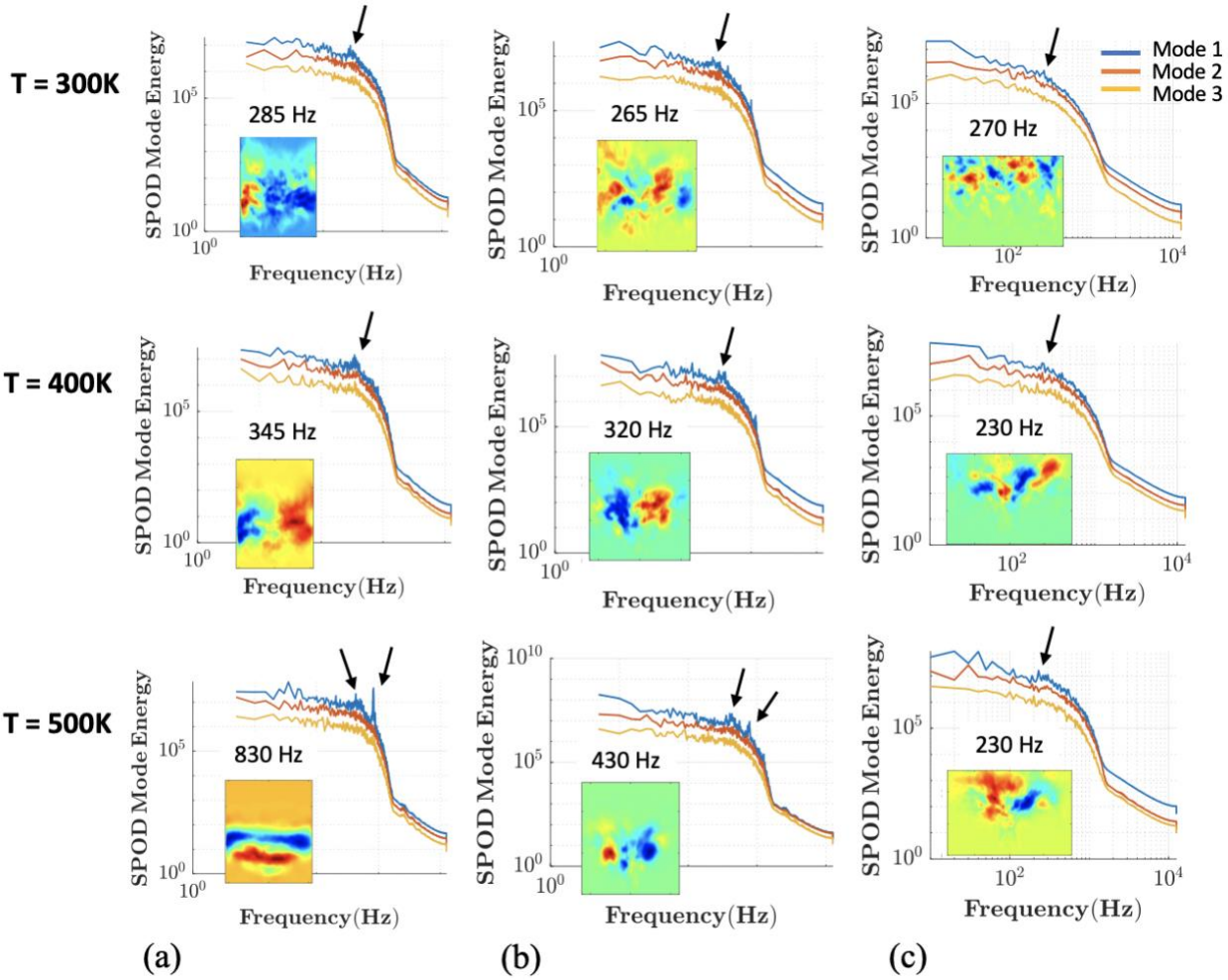

Figure 22. SPOD modes of the OH* flame images for (a) 5.6 (b) 6.9, and (c) 9.6 confinement ratios at near stichometry. The inlet temperature increases from top to bottom of the figure.

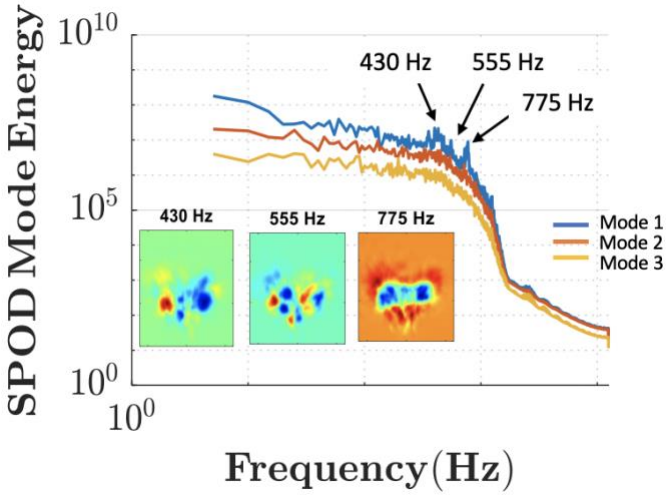

Figure 23. SPOD modes of the 6.9 confinement ratio with 500 K inlet temperature.

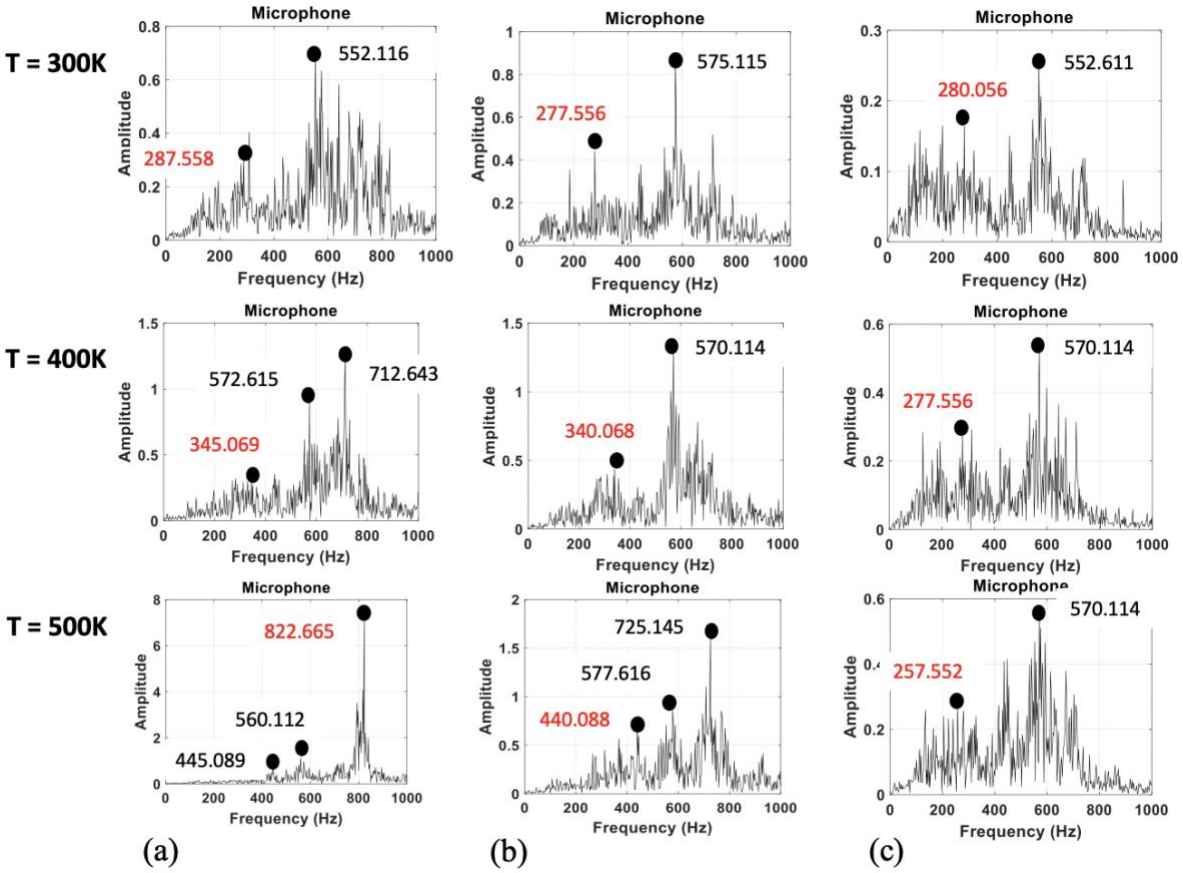

Figure 24. FFT results of the microphone measurements for (a) 5.6 (b) 6.9, and (c) 9.6 confinement ratios. The inlet temperature increases from top to bottom of the figure. The red color values indicate the dominant SPOD modes of the OH* flame.

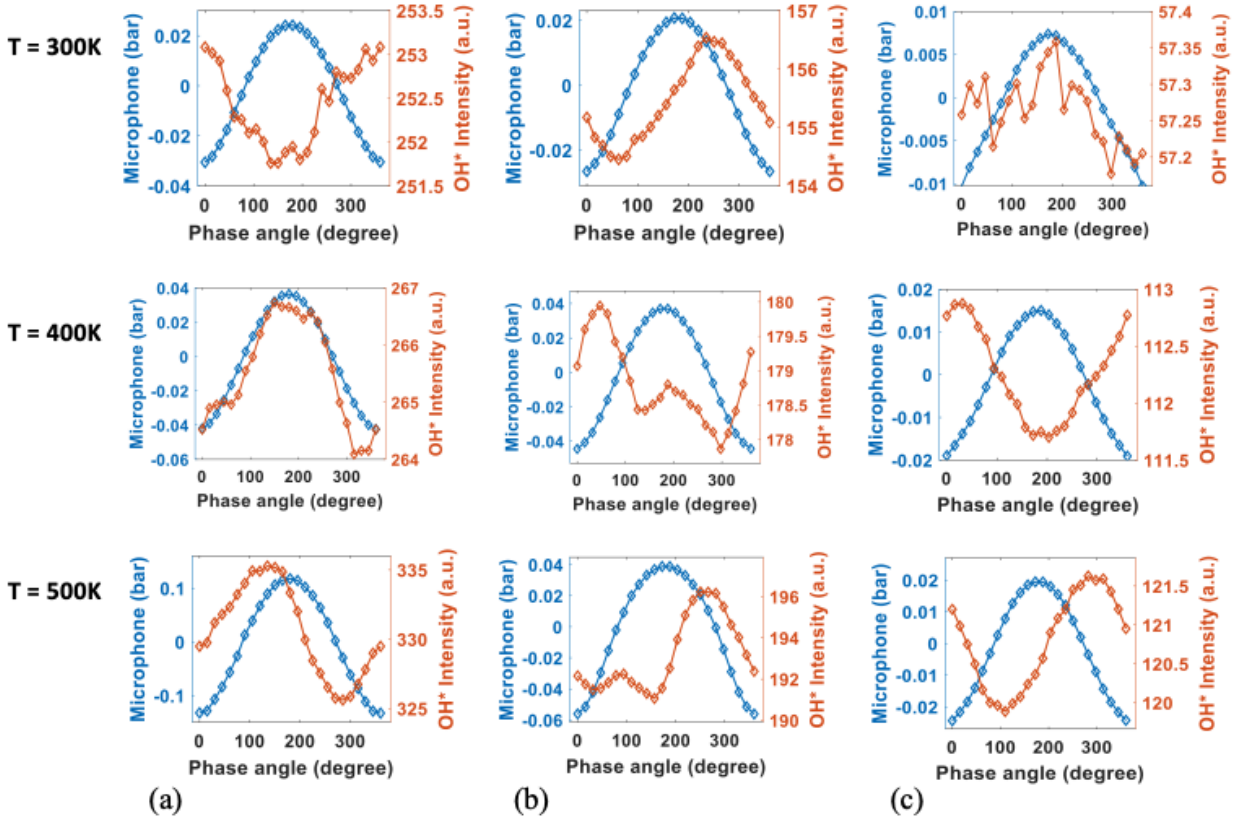

Figure 25. Phase-averaged results between the microphone and OH* for (a) 5.6 (b) 6.9, and (c) 9.6 confinement ratios near stichometry. The inlet temperature increases from top to bottom of the figure.

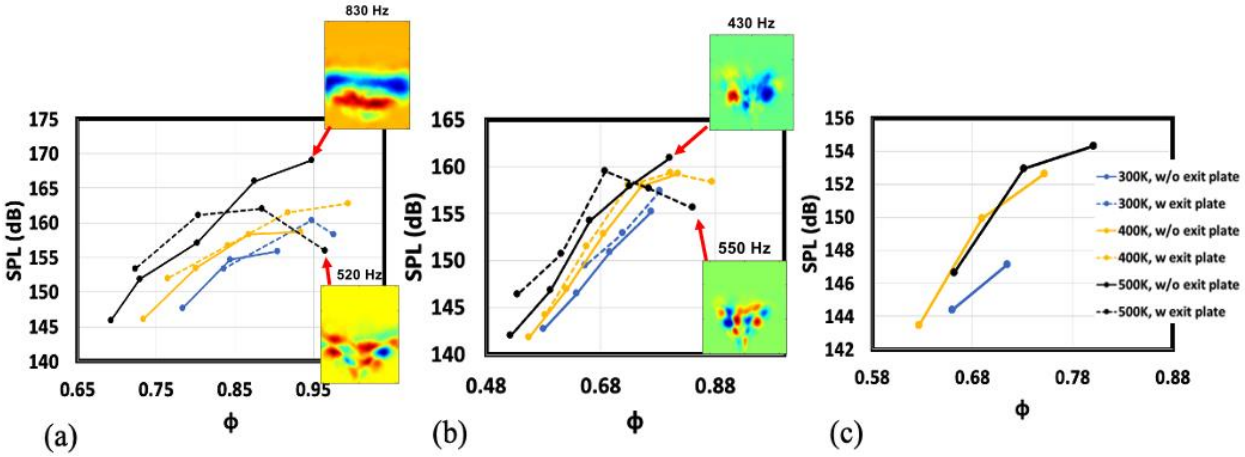

Figure 26. Averaged SPL results of the microphone measurements for (a) 5.6, (b) 6.9, and (c) 9.6 confinement ratios.

3.3. Exit Boundary Effects

Several researchers have demonstrated that the exit boundary affects flow structure and precessing vortex dynamics. Increased constriction forces the vortex breakdown point upstream, influencing the swirling jet [56]. Additionally, the exit boundary impacts flame stability by altering reflection coefficients and acoustic mode shapes [57]. It also influences the flow's susceptibility to downstream perturbations and affects the frequency and amplitude of thermoacoustic instability modes within the combustor. This recent study explained that modifying the exit boundary condition can alter thermoacoustic modes without changing the flame's operating conditions, suggesting that thermoacoustic instability can be suppressed by changing the exit boundary conditions. Therefore, understanding flame behavior under different exit boundary conditions is an important aspect of studying combustion dynamics in the MLDI system. The effects of the exit boundary on flame structure are illustrated in Fig. 27 for the 5.6 and 6.9 confinement ratios at a near-stoichiometric equivalence ratio, with an inlet air temperature of 500K. The flame anchoring point shifts upstream toward the nozzle exit, caused by an increased pressure gradient in the reverse flow region after adding the exit plate, which forces the vortex breakdown point upstream. Fig. 28 shows that OH* intensity increases after installing the exit plate, as the increased pressure gradient in the combustion chamber compresses OH* species into a smaller region. The SPOD results in Fig. 29 indicate that the exit plate modifies the flame's dynamic mode and shifts the frequency. In both the 5.6 and 6.9 cases, dynamic fluctuations after adding the exit plate occur simultaneously in both axial and radial directions, with a dominant mode around 550 Hz. This 550 Hz mode existed prior to adding the exit plate (as shown in Fig. 23), but its prominence increases, overtaking the axial (around 800 Hz) and radial (around 400 Hz) modes. The addition of the exit plate leads to a dominance of simultaneous axial-radial fluctuation modes, induced by an increased pressure

gradient. This alteration affects the vortices within the inner recirculation zone, thereby impacting the penetration of the swirling jet. Consequently, the enhancement of the axial-radial mode due to the exit plate causes the flame to exhibit simultaneous vortex roll-up and flame angle fluctuation motions. In Fig. 30, the SPOD results reveal that both the axial fluctuation mode and a new axial-radial fluctuation mode co-exist after adding the plate, with the axial-radial mode becoming dominant. Similarly, the FFT results of microphone data in Fig. 31 reflect the same competitive behavior among the three modes, with the new axial-radial mode (around 550 Hz) being amplified after adding the exit plate. These findings explain the significant reduction in SPL magnitude, 15 dB for the 5.6 confinement ratio and 5 dB for the 6.9 confinement ratio, at the highest equivalence ratio after adding the exit plate (see Fig. 26, red arrows). When flame fluctuations occur in both axial and radial directions simultaneously, the motions partially cancel each other out, leading to a lower SPL magnitude. In contrast, when either the axial mode (vortex roll-up), as in the 5.6 confinement ratio case without the exit plate, or radial mode (flame angle fluctuation), as in the 6.9 confinement ratio case without the exit plate, is dominant, there is no interference mechanism, resulting in a notably higher SPL magnitude. To further illustrate the canceling mechanism, Fig. 32 from Palies et al.'s work on the flame transfer function shows that axial and azimuthal velocity fluctuations are in-phase during modes with maximum gain (lower plot) and out-of-phase, thus canceling each other, during modes with minimum gain (upper plot) [51].

To examine the effects of these parameters on the LBO limit, which is important for managing thermal NOx emissions by enabling the fuel nozzle to operate at lower equivalence ratios, Fig. 33 presents LBO limits across different parameters. The LBO value decreases with increasing inlet air temperature, as higher temperatures accelerate fuel combustion, allowing the reaction to occur at lower fuel rates and equivalence ratios. However, increasing the inlet

temperature also results in a higher peak flame temperature. This means that although the LBO limit is reduced at higher inlet temperature, the flame may still produce higher NOx emission due to the elevated peak temperatures associated with the increased inlet air temperature. Additionally, higher confinement ratios significantly reduce the LBO limit due to the enlarged inner recirculation vortices, which constrain the jet in a smaller area and increase the air requirement to maintain a 2% pressure drop across the nozzle, resulting in a lower equivalence ratio at higher confinement ratios. However, the 9.6 confinement ratio shows some nonlinearity as the flame at LBO conditions is already unsteady. With the 9.6 confinement ratio, the flame becomes a lifted flame with a less coherent structure, leading to fluctuations that can oppose the incoming airflow and reduce it, resulting in a slight increase in the equivalence ratio. Lastly, adding the exit plate increases the LBO limit due to the heightened pressure gradient in the reverse flow region, which reduces the incoming air's flow rate, leading to a higher equivalence ratio.

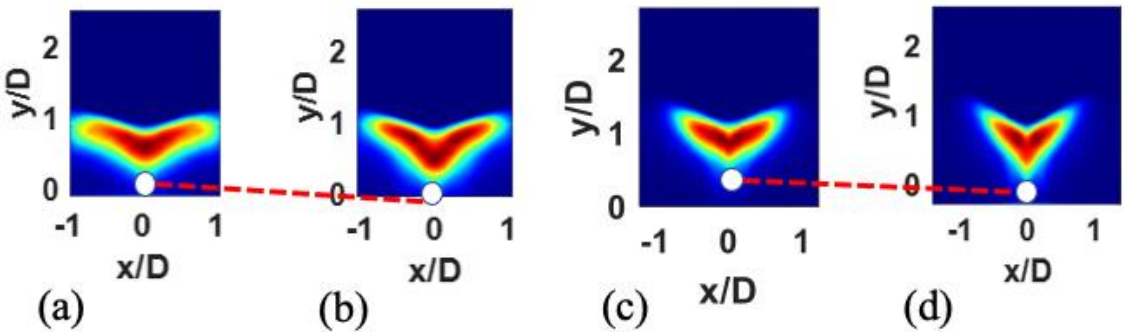

Figure 27. Averaged Abel-deconvoluted OH* flame images with 500K inlet temperature at near-stichometry equivalence ratio of the (a) 5.6 case without exit plate, (b) 5.6 case with exit plate, (c) 6.9 case without exit plate, and (c) 6.9 case with exit plate.

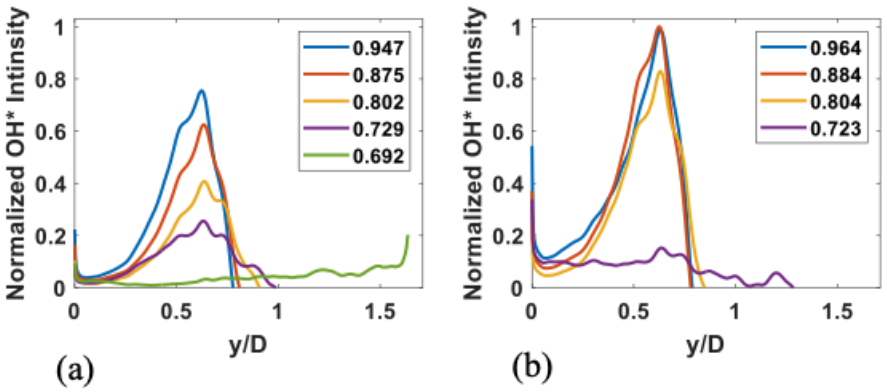

Figure 28. OH* intensity line plot along the central line of the 5.6 confinement ratio case at 500K (a) without exit plate, and (b) with exit plate.

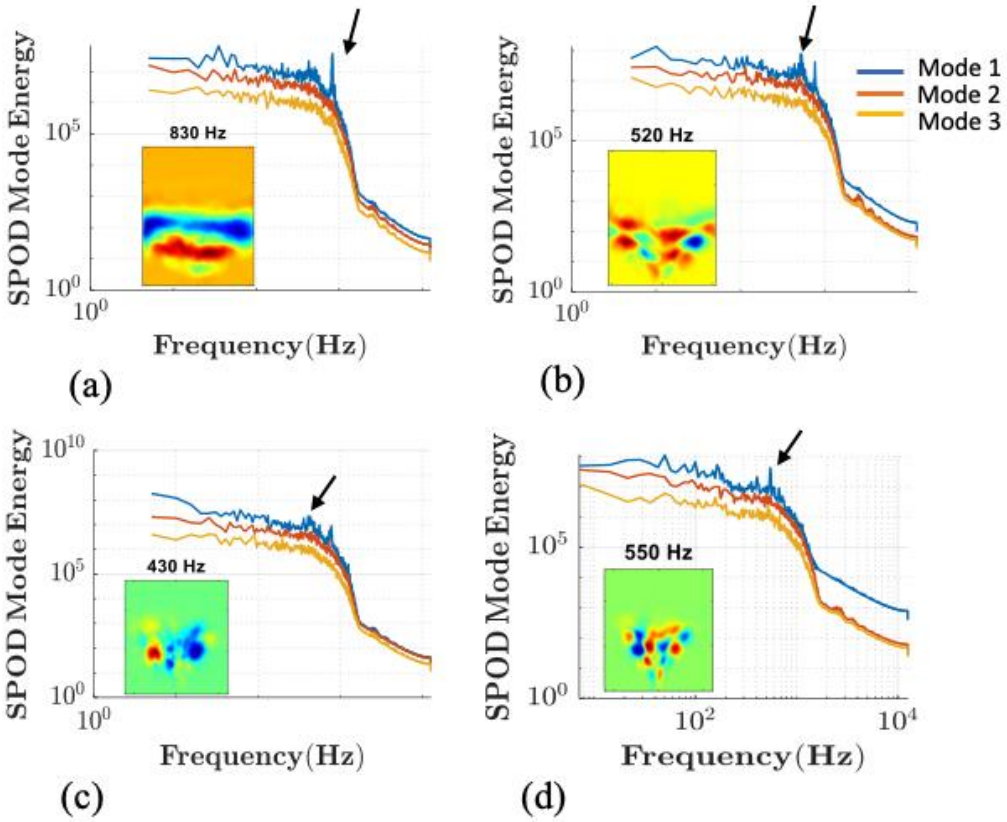

Figure 29. SPOD modes of the (a) 5.6 case without exit plate, (b) 5.6 case with exit plate, (c) 6.9 case without exit plate, and (d) 6.9 case with exit plate with 500K inlet temperature near-stichometry.

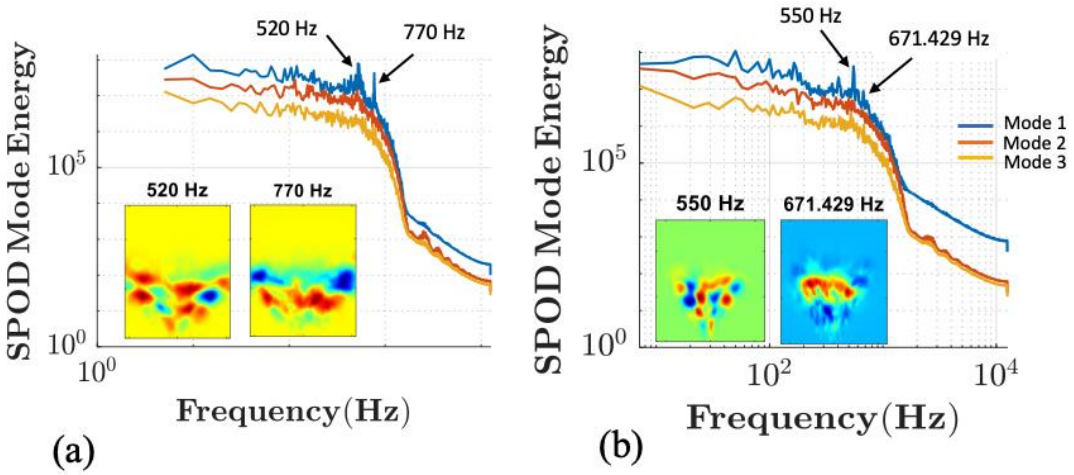

Figure 30. SPOD modes of the (a) 5.6 case with exit plate, and (b) 6.9 case with exit plate.

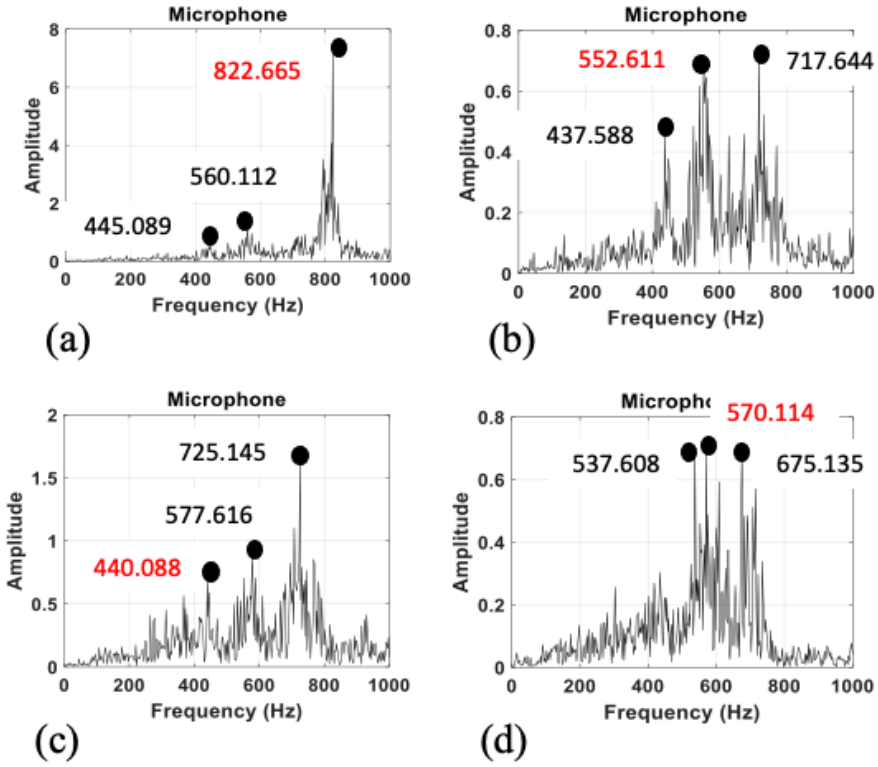

Figure 31. FFT results of the microphone data for (a) 5.6 case without exit plate, (b) 5.6 case with exit plate, (c) 6.9 case without exit plate, and (d) 6.9 case with exit plate. The red color values indicate the dominant SPOD mode.

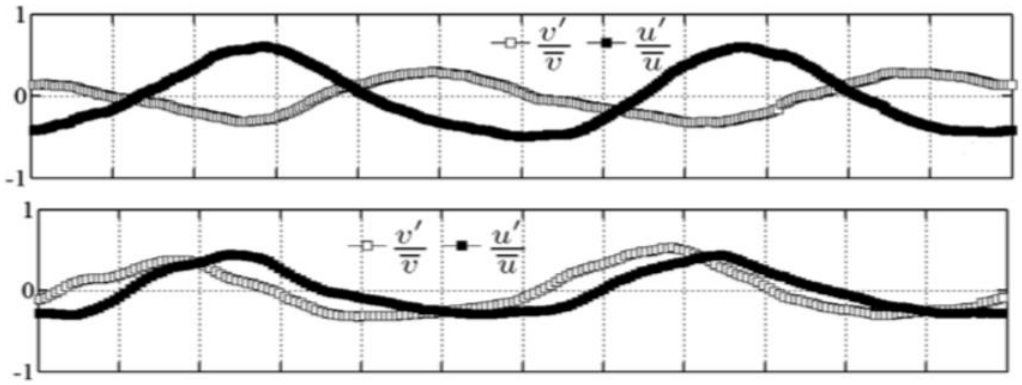

Figure 32. Upper plot: velocity fluctuations field during the minimum gain mode. Lower plot: velocity fluctuations field during the maximum gain mode. u = axial velocity, v = azimuthal velocity [51]**.**

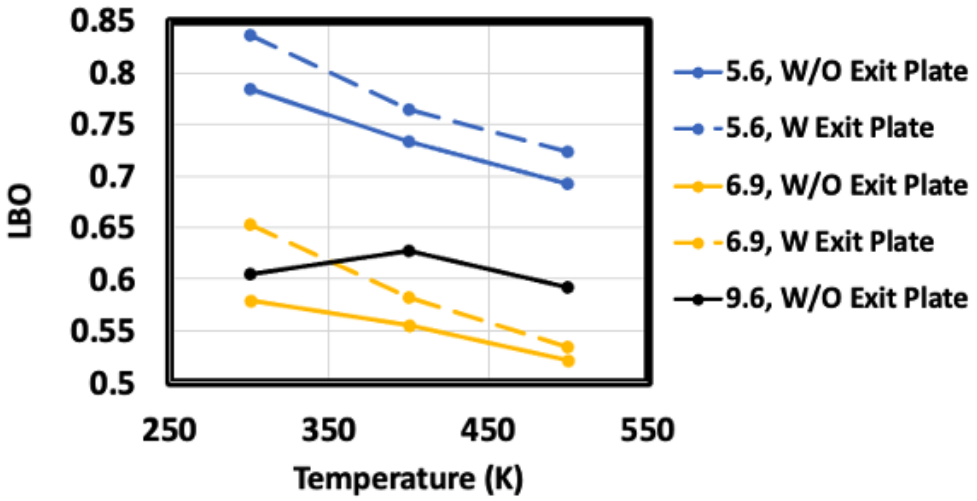

Figure 33. line plot of the LBO limit vs. inlet temperature for all the confinement ratios with and without exit plate.

4. Conclusion

The equivalence ratio effects on the single-element low-emission nozzle used in the MLDI combustion system were thoroughly characterized in this study. A high-speed OH* chemiluminescence technique, combined with acoustic microphone measurements acquired outside the combustion chamber, was employed to identify and analyze three distinct flame structures: the V-flame, M-flame (with the M-V flame as a transient phase), and lifted-distributed flames. The results revealed significant differences between these flame structures. The V-flame exhibited the highest OH* intensity, concentrated primarily in the central region of the flame, creating a hot spot that may lead to higher thermal NOx emissions. In contrast, the M-flame and lifted-distributed flames displayed lower and more spatially distributed reaction zones, which can help in reducing the formation of these hot spots, thereby mitigating thermal NOx formation. Interestingly, the V-flame, which occurred at higher equivalence ratios, was associated with axial fluctuation modes. In contrast, the M-flame and lifted-distributed flames, found at lower equivalence ratios, were dominated by radial fluctuations and non-coherent turbulence modes, respectively. The frequency values derived from both the SPOD mode and sound pressure measurements were remarkably similar—830 Hz and 822.65 Hz, respectively—during the V-flame condition at an equivalence ratio of $\phi = 0.947$, suggesting a coupling between the flame dynamics and the acoustic field. Phase-averaged results further supported these observations, showing that the flame's OH* intensity and acoustic pressure were in-phase during V-flame conditions. However, under M-flame conditions, the OH* intensity and sound pressure were out-of-phase, indicating a decoupling between the flame dynamics and acoustic field. The study also found a linear correlation between the measured sound pressure intensity and the equivalence ratio, with the V-flame producing the highest sound intensity, approximately 20 dB higher than that of

the M-flame and lifted-distributed flame. These findings suggest that, at higher equivalence ratios under V-flame conditions, flame-acoustic coupling is the primary source of noise. As the equivalence ratio decreases and the flame structure becomes less coherent, as seen at near LBO conditions, turbulent noise becomes the dominant sound source.

The effects of inlet temperature, confinement ratio, and exit plate on flame structure and dynamic modes are significant. Increasing the inlet temperature and adding the exit plate both shift the flame anchoring point upstream. This occurs because a higher inlet temperature decreases air density, which increases axial velocity and reduces the size of the inner recirculation zones, leading to a V-flame anchored near the nozzle exit. Similarly, adding the exit plate raises the pressure gradient in the reverse flow region, pushing the flame anchoring point upstream. Each parameter promotes a different flame dynamic mode. The axial fluctuation mode, associated with flame vortex roll-up, is magnified with increasing inlet temperature, particularly in more confined flames, such as those with a 5.6 confinement ratio. In contrast, the newly revealed axial-radial fluctuation mode (where both vortex roll-up and flame angle fluctuations occur simultaneously) is amplified after adding the exit plate. These changes in flame dynamics significantly affect frequency values and SPL measured by the microphone. A notable reduction of approximately 15 dB in SPL occurs when the flame mode shifts from axial fluctuations to axial-radial fluctuations after adding the exit plate at near-stoichiometric conditions. The confinement ratio also has a marked impact on flame structure, flame dynamic modes, and SPL values. As the confinement ratio increases, the size of the inner recirculation zone grows linearly, producing larger flames with lower OH* intensity, as the OH* species become more distributed. Larger confinement ratios, such as 6.9 and 9.6, promote the radial fluctuation mode associated with flame angle fluctuations. This is because the increased inner recirculation vortices push the jet radially, in contrast to the more

axial penetration seen with the 5.6 confinement ratio, where higher axial velocity promotes the axial fluctuation mode tied to vortex roll-up motion. Additionally, the frequency of the dominant dynamic modes promoted by the 9.6 confinement ratio was less sensitive to changes in inlet air temperature, suggesting that the flame becomes less sensitive to variations in inlet air temperature as the confinement ratio increases. These effects result in a significant SPL reduction of about 15 dB when comparing maximum values at near-stoichiometric conditions between confinement ratios of 5.6 and 9.6. This SPL decrease occurs because the radial fluctuation mode, associated with flame angle fluctuations, produces less SPL than the axial fluctuation mode linked to vortex roll-up. Based on the flame-acoustic phase-averaged results, it was hypothesized that the combustion chamber can be acoustically treated as a closed-open tube, with the fundamental mode being a longitudinal (axial) quarter-wave mode when there is no exit plate installed. Thus, depending on the swirling jet penetration angle (axial or radial) and the resulting flame dynamic mode—which are controlled by the size and location of the inner recirculation zone vortices and influenced by the velocity field associated with varying inlet air temperatures and confinement ratios—the flame can either couple or decouple with the longitudinal acoustic mode of the combustion chamber. When the axial fluctuation mode was dominant, the flame coupled with the longitudinal (axial) mode of the combustion chamber. When the radial fluctuation mode was dominant, the flame generally tended to decouple from the longitudinal mode of the combustion chamber. In some cases, the flame can also couple with a sub-harmonic mode of the combustion chamber. These coupling mechanisms affect the overall sound intensity (or combustion noise) measured by the microphone outside the combustion chamber. Finally, the LBO limit, important for reducing thermal NOx formation, is influenced by these parameters. In relatively hot environments created by increased inlet temperature, fuel burns at a lower rate, enabling

combustion at a lower equivalence ratio. However, due to the elevated peak temperature associated with higher inlet air temperatures, the flame may still produce relatively higher NOx emissions. Additionally, the larger inner recirculation zones associated with higher confinement ratios restrict the jet penetration area, requiring a higher airflow rate to maintain the pressure drop across the nozzle and resulting in a lower global equivalence ratio. Conversely, the addition of the exit plate raises the pressure gradient, slightly reducing airflow rate and increasing the equivalence ratio. In summary, this research characterizes the critical roles of equivalence ratio, inlet air temperature, confinement ratio, and exit boundary in determining flame structure, dynamic modes, OH* intensity, and sound intensity in the single-element low-emission nozzle used in the MLDI combustion system. Understanding these interactions is essential for optimizing efficiency and developing advanced design strategies for low-emission combustion systems.

5. Contributions

The significant contributions of this study can be summarized as follows:

1. This study provides a comprehensive characterization of flame dynamics in a single-element low-emission nozzle used in multipoint lean direct injection (MLDI) combustion systems.
2. This study explores how the equivalence ratio, inlet air temperature, confinement ratio, and exit boundary influence flame dynamics in a single-element low emission nozzle.
3. The findings reveal critical insights into flame-acoustic coupling and the transition between various dynamic modes, contributing to a deeper understanding of how flame dynamics influence combustion noise and thermal NOx emissions.
4. These results hold significant implications for optimizing efficiency and advancing design strategies for low-emission combustion systems.

Appendix

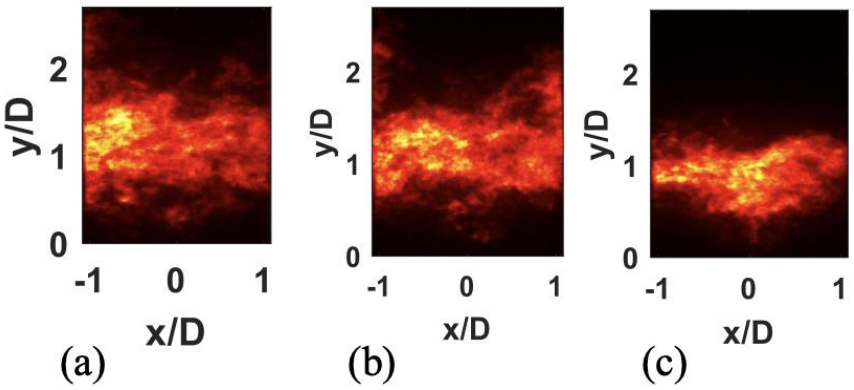

Figure 34. Instantaneous OH* flame images of the 5.6 confinement ratio without exit plate with (a) 300K, (b) 400K, and (c) 500K inlet air temperature at near-stoichiometric equivalence ratio.

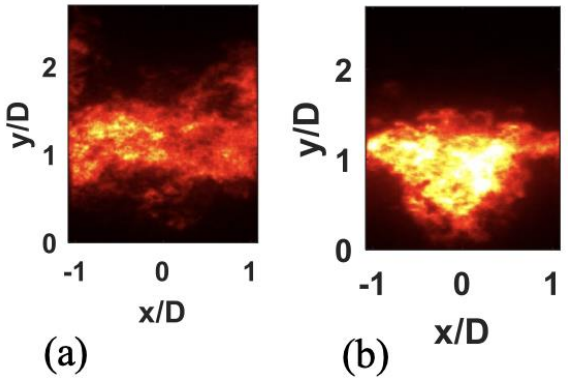

Figure 35. Instantaneous OH* flame images of the 5.6 confinement ratio. (a) without exit plate, and (b) with exit plate, with 500K inlet air temperature at near-stoichiometric equivalence ratio.

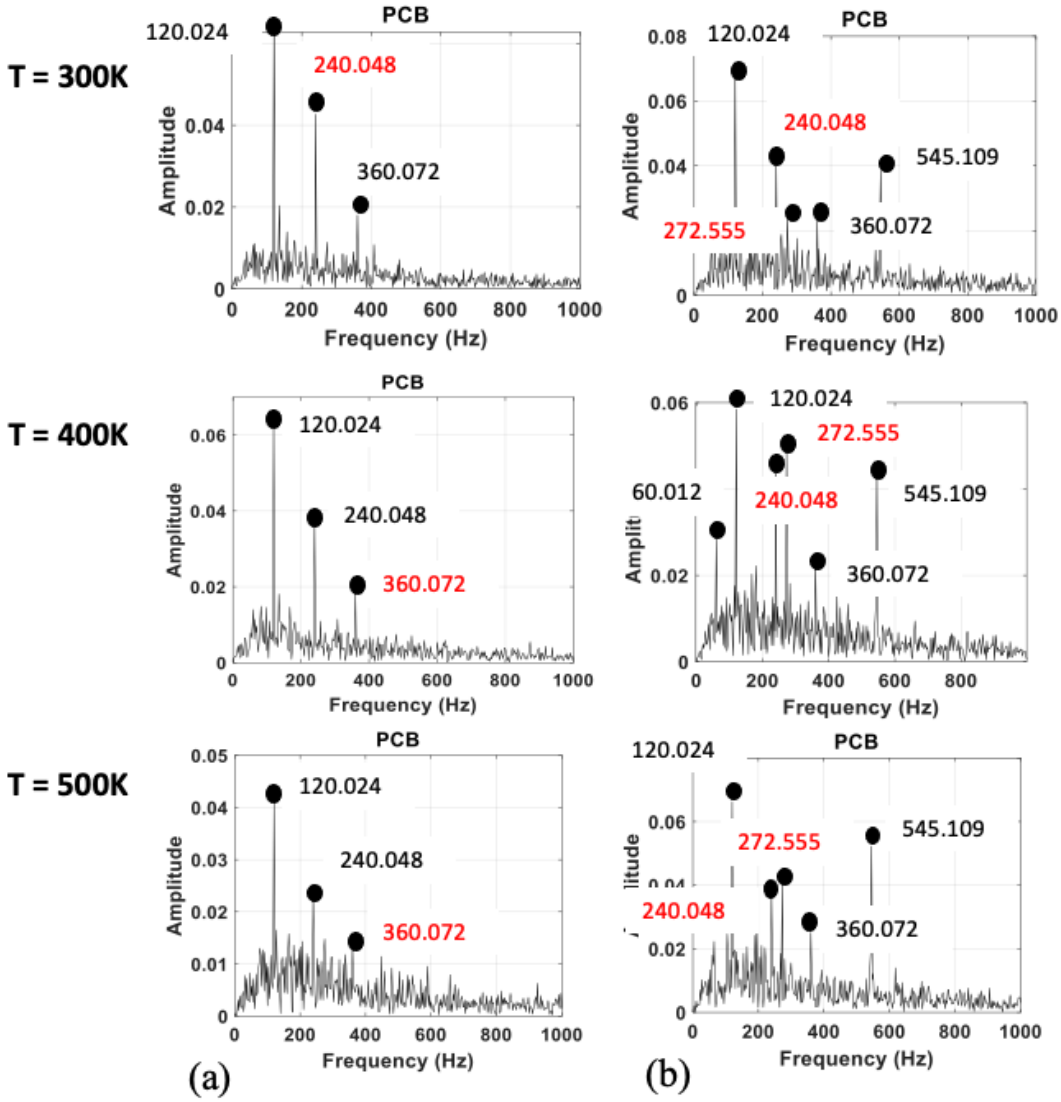

Figure 36. FFT results of the pressure PCB sensor located in the rectangular plenum upstream prior to the combustion chamber for (a) 6.9, and (c) 9.6 confinement ratios at near stichometry. The inlet temperature increases from top to bottom of the figure. The red color values indicate the dominant SPOD mode.

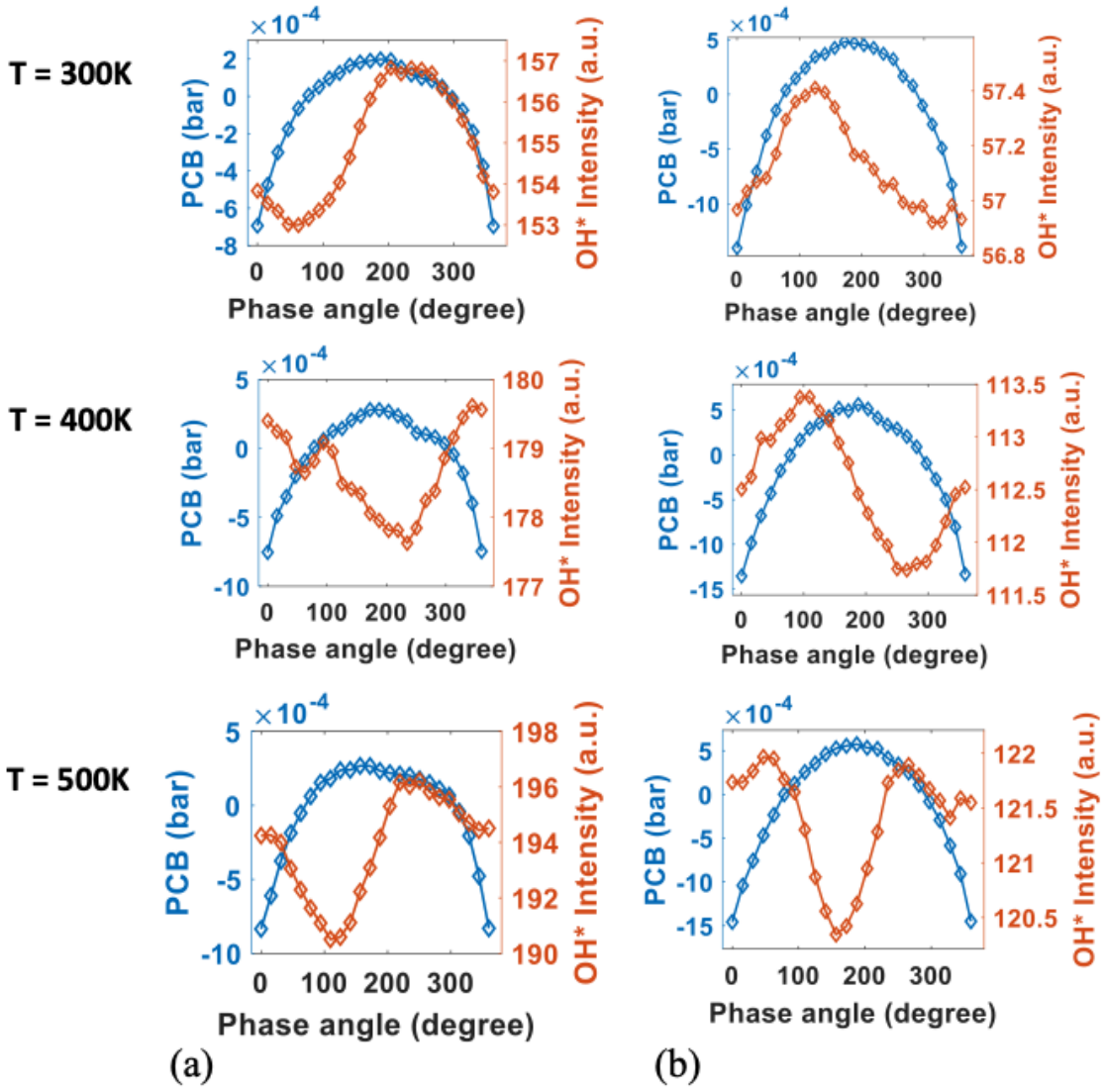

Figure 37. Phase-averaged results between the pressure in the upstream section and OH* for (a) 6.9, and (c) 9.6 confinement ratios at near stichometry. The inlet temperature increases from top to bottom of the figure.

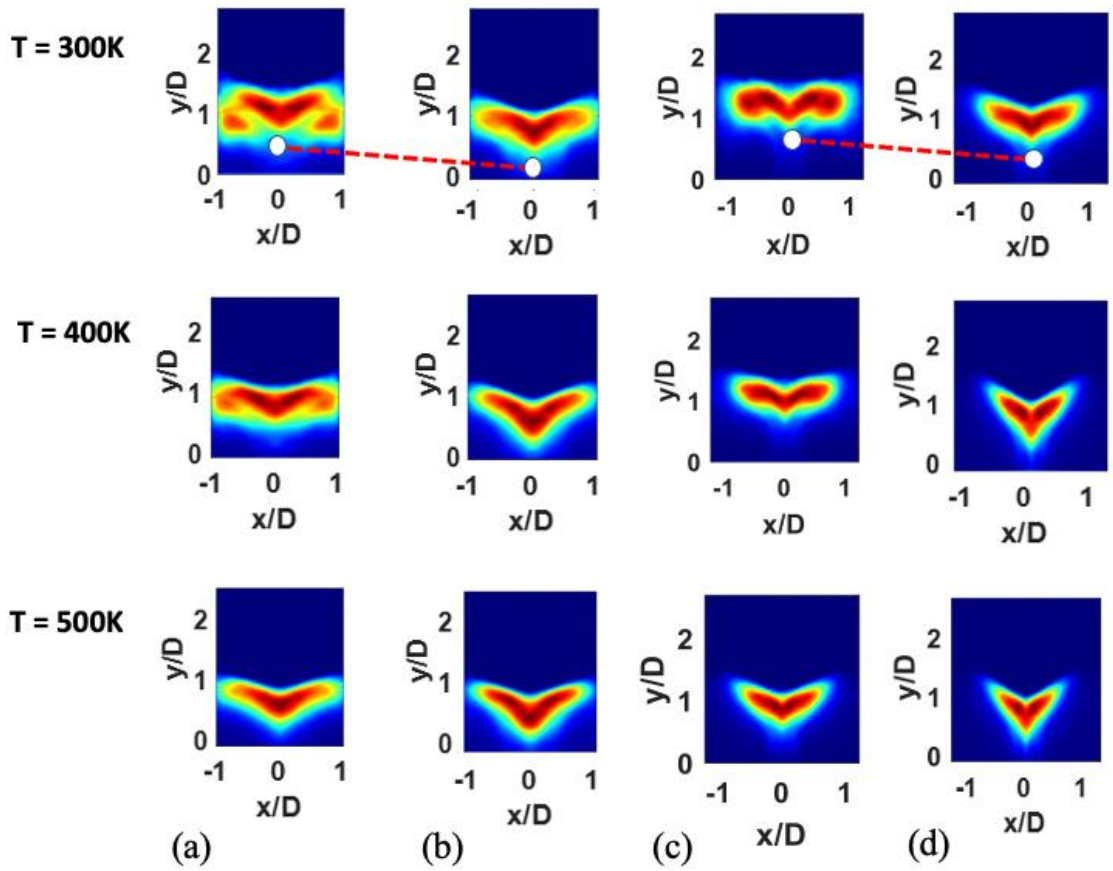

Figure 38. Averaged Abel-deconvoluted OH* flame images of the (a) 5.6 without exit plate, (b) 5.6 with exit plate, (c) 6.9 without exit plate, and (d) 6.9 with exit plate confinement ratios at near stichometry. The inlet temperature increases from top to bottom of the figure.

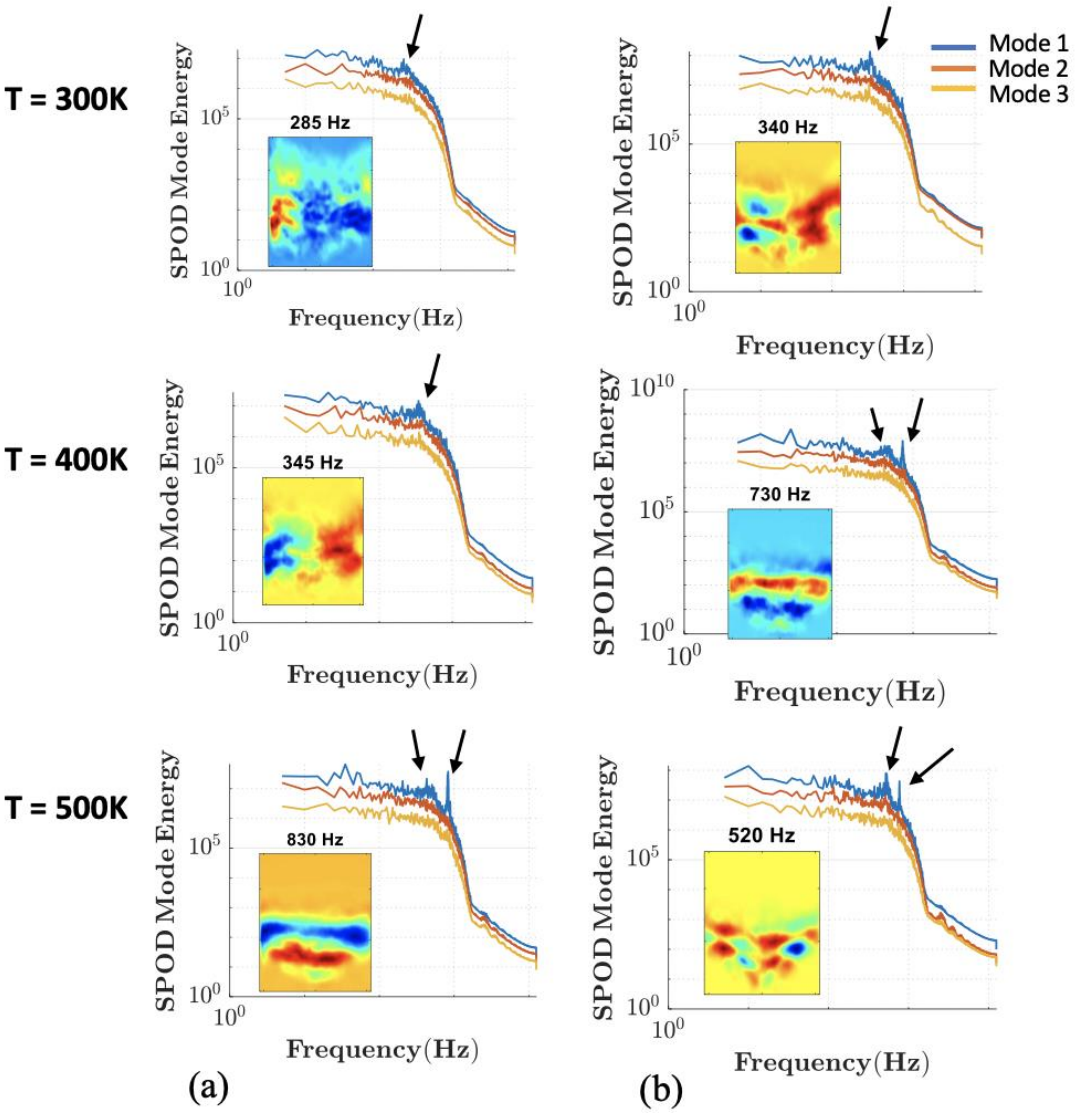

Figure 39. SPOD modes of the (a) 5.6 case without exit plate, and (b) 5.6 case with exit plate at near stichometry. The inlet temperature increases from top to bottom of the figure.

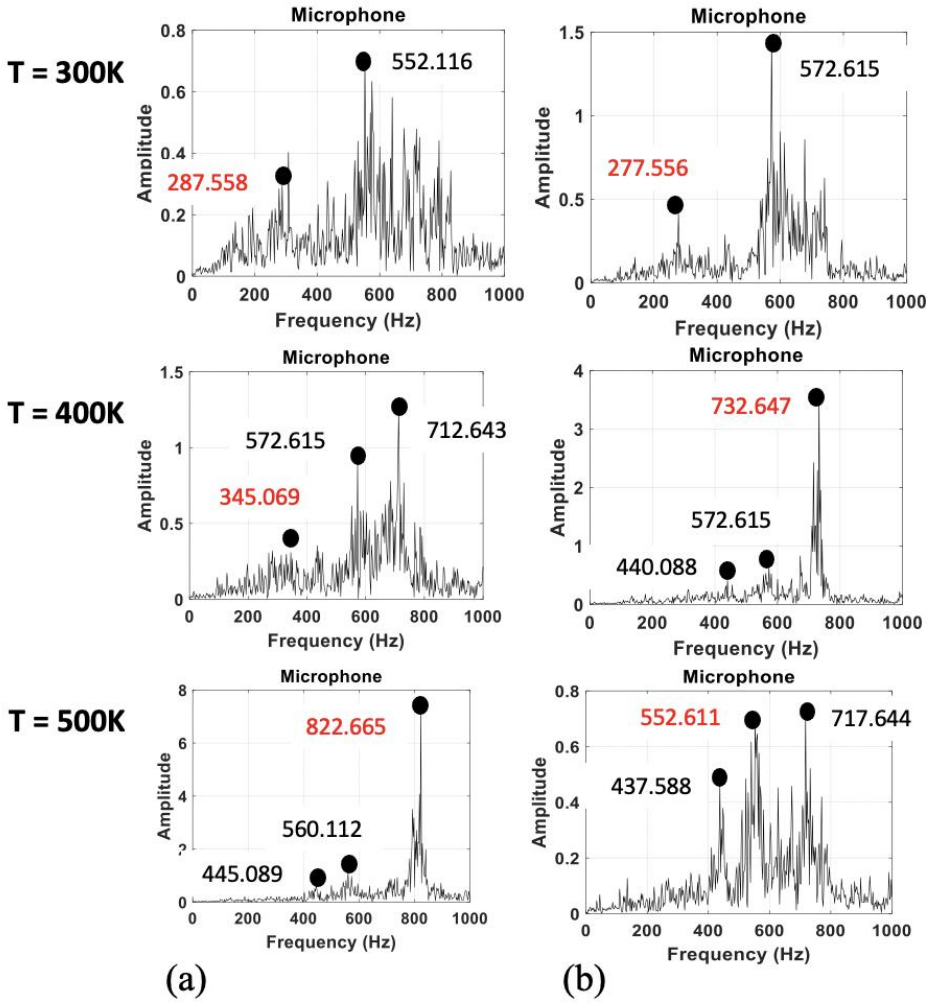

Figure 40. FFT results of the microphone data for (a) 5.6 case without exit plate, and (b) 5.6 case with exit plate at near stichometry. The inlet temperature increases from top to bottom of the figure.

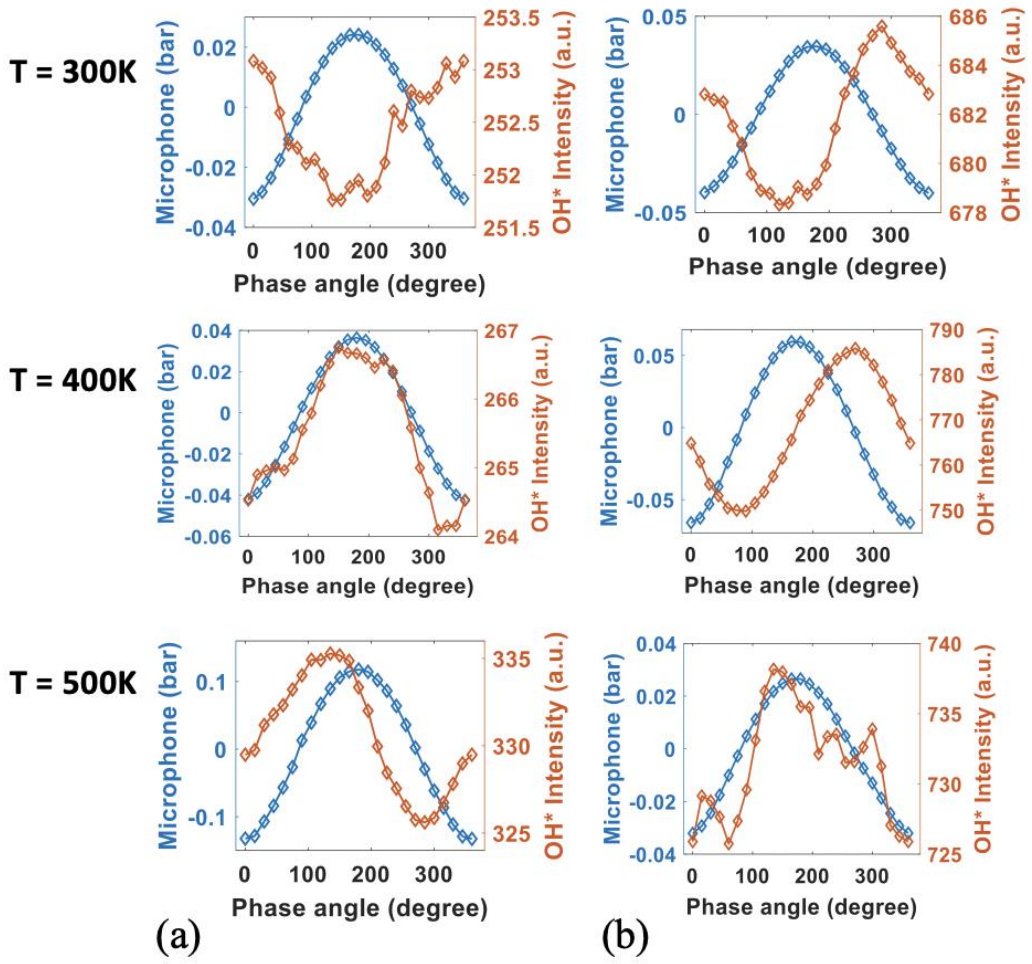

Figure 41. Phase-averaged results between the microphone and OH* for (a) 5.6 case without exit plate, and (b) 5.6 case with exit plate at near stichometry. The inlet temperature increases from top to bottom of the figure.

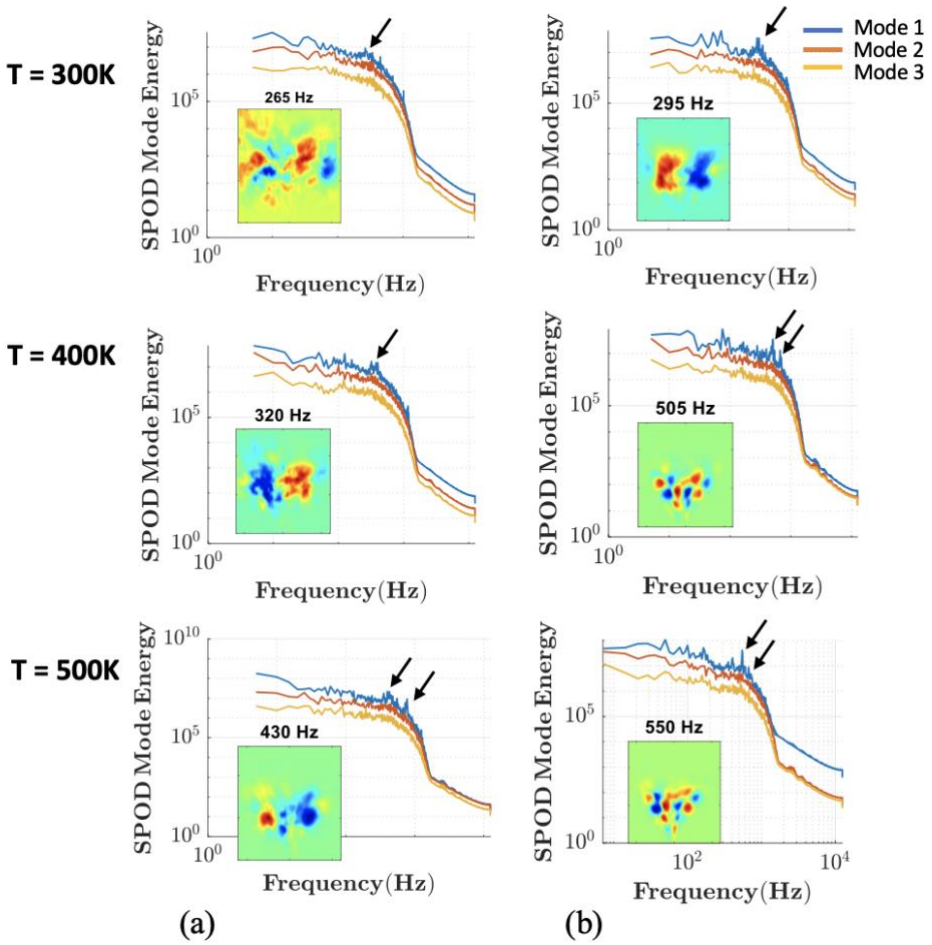

Figure 42. SPOD modes of the (a) 6.9 case without exit plate, and (b) 6.9 case with exit plate at near stichometry. The inlet temperature increases from top to bottom of the figure.

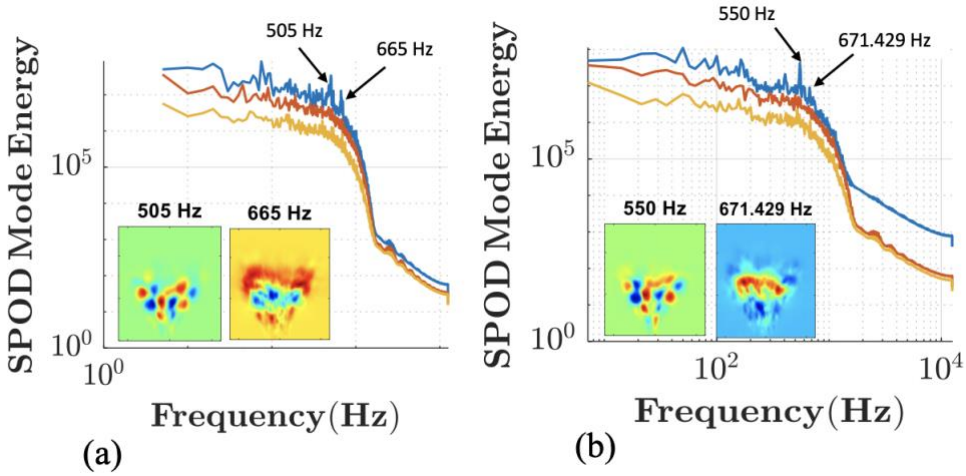

Figure 43. SPOD modes of the (a) 6.9 case with exit plate at 400K, and (b) 6.9 case with exit plate at 500K at near stichometry.

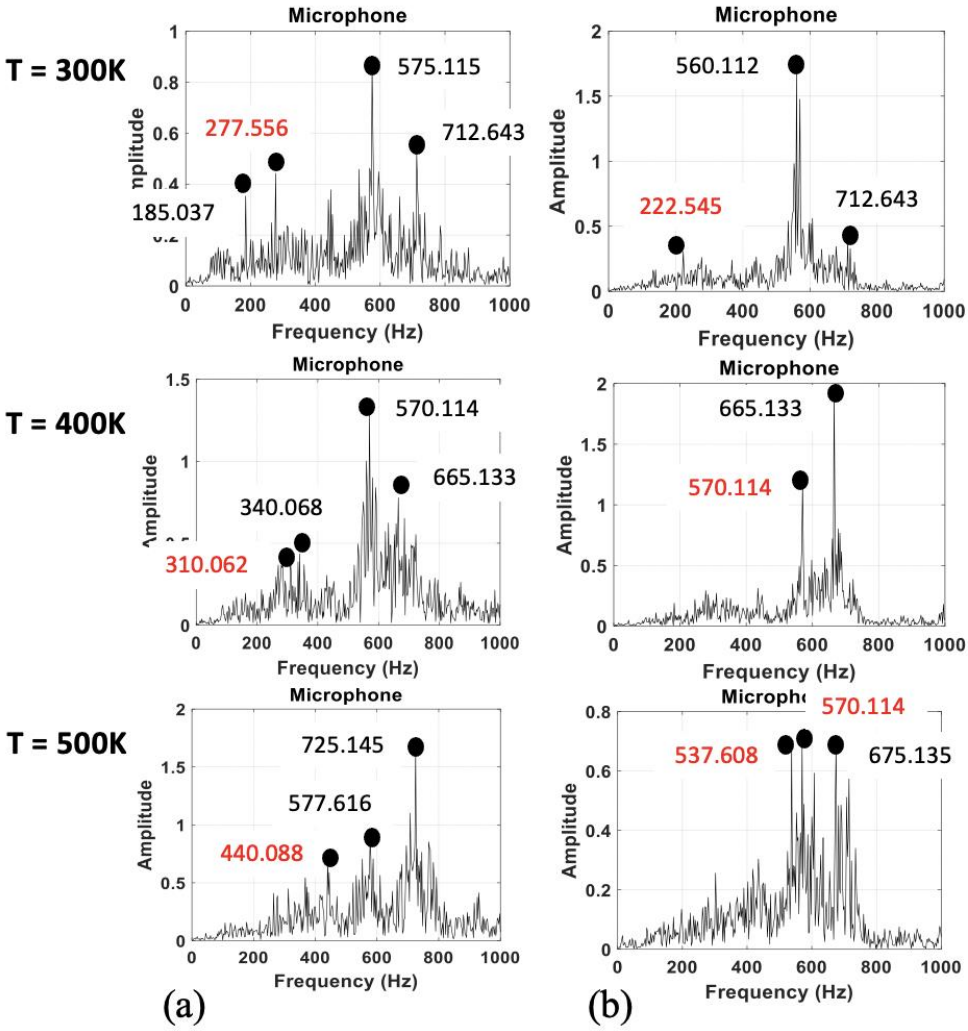

Figure 44. FFT results of the microphone data for (a) 6.9 case without exit plate, and (b) 6.9 case with exit plate at near stichometry. The inlet temperature increases from top to bottom of the figure.

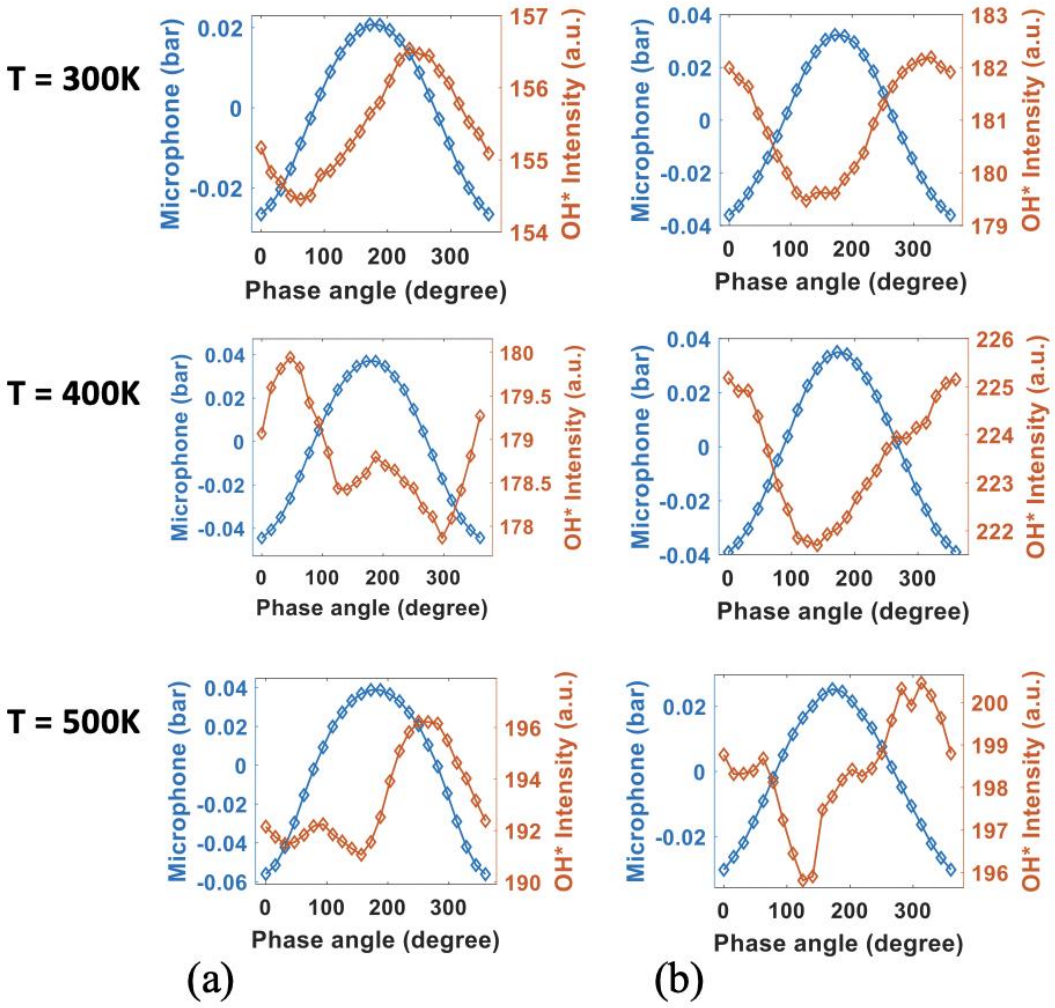

Figure 45. Phase-averaged results between the microphone and OH* for (a) 6.9 case without exit plate, and (b) 6.9 case with exit plate at near stichometry. The inlet temperature increases from top to bottom of the figure.

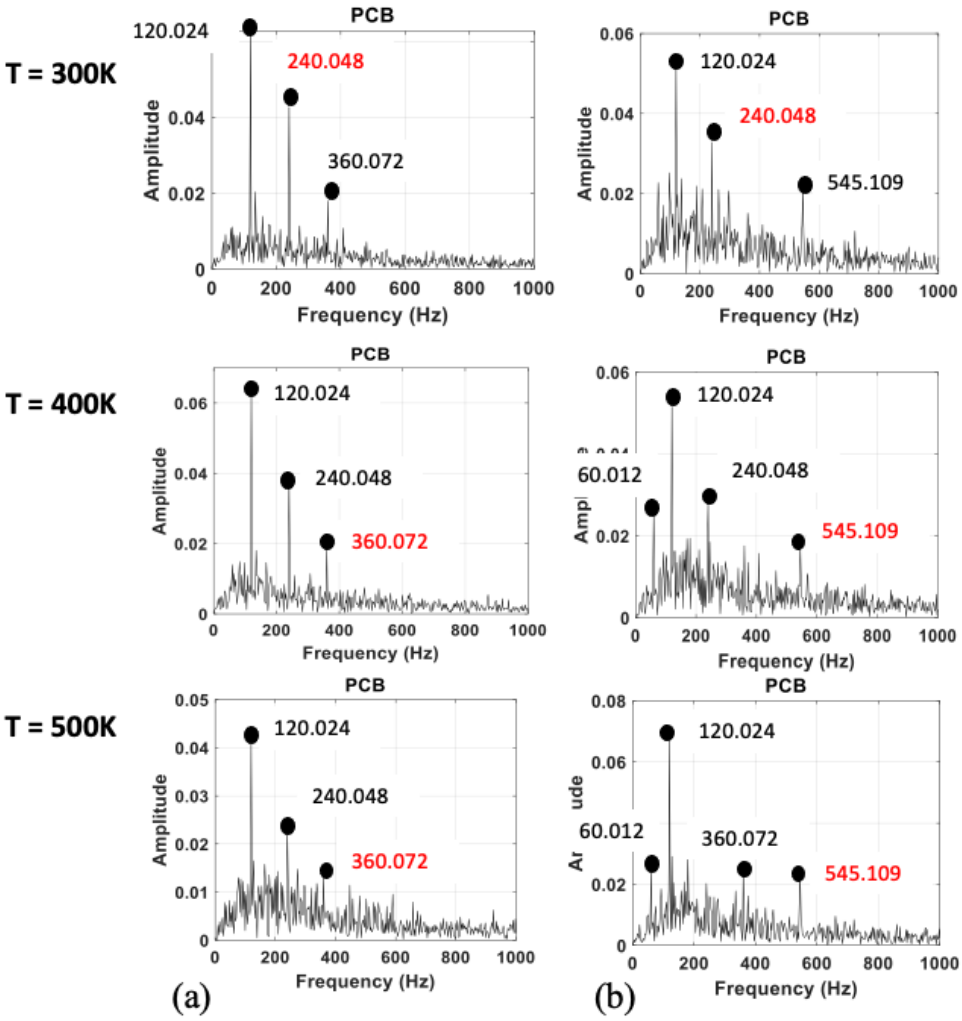

Figure 46. FFT results of the pressure (PCB) sensor located in the rectangular plenum upstream prior to the combustion chamber for (a) 6.9 case without exit plate, and (b) 6.9 case with exit plate at near stichometry. The inlet temperature increases from top to bottom of the figure.

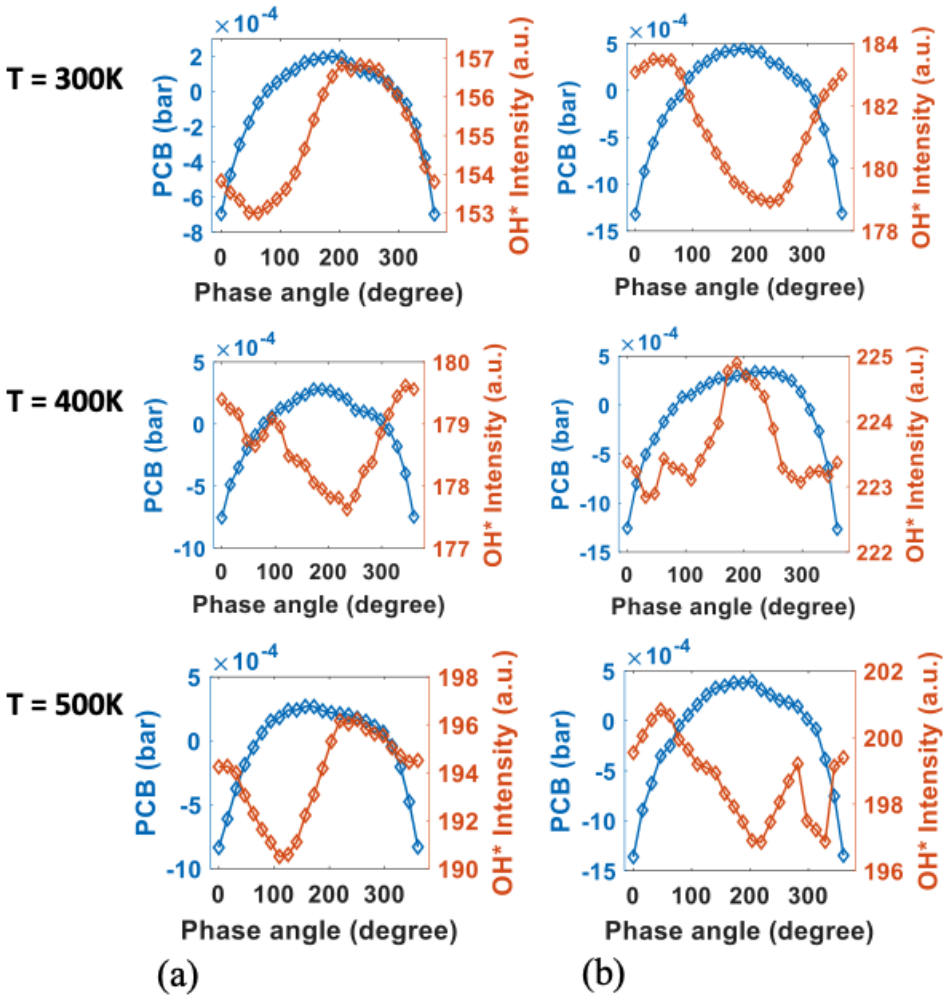

Figure 47. Phase-averaged results between the pressure in the upstream section and OH* for (a) 6.9 case without exit plate, and (b) 6.9 case with exit plate at near stichometry. The inlet temperature increases from top to bottom of the figure.

References

[1] A. Lefebvre, D. Ballal, Gas turbine combustion: alternative fuels and emissions, 2010.

[2] T. Lieuwen, V. McDonell, E. Petersen, D. Santavicca, Fuel flexibility influences on premixed combustor blowout, flashback, autoignition, and stability, J Eng Gas Turbine Power 130 (2008). https://doi.org/10.1115/1.2771243.

[3] S. Samuelsen, 3.2.1.3 Rich Burn, Quick-Mix, Lean Burn (RQL) Combustor 3.2.1.3-1 Introduction.

[4] A. Prociw, J. Ryon, J. Goeke, Low NOx combustion concepts in support of the NASA environmentally responsible aircraft program, Proceedings of the ASME Turbo Expo 2012, V04BT04A009.

[5] Y.R. Hicks, C.M. Heath, R.C. Anderson, K.M. Tacina, Investigations of a combustor using a 9-point swirl-venturi fuel injector: recent experimental results, report No. 2012-217245, NASA Glenn Research Center, Cleveland, OH, USA, 2012.

[6] S. Izadi, O. Kislat, J. Zanger, H. Seliger-Ost, P. Kutne, M. Aigner, Investigating the Impact of Steam Enhancement on Combustion in a Swirl-Assisted Jet-Stabilized Gas Turbine Combustor, J Eng Gas Turbine Power 147 (2025). https://doi.org/10.1115/1.4066235.

[7] Y. Liu, X. Sun, V. Sethi, D. Nalianda, Y.G. Li, L. Wang, Review of modern low emissions combustion technologies for aero gas turbine engines, Progress in Aerospace Sciences 94 (2017) 12–45. https://doi.org/10.1016/j.paerosci.2017.08.001.

[8] C. Shao, D. Brouzet, N. Rock, M. Ihme, Parametric analysis of core-noise from a realistic gas-turbine combustor for cruise and take-off conditions, Applications in Energy and Combustion Science 9 (2022). https://doi.org/10.1016/j.jaecs.2021.100045.

[9] R. Villalva, B.J. Dolan, D. Munday, G.A. Zink, S.D. Pack, J.L. Goeke, E.J. Gutmark, Experimental study of a multinozzle combustor at elevated pressures, AIAA Journal 53 (2015) 986–1001. https://doi.org/10.2514/1.J053123.

[10] T. Tanneberger, S. Schimek, C.O. Paschereit, P. Stathopoulos, Combustion efficiency measurements and burner characterization in a hydrogen-oxyfuel combustor, Int J Hydrogen Energy 44 (2019) 29752–29764. https://doi.org/10.1016/j.ijhydene.2019.05.055.

[11] N. Syred, A review of oscillation mechanisms and the role of the precessing vortex core (PVC) in swirl combustion systems, Prog Energy Combust Sci 32 (2006) 93–161. https://doi.org/10.1016/j.pecs.2005.10.002.

[12] C.O.U. Umeh, Z. Rusak, E. Gutmark, Vortex breakdown in a swirl-stabilized combustor, J Propuls Power 28 (2012) 1037–1051. https://doi.org/10.2514/1.B34377.

[13] A.E.E. Khalil, J.M. Brooks, A.K. Gupta, Impact of confinement on flowfield of swirl flow burners, Fuel 184 (2016) 1–9. https://doi.org/10.1016/j.fuel.2016.06.098.

[14] I. Boxx, M. Stöhr, C. Carter, W. Meier, Temporally resolved planar measurements of transient phenomena in a partially pre-mixed swirl flame in a gas turbine model combustor, Combust Flame 157 (2010) 1510–1525. https://doi.org/10.1016/j.combustflame.2009.12.015.

[15] M. Stöhr, I. Boxx, C.D. Carter, W. Meier, Experimental study of vortex-flame interaction in a gas turbine model combustor, Combust Flame (2012). https://doi.org/10.1016/j.combustflame.2012.03.020.

[16] S. Hansford, J. O'connor, K. Manoharan, S. Hemchandra, Impact of flow non-axisymmetry on swirling flow dynamics and receptivity to acoustics, in: Proceedings of the ASME Turbo Expo, 2015. https://doi.org/10.1115/GT201543377.

[17] B. Mathews, S. Hansford, J. O'Connor, Impact of swirling flow structure on shear layer vorticity fluctuation mechanisms, in: Proceedings of the ASME Turbo Expo, 2016. https://doi.org/10.1115/GT2016-56460.
[18] M. Frederick, J. Dudash, J. O'Connor, K. Manoharan, S. Hemchandra, B. Brubaker, Impact of pvc dynamics on shear layer response in a swirling jet, in: Proceedings of the ASME Turbo Expo, 2017. https://doi.org/10.1115/GT2017-64691.
[19] M. Frederick, K. Manoharan, J. Dudash, B. Brubaker, S. Hemchandra, J. O'Connor, Impact of Precessing Vortex Core Dynamics on Shear Layer Response in a Swirling Jet, J Eng Gas Turbine Power (2018). https://doi.org/10.1115/1.4038324.
[20] G. Vignat, D. Durox, A. Renaud, Investigation of transient PVC dynamics in a strongly swirled spray flame using high speed SnO 2 tomography, Combust Flame 225 (2021) 305–319. https://doi.org/10.1016/j.combustflame.2020.11.009.
[21] K. Oberleithner, M. Sieber, C.N. Nayeri, C.O. Paschereit, C. Petz, H.C. Hege, B.R. Noack, I. Wygnanski, Three-dimensional coherent structures in a swirling jet undergoing vortex breakdown: Stability analysis and empirical mode construction, J Fluid Mech 679 (2011) 383–414. https://doi.org/10.1017/jfm.2011.141.
[22] O. Tammisola, M.P. Juniper, Coherent structures in a swirl injector at Re = 4800 by nonlinear simulations and linear global modes, J Fluid Mech 792 (2016) 620–657. https://doi.org/10.1017/jfm.2016.86.
[23] M. Vanierschot, J.S. Müller, M. Sieber, M. Percin, B.W. van Oudheusden, K. Oberleithner, Single- and double-helix vortex breakdown as two dominant global modes in turbulent swirling jet flow, J Fluid Mech 883 (2020) 1–30. https://doi.org/10.1017/jfm.2019.872.
[24] S.J. Shanbhogue, Y.S. Sanusi, S. Taamallah, M.A. Habib, E.M.A. Mokheimer, A.F. Ghoniem, Flame macrostructures, combustion instability and extinction strain scaling in swirl-stabilized premixed CH 4 /H 2 combustion, Combust Flame 163 (2016) 494–507. https://doi.org/10.1016/j.combustflame.2015.10.026.
[25] Z. Wang, X. Li, Z. Feng, Z. Yang, The role of precessing vortex core in two combustion regimes: Numerical simulation studies, Journal of Mechanical Science and Technology (2019). https://doi.org/10.1007/s12206-018-1243-0.
[26] Y.R. Hicks, K.M. Tacina, Design guidelines for swirl-venturi fuel-air mixers for lean direct injection combustors, report No. 20210011787, NASA Glenn Research Center, Cleveland, OH, USA, 2021.
[27] B. Dolan, R.V. Gomez, G. Zink, S. Pack, E. Gutmark, Effect of Nozzle Spacing on Nitrogen-Oxide Emissions and Lean Operability, AIAA Journal 54 (2016) 1953–1961. https://doi.org/10.2514/1.J054685.
[28] B. Dolan, G. Zink, W. Des Moines, Gt2014-26164 Flame Dynamics in a Multi-Nozzle Staged Combustor During High Power Operation, Proceedings of the ASME Turbo Expo, 2014.
[29] B. Dolan, R. Villalva, D. Munday, G. Zink, S. Pack, E. Gutmark, Flame dynamics in a multi-nozzle staged combustor during high power operation, in: Proceedings of the ASME Turbo Expo, 2014. https://doi.org/10.1115/GT2014-26164.
[30] B.J. Dolan, R.V. Gomez, H. Nawroth, S. Pack, E.J. Gutmark, Study on the isothermal flowfields of interacting swirl-stabilized nozzles, in: 53rd AIAA Aerospace Sciences Meeting, American Institute of Aeronautics and Astronautics Inc, AIAA, 2015. https://doi.org/10.2514/6.2015-0929.
[31] Y. Shen, M. Ghulam, K. Zhang, E. Gutmark, C. Duwig, Vortex breakdown of the swirling flow in a Lean Direct Injection burner, Physics of Fluids 32 (2020). https://doi.org/10.1063/5.0028838.

[32] M.M. Ghulam, Y. Shen, F. Baier, R.G. Villalva, A. Karnam, R. Holpp, O.R. Lopez, C. Duwig, E. Gutmark, Characterization of non-reacting swirling flow in a gas fuel injector, in: AIAA Scitech 2021 Forum, American Institute of Aeronautics and Astronautics Inc, AIAA, 2021: pp. 1–22. https://doi.org/10.2514/6.2021-1109.
[33] M.A. Nemitallah, A. Abdelhafez, M.A. Habib, Experimental and Numerical Investigations of Structure and Stability of Premixed Swirl-Stabilized CH4/O2/CO2 Flames in a Model Gas Turbine Combustor, Energy and Fuels 33 (2019) 2526–2537. https://doi.org/10.1021/acs.energyfuels.8b04438.
[34] X. Chen, W. Culler, S. Peluso, D. Santavicca, J. O'Connor, Comparison of Equivalence Ratio Transients on Combustion Instability in Single-Nozzle and Multi-Nozzle Combustors, in: Volume 4A: Combustion, Fuels, and Emissions, American Society of Mechanical Engineers, 2018. https://doi.org/10.1115/GT2018-75427.
[35] L. Huang, C. Liu, T. Deng, H. Jiang, P. Wu, Experimental investigation on the influence of central airflow on swirl combustion stability and flame shape, J Therm Anal Calorim 144 (2021) 503–514. https://doi.org/10.1007/s10973-020-10399-2.
[36] G. Kewlani, S. Shanbhogue, A. Ghoniem, Investigations into the Impact of the Equivalence Ratio on Turbulent Premixed Combustion Using Particle Image Velocimetry and Large Eddy Simulation Techniques: "v" and "m" Flame Configurations in a Swirl Combustor, Energy and Fuels 30 (2016) 3451–3462. https://doi.org/10.1021/acs.energyfuels.5b02921.
[37] J. Hao, Y. Ding, C. Yang, X. Wang, X. Zhang, Y. Liu, F. Jin, Study on Unstable Combustion Characteristics of Model Combustor with Different Swirler Schemes, Energies (Basel) 15 (2022). https://doi.org/10.3390/en15238972.
[38] J. Runyon, R. Marsh, Y. Sevcenco, D. Pugh, Development and Commissioning of a Chemiluminescence Imaging System for an Optically-Accessible High-Pressure Generic Swirl Burner, 7th European Combustion Meeting (2015), (P3-29) pp. 1-6.
[39] J.A.H. Dreyer, R.I. Slavchov, E.J. Rees, J. Akroyd, M. Salamanca, S. Mosbach, M. Kraft, Improved methodology for performing the inverse Abel transform of flame images for color ratio pyrometry. Appl. Opt. 58, 2662-2670 (2019).
[40] L. Huang, C. Liu, T. Deng, H. Jiang, P. Wu, Experimental investigation on the influence of central airflow on swirl combustion stability and flame shape, J Therm Anal Calorim 144 (2021) 503–514. https://doi.org/10.1007/s10973-020-10399-2.
[41] A.M. Cormack, Representation of a Function by Its Line Integrals, with Some Radiological Applications, J Appl Phys 34 (1963) 2722–2727. https://doi.org/10.1063/1.1729798.
[42] M.F. Kasim, J. Holloway, L. Ceurvorst, M.C. Levy, N. Ratan, J. Sadler, R. Bingham, P.N. Burrows, R. Trines, M. Wing, P. Norreys, Quantitative single shot and spatially resolved plasma wakefield diagnostics, Physical Review Special Topics - Accelerators and Beams 18 (2015) 081302. https://doi.org/10.1103/PhysRevSTAB.18.081302.
[43] C.J. Dasch, One-dimensional tomography: a comparison of Abel, onion-peeling, and filtered backprojection methods, 1992.
[44] X. Feng, H. Liang, J. Suo, L. Zheng, OH* Chemiluminescence Characteristics of the RP-3 Fueled Dual-Swirl Direct-Mixing Combustor, ACS Omega 8 (2023) 30716–30726. https://doi.org/10.1021/acsomega.3c04688.
[45] O.T. Schmidt, Spectral proper orthogonal decomposition using multitaper estimates, Theor Comput Fluid Dyn 36 (2022) 741–754. https://doi.org/10.1007/s00162-022-00626-x.
[46] A. Nekkanti, O.T. Schmidt, Frequency-time analysis, low-rank reconstruction and denoising of turbulent flows using SPOD, J Fluid Mech 926 (2021). https://doi.org/10.1017/jfm.2021.681.

[47] G.A. Brès, P. Jordan, V. Jaunet, M. Le Rallic, A.V.G. Cavalieri, A. Towne, S.K. Lele, T. Colonius, O.T. Schmidt, Importance of the nozzle-exit boundary-layer state in subsonic turbulent jets, J Fluid Mech 851 (2018) 83–124. https://doi.org/10.1017/jfm.2018.476.
[48] O.T. Schmidt, A. Towne, G. Rigas, T. Colonius, G.A. Brès, Spectral analysis of jet turbulence, J Fluid Mech 855 (2018) 953–982. https://doi.org/10.1017/jfm.2018.675.
[49] G.A. Brès, P. Jordan, V. Jaunet, M. Le Rallic, A.V.G. Cavalieri, A. Towne, S.K. Lele, T. Colonius, O.T. Schmidt, Importance of the nozzle-exit boundary-layer state in subsonic turbulent jets, J Fluid Mech 851 (2018) 83–124. https://doi.org/10.1017/jfm.2018.476.
[50] A. Towne, O.T. Schmidt, T. Colonius, Spectral proper orthogonal decomposition and its relationship to dynamic mode decomposition and resolvent analysis, J Fluid Mech 847 (2018) 821–867. https://doi.org/10.1017/jfm.2018.283.
[51] P. Palies, D. Durox, T. Schuller, S. Candel, The combined dynamics of swirler and turbulent premixed swirling flames, Combust Flame 157 (2010) 1698–1717. https://doi.org/10.1016/j.combustflame.2010.02.011.
[52] M.M. Ghulam, S.S. Muralidharan, V. Anand, E. Prisell, E.J. Gutmark, Operational mechanism of valved-pulsejet engines, Aerosp Sci Technol 148 (2024). https://doi.org/10.1016/j.ast.2024.109060.
[53] A. Amer, H. Gad, I. Abdelrahman, S.I. Abdel-Mageed, Experimental study of LPG diffusion flame at elevated preheated air temperatures, International Journal of Mechanical and Mechatronics Engineering, 9 (8), 2015.
[54] K. Souflas, P. Koutmos, Effects of Stratification and Preheat on Turbulent Flame Characteristics and Stabilization, Flow Turbul Combust 108 (2022) 237–262. https://doi.org/10.1007/s10494-021-00267-w.
[55] R. Sharma, F. Cozzi, P. Di Milano, Experimental Study of Unconfined and Confined Isothermal Swirling Jets, International Journal of Mechanical and Mechatronics Engineering, 11 (2), 2017. https://doi.org/10.1999/1307-6892/10006459.
[56] D. Mason, S. Clees, M. Frederick, J. O'connor, The effects of exit boundary condition on precessing vortex core dynamics, Proceedings of the ASME Turbo Expo 2019, V04BT04A009.
[57] A. Blondé, B. Schuermans, N. Noiray, Experiments and Modelling on the Effect of an Adjustable Boundary on Thermoacoustic Stability, (2022).